Treatment Planning Methods for Clinical Electroporation

Radwan Qasrawi

TESI DOCTORAL UPF / 2017

Universitat Pompeu Fabra
Barcelona

Directors:

Dr. Antoni Ivorra

Dr.Ziad Abdeen

(Faculty of Medicine-Al-Quds University, Palestine)

Department Of Information And Communication Technologies

Universitat Pompeu Fabra

This work was carried out in the Department of Information and Communication Technologies (DTIC) at Universitat Pompeu Fabra (UPF), Barcelona, Spain.

Abstract

Two treatment modalities based on the electroporation phenomenon, electro-chemotherapy and irreversible electroporation, have been developed in the last decades to destroy solid tumors. These treatments are based on the delivery of short high voltage pulses across electrodes and their success depends on covering the whole tumor with an adequate electric field magnitude. This leads to a need for software tools capable of allowing patient-specific treatment planning. In particular, there is a need for treatment planning tools similar to those used in radiotherapy in order to plan the location of the electrodes and the voltage magnitudes to be applied across these electrodes.

Here it is described a treatment planning platform prototype which allows users to perform the complete treatment planning sequence in a single environment. The planned treatment volume is represented on the patient medical images after computing, by the finite element method, the electric field magnitude generated by needle-shaped electrodes.

Here it is also reported a study in which the above prototype was employed for analyzing the potential impact of liver blood vessels on tumor ablation by irreversible electroporation. From this study it is concluded that those vessels must not be neglected in treatment planning and that undertreatment around those vessels may be occurring frequently in current irreversible electroporation treatments of liver tumors.

Finally, it is described the implementation and characterization of a fast semi-analytical algorithm for computing the electric field distribution generated by needle-shaped electrodes. This algorithm is intended to rapidly pre-visualize the expected treatment region before proceeding with an accurate, but laborious and slow, computation based numerical methods.

Resumen

Dos modalidades de tratamiento basadas en el fenómeno de la electroporación, la electroquimioterapia y la electroporación irreversible, han sido desarrolladas en las últimas décadas para destruir tumores sólidos. Estos tratamientos se basan en la aplicación de pulsos cortos de alta tensión a través de electrodos y para su éxito se requiere abarcar todo el tumor con una magnitud de campo eléctrico adecuada. Esto lleva a la necesidad de herramientas software que permitan la planificación de tratamiento específica del paciente. En particular, existe la necesidad de herramientas de planificación de tratamiento similares a las utilizadas en radioterapia para planificar la ubicación de los electrodos y las magnitudes de voltaje a aplicar a través de estos electrodos.

Aquí se describe un prototipo de plataforma de planificación de tratamiento que permite a los usuarios realizar la secuencia completa de planificación de tratamiento en un solo entorno. El volumen planificado de tratamiento se representa sobre las imágenes médicas del paciente después de calcular, mediante el método de elementos finitos, la magnitud del campo eléctrico generada por electrodos en forma de aguja.

Aquí también se detalla un estudio en el que el prototipo anterior se empleó para analizar el impacto potencial de los vasos sanguíneos hepáticos sobre la ablación de tumores por electroporación irreversible. De este estudio se concluye que estos vasos no deben ser descuidados en la planificación del tratamiento y que alrededor de esos vasos se puede estar produciendo sub-tratamiento frecuentemente en los tratamientos de electroporación irreversible que actualmente se aplican para tumores hepáticos.

Finalmente, se describe la implementación y caracterización de un algoritmo semi-analítico rápido para calcular la distribución de campo eléctrico generada por electrodos en forma de aguja. Este algoritmo está destinado a pre-visualizar rápidamente la región de tratamiento esperada antes de proceder con un preciso, pero laborioso y lento, proceso de cálculo basado en métodos numéricos.

Contents

List of Figures

List of Tables

Acronyms and abbreviations

ac	Alternating Current
dc	Direct Current
ECT	Electrochemotherapy
IRE	Irreversible Electroporation
GTV	Gross Tumor Volume
CTV	Clinical Tumor Volume
PTV	Planed Tumor Volume
MAD	Maximum Average Diastance
VTK	Visualization Toolkit
ITK	Insight Segmentation and Registration Toolkit
MITK	Medical Imaging Interaction Toolkit
GIMIAS	Graphical Interface for Medical Image Analysis and Simulation
FEM	Finite Element Method
MRI	Magnetic resonance imaging
CT	A computerized tomography
DICOM	Digital Imaging and Communications in Medicine
TetGen	Tetrahedral Mesh Generator

CHAPTER 1

Introduction

1.1 Introduction

Electroporation, or electropermeabilization, is the phenomenon in which the permeability of the cell membrane to ions and molecules is artificially increased by applying an electrical field that causes the formation of nano-scale defect in the cell membrane. The electric field applied can be either in the form of short (dc) pulses or in the form of short (ac) bursts [1]–[4].

Electroporation is a dynamic phenomenon that depends on the local transmembrane voltage, that is, the voltage difference between the exterior and the interior of the cell[1]. It is generally stated that electroporation occurs when the transmembrane voltage reaches a certain threshold. When an electric field is externally applied to a biological organism, typically by means of electrodes, an artificially induced transmembrane voltage is superimposed to the natural resting transmembrane so that the threshold for electroporation can be reached.

Depending on the number of pulses, their magnitude, their duration and other factors, permeabilization induced by electroporation can be temporary and not compromise the viability of the cell ("reversible electroporation") or can be permanent (too intense) so that cell homeostasis is severely disrupted and the cell ends dying by necrotic or apoptotic processes ("irreversible electroporation") (See Figure 1.1)[3], [5], [6].

As it will be later described, the artificially induced transmembrane voltage is proportional to the local electric field magnitude that is created in tissue because of the passage of current delivered by electrodes. Therefore, as indicated in figure 1.1, cells in a tissue region will experience electroporation if the electric field magnitude in that region is above a threshold. This concept has been tested in a number of experimental studies and it has been recognized that, for each tissue and pulse protocol, at least two electric field thresholds can be described: a threshold for reversible electroporation and a higher threshold for irreversible electroporation[2], [3], [5], [7].

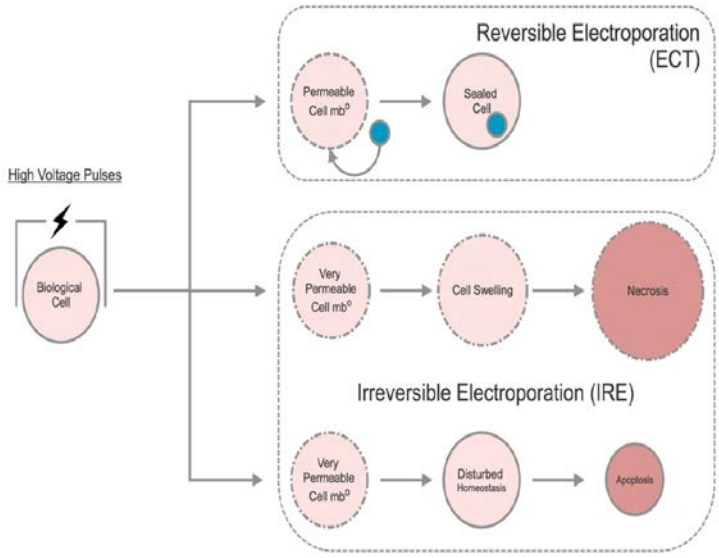

Figure 1.1. A schematic representation of the outcomes of electroporation from the perspective of a single cell (adapted from [8] with permission by A. Ivorra)

Reversible electroporation is the basis of "electrochemotherapy" or ECT for short, that is used for facilitating the penetration of anticancer drugs, mainly bleomycin and cisplatin, into malignant cells in the tissue [9].
Irreversible Electroporation (IRE) is a novel non-thermal tissue ablation method and is currently employed for destroying solid tumors[10]. According to Ivorra et al. irreversible electroporation (IRE) can be defined as "the permanent or temporal membrane electroporation process that causes cells to die"[11].
IRE can be performed by applying short pulses (microsecond to millisecond) of electrical energy applied to a direct tissue by electrodes. Typically, IRE in soft living tissues is achieved by applying 10 to 100 pulses with a duration in the order of 100 u(micro)s and a field magnitude from 500 to 3000 V/cm [4], [10].

1.1 Electroporation as a bioelectrical phenomenon

1.1.1 At cellular level

There are numerous evidences from experiments on cell suspensions[12], [13][14], isolated cells and on artificial membranes[15], [16], indicating that the electroporation occurs when the transmembrane voltage reaches a specific threshold. The value of such threshold depends on the characteristics of the applied pulses (number, duration, and shape) and also on how electroporation is assessed (e.g. by noticing an increase of membrane conductance, by detecting intracellular contents release or by observing cell lysis). Most authors reported threshold values in the range from 200 mV to 1 V.

In electrical terms, the extracellular and intracellular media are considered to behave as resistive media whereas the lipid bilayer cell membrane is modeled as a thin dielectric layer. When an electric field is applied to a biological sample, either a cell suspension or a tissue, the membrane is charged until it reaches a steady transmembrane voltage, typically in a time range in the order of 1μs. If the magnitude of the field is large enough, the induced transmembrane potentials will cause electroporation. Up to a point, the electroporation phenomenon can be understood as the dielectric rupture of the cell membrane.

Before electroporation occurs the induced transmembrane voltages are proportional to the magnitude of the applied field. In the case that a uniform field is applied to a single cell in suspension, or to a diluted suspension, it is possible to employ a simple model in order to predict when electroporation will occur: for a spherical cell of radius r with negligible membrane conductivity (figure 1.2.) the induced transmembrane potential (ΔVm) at each membrane point is[17]:

$$\Delta V_m = \frac{3}{2}\left|\mathbf{E_{ext}}\right| r\cos(\theta) \qquad (1)$$

Where θ is the angle between the radius (from cell center to evaluation point) and the applied external field (E_{ext}). This expression is sometimes referred to as the Schwan's equation.

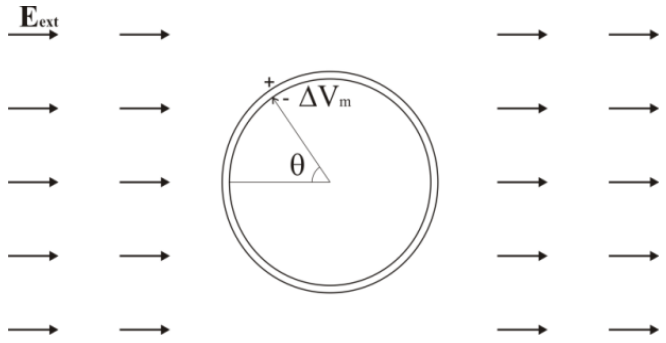

Figure 1.2. An external electric ($\mathbf{E}_{ext}$) field induces a modification of the transmembrane potential. The electric field is intentionally not drawn in the vicinity of the cell because there it is not uniform (authored by A. Ivorra; with permission).

Therefore, since ΔVm is proportional to the cell radius, lower fields are typically required to achieve electroporation in larger cells that in smaller cells (although some exceptions have been identified[18]). This fact has significant consequences when cell suspensions are electroporated in a cuvette. For instance, the magnitude of the applied electric field needs to be optimized for each cell type and better results will be obtained for cell lines with small variations in cell sizes.

Another interesting consequence of the above equation is that electroporation will not occur uniformly across the cell membrane; some areas will be easily electroporated (i.e. large $|\Delta V_m|$) whereas other will remain intact ($|\Delta V_m| \sim 0$ V). In particular, cell areas facing the electrodes, that is, perpendicular to the field direction ($\theta \sim 0$) will experience larger transmembrane voltages and therefore will become more easily electroporated. This phenomenon is nicely illustrated in[16]. In that paper, the researchers employed voltage-sensitive fluorescence dyes combined with fast microscopy and they were able to observe that:

Large $|\Delta V_m|$ occurred at the cell poles facing the electrodes.

At those areas, it was observed a huge increase in membrane conductivity (i.e. electroporation).

1.1.2 At tissue level

For more complex geometries than that shown in Figure 1.2., the equations that describe the induced transmembrane potential are much more intricate or do not exist. For those cases, it is convenient to make use of numerical methods implemented on computers. For instance, in[19] the finite element method was employed to conclude that the maximum transmembrane potential induced in erythrocytes (biconcave shape) must be 22 % lower than the maximum transmembrane potential that is reached in a spherical cell of the same size.

In dense cell suspensions and tissues, where the spaces between cells are narrow, the electric field will be far from uniform at the microscopic level. Hence the above equation for the induced transmembrane voltage in the case of an isolated cell will be useless for tissues. However, given that the resistivity of some tissues can be assumed to be homogeneous at the macroscopic level, it is possible to consider a macroscopic electric field distribution. Then it is reasonable to hypothesize that cells in a specific tissue region will be electroporated if the macroscopic electric field magnitude at that region reaches or surpasses a specific field magnitude threshold. Such threshold will not only be dependent on electroporation parameters but also on tissue type, similarly to what happens with suspensions of cells from different lines. Besides cell sizes, shapes and orientations, the intercellular distances will also play a significant role. That is, the separation between cells will modulate the transmembrane potential induced by the external macroscopic field.

The above hypothesis is now commonly employed to predict the extension and shape of tissue volume that will be electroporated with a specific electrode setup. That is, it is key ingredient of treatment planning for electroporation-based therapies. Figure 1.3. illustrates this hypothesis. Regardless of the mentioned difficulties, the numerical modeling of tissues by means of finite element methods (FEM) has been used in predicting the electroporation outcomes. The finite element requires building model geometry that includes the tissues and electrodes geometries. In which the tissues conductivities are models as homogeneous models (in Figure 1.3 a single tissue type and two needle electrodes are modeled). Then, the electric field distribution can be calculated by analytical or numerical methods. In order to identify the volume of the electroporated tissues, the electric field threshold should be known in advance. The tissues that exposed to an electric field magnitude above the $E_{threshold}$ are electroporated, while no electroporation occurs in tissues exposed to lower electric field magnitude are not electroporated. This methodology has been validated in multiple experimental studies[20]–[23].

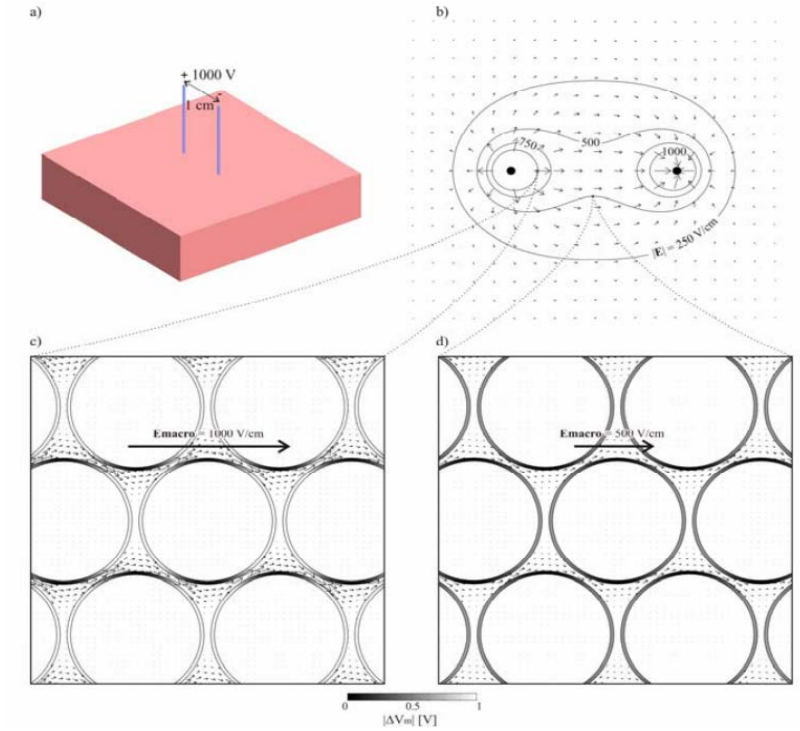

Figure 1.3. The numerical modeling of electric field distribution in homogeneous tissues. a) The geometrical model composed of two needle electrodes of 0.5 mm in diameter, 1 cm interelectrode spacing and 1000 V applied potential. b) The electric field distribution (arrows) on the tissue surface; four isolines of the electric field magnitude are also displayed (250, 500, 750 and 1000 V/cm). c) The area where the 1000V/cm electric field and the induced transmembrane potentials (ΔVm) (packed round cells with a diameter of 20 μm) are located. d) The same as subfigure (c) but at an area where the field magnitude is 500 V/cm. Note: the length scale of the microscopic field distribution in subfigures (c) and (d) is not the same than the one used for the macroscopic field (authored by A. Ivorra; with permission).

At least three different electric field thresholds can be defined that are of interest in electroporation. The lowest of them would be the threshold for the manifestation of reversible electroporation (E_{rev}); only the cells within areas where $E > E_{rev}$ are electroporated. If a second threshold (E_{irrev}) is reached or surpassed, electroporation will compromise the viability of the cells. A larger threshold can also be defined ($E_{thermal}$) for the manifestation of thermal damage caused by the Joule effect. This is particularly relevant in the case of IRE ablation techniques: if irreversibility threshold is surpassed but the thermal threshold is not reached then cells are destroyed but tissue scaffold is spared and that facilitates post-treatment healing[10].
The above modeling strategy employed for computing the electric field distribution assumed that the conductivity of the tissues was inalterable. However, recently, a refinement was introduced that further increases the accuracy of the predictions: the electrical conductivity of a tissue is not constant but depends on the electric field magnitude it is experiencing[20], [21]. This models the fact that when electroporation occurs the conductivity of the tissues increases abruptly and significantly. Such conductivity increase results in a field redistribution which in turn results in new conductivity redistribution and so on. Hence, when a high-voltage pulse is applied to a tissue, if electroporation occurs, the final electric field distribution will not be reached immediately and such final field distribution will be different from the distribution computed assuming that the tissue conductivity is constant.

1.2 Pre-clinical and clinical studies on electroporation

Currently, electroporation-based therapies (Electrochemotherapy and Irreversible electroporation) are used clinically for tumor treatment. In this thesis, it was aimed at developing a software treatment planning tool for electroporation clinical applications. Therefore, Therefore, it was deemed convenient to briefly survey past and current research on the use of clinical electroporation. Here are outlined some conclusions from that survey. It must be noted that here it was not attempted to perform a review on the use of electroproation-based therapies. The present survey is far from being a complete and exhaustive review. Its main purpose was to collect some observations that can be helpful to understand the clinical implications of electroporation-based therapies.

1.2.1 Electrochemotherapy (ECT)

In the context of cancer treatment, reversible electroporation can be employed both for gene delivery and for chemotherapeutic drug delivery. Although electroporation-mediated gene delivery for cancer treatment shows very promising results[22], its clinical use is still quite immature. This section focuses on electrochemotherapy, which consists in the use of

reversible electroporation for introducing chemotherapeutic drugs into solid tumors cells.
Electrochemotherapy was pioneered by Lluis Mir in the early 90s with an initial clinical trial for cutaneous and subcutaneous (head and neck) tumor nodules[3]. Then, electrochemotherapy rapidly gained popularity and currently exists as an independent treatment procedure in clinical settings. ECT now is very well established in in clinical centers in Europe and reported response rates range from 72%-100%[9], [23].
In the 90s and early 2000s, in parallel to clinical trials, several studies were performed in animal tumor models either spontaneous or transplanted at different locations such as skeletal muscles, liver, and brain for optimizing electrochemotherapy protocols and for exploring different clinical targets. The animal models included mice, rats, and rabbits in which high ECT antitumor effectiveness was reported on carcinomas, melanomas, neuroblastomas, and fibrosarcomas in the muscle, liver or brain [24]–[29].

1.2.1.1 Early pre-clinical studies

- *In vitro* studies

Electroporation was shown to increase the permeability of different pharmaceutical and chemotherapeutic molecules into the tissue where an electric field is applied. In 1988, suitable candidates for ECT were identified by in vitro studies on Chinese hamster lung fibroblast cell cultures and were limited to bleomycin and cisplatin[30]. The conditions that allowed for the chemotherapeutic agent to be suitable for ECT use were their permeability, which is determined by the size and physic-chemical properties of the molecules. Both bleomycin and cisplatin act on breaking the DNA strands upon entering the cells. In vitro studies showed that bleomycin enters the cell and disrupts DNA strands in 30 seconds following the electroporation pulse, and only several hundreds of the molecule are sufficient to kill the cell[31]. It was shown that bleomycin's cytotoxicity was increased 300-700 fold when electroporation was applied in comparison to no electroporation pulses [32]. The cytotoxicity increase of cisplatin with electroporation was less than that observed with bleomycin. However, cisplatin was extremely useful to reduce the cumulative dose of bleomycin in the case of multiple treatments. Note that a cumulative dose of bleomycin higher than 300mg/m^2 could contribute to lung fibrosis[23].

In vivo studies

Electrochemotherapy has been used to treat different types of tumors in animal models, such as (cats, canines, and horses)[26], [33], [34]. Studies on brain tumor, liver and pancreas indicated promising results [35],[24],[3], These studies were also used to demonstrate the most

effective route of administration (intravenously or intratumorally), drug dosage and pulse parameters[32]. It became a standard to employ eight voltage pulses of 100 μs producing an electric field in the range from 1000 V/cm to 1500 V/cm at a repetition frequency of 1 Hz or 5 kHz. Moreover, Moreover, a minimum interval of 4-weeks between consecutive ECT treatment was affirmed for protection against side effects of cumulative bleomycin doses especially on the lungs[36].

In a comparative study conducted on 25 dogs that suffered from Canine Mast Cell Tumors (MCT), electrochemotherapy effectiveness in treating tumors was assessed. During the study, both the duration of response to treatments and the response rates were assessed. The results showed that ECT caused similar antitumor success as surgical treatment; however, treatment response of the surgical treatment was shorter than that of ECT. This suggests that ECT can be used as an alternative to surgery, especially when the small nodules are used in one treatment session can result in a complete response with a long duration. Interestingly, no major side effects to ECT were reported apart from minor temporary muscle contraction during the application of ECT and partial necrosis which resulted in a superficial scar that fell off within a few weeks after the treatments. The effectiveness of electrochemotherapy on brain tumors of male rate showed complete tumor ablation with minimal side effects[28].

1.2.1.2. Clinical studies

Electrochemotherapy clinical studies were advanced further in a successful first clinical phase I-II trial in 1993 on eight patients with nodules of head and neck squamous cell carcinomas using bleomycin. The results were promising with 57% of the nodules having a complete response within 4-5 days[37]. Recent ECT clinical trials using either bleomycin or cisplatin, indicate tumor response rates above 80%[38]–[40].

Almost all previously mentioned clinical trials were concerned with cutaneous nodules and not any subcutaneous, deep-seated tumors. Treatment of deep-seated tumors by electrochemotherapy was not attempted until recently[41]. Another clinical trial was conducted in Greece on 47 patients with cutaneous and subcutaneous tumors in which a 63.83% of the tumors showed a complete response, while 31.91% showed only partial response and only 4.26% of the tumors show no response at all[42].

Further clinical trials confirmed the safety and efficacy of using ECT in treating the tumor with different histologies. A two-year-long study lead by Marty et al. on 41 patients to evaluate the efficacy of ECT on cutaneous and subcutaneous metastases using both bleomycin and cisplatin showed that ECT was effective in treating both cutaneous and

subcutaneous tumors[9]. Moreover, ECT was tested on treating pancreatic cancer. A study was carried on 13 patients with advanced pancreatic cancer in phase I/II. Electrochemotherapy was completed along bleomycin in an open surgery. All patients underwent Ultra Sound and Magnetic Resonance Imaging before and after the application of ECT, some were also assessed by morphological computer tomography. There were no side effects or major complications recorded with the good functional result. Moreover, the surrounding viscera was not damaged and most importantly, ECT was recorded to be able to treat locally advanced pancreatic cancer [46]. Larkin et al. conducted a research on a total of 111 tumors and reported the effectiveness of using Electrochemotherapy in treating cancers that are progressive, unable to be operated on or recurrent. In addition to its competency, the results showed its safety, inexpensive and absence of pain or bleeding[44].

1.2.2 Irreversible electroporation (IRE)

During the last two decades in which reversible electroporation was clinically employed for drug and gene delivery, irreversible electroporation was mainly perceived as a detrimental outcome that occurred when excessive fields were applied. However, in 2005, Davalos and Rubinsky proposed that irreversible electroporation could be employed as a tissue ablation modality without some of the constraints and drawbacks of thermal methods and without the requirement of any chemotherapeutic drugs [5]. In 2006, it was experimentally demonstrated that IRE can selectively ablate areas of non-pathological rodent livers[45]. This later study confirmed the hypotheses by Davalos and Rubinsky and prompted the development of further animal studies aimed at further refining the IRE techniques and the study of possible clinical applications.

1.2.2.1 Early pre-clinical studies

- *In vitro* studies

An in vitro study conducted on MDA-MD-231 human mammary carcinoma cells, where a set of pulses were incorporated into a three-dimensional numerical model of the heterogeneous system to establish the threshold needed to induce IRE. The study results showed that IRE was induced at 1000 V/cm with an electrode placed within 0.5 mm of the tissue margin to get the best results. This study found that IRE is an effective method to fully treat heterogeneous tissue without causing thermal damage and resulting in side effects (scarring, aesthetic effects) [46]. Rubinsky et al. conducted systematic studies of the parameters needed for IRE of cancer cells. In this study, they used an electric field strength of 125V/cm to 2000V/cm with pulse numbers from 1- 3840.

While the pulse duration remains constant. The study found that the prostate cancer cells were completely destroyed without any thermal damage[47]. Bao et al. systematically studied the electroporation of tumor and blood cells, in which various electroporation duration and electric field intensities were applied including irreversible electroporation threshold (E 110-1200V/cm), the study observed rapid tumor cell death due to electroporation[48].

Furthermore, the advantages of IRE triggered the interest of researchers leading to many in vitro studies [46], [49]–[51]. In which the effect of IRE on the artificial membrane systems, including lipid bilayer sheet membrane and the isolation of single individual cells from their extracellular environment has been investigated[52], [53].

- *In vivo* studies

The effectiveness and safety of IRE have been investigated in several in vivo studies[54]–[57]. Guo et al. conducted a study on 30 rats with Hepatomas, the results confirmed the effectiveness of using IRE in ablation of liver tumors[57]. Furthermore, the ablation effectiveness of IRE has been investigated in [58] 69 pigs, the results showed that the increase in the IRE electric field intensity increased the treatment region. An in vivo study conducted on 87 mice with livers tumors divided the subjects into two groups and treated them with different combinations of field strengths (1000V/cm, 2000V/cm) and anti-hyperkalemic therapy. The study results showed that mice that received 1000V/cm survived longer than those given 2000V/cm. The study also showed that mice were given 2000V/cm and anti-hyperkalemic had a higher survival rate than those treated with 2000V/cm alone [59]. This suggested that ionic disturbances should be monitored and corrected when doing large ablation volume IRE.

Another study conducted on 18 pigs that treated different tissue types using IRE; muscle, kidney, and liver. It was shown that each tissue has its own electrical conductivity properties that require its own customized IRE with a specific electrical parameter to induce the best results [60].

Furthermore, the IRE parameters (Electrode parameters, pulse duration, the number of pulses and tissue electrical properties) were further tested and validated in many studies on various tissue types. They were tested in liver, brain, lung, kidney, and prostate in deferent animal models(rat, rabbit, porcine and dog)[61]–[67].

1.2.2.2 Clinical studies

IRE has already been tried for the ablation of human tumors. In 2011, Thomson KR and colleagues investigated the safety of irreversible electroporation. In their study, a set of 38 volunteers with advanced malignancy of liver, kidney or lung (with overall 69 separate tumors), who were unresponsive to other treatment procedures, were subjected to IRE treatment under general anesthesia. Clinical examinations, biochemistry, and CT scans of the treated organs were performed before, immediately after IRE, and after 1 month and 3 months. The study results indicated that no mortalities occurred in 30 days after IRE. A few complications were reported: four patients had a transient ventricular arrhythmia, one patient developed obstruction of the upper urethra after IRE, and one adrenal gland was unintentionally directly electroporated, which produced transient severe hypertension. The CT scans results after IRE showed that complete volume ablation was achieved in 46 tumors, out of 69 (66%), and that most treatment failures occurred in renal and lung tumors. The study concluded that IRE can be used as a safe ablation modality for humans under the use of synchronized electrocardiography (ECG) for pulse delivery and under general anesthesia[68].

Furthermore, in 2011, IRE was experimentally tested by [69] in a clinical study for assessing the feasibility and safety of ablating renal cell carcinoma (RCC) in human tissues by IRE. Six patients scheduled for curative resection of RCC were subjected to IRE. IRE was followed by monitoring procedure in which the central hemodynamics were recorded 5 minutes before and after electroporation, electrocardiography (ECG) before, during, and at scheduled intervals after the intervention, and blood sampling. The analysis of monitoring results did not show any changes: in the ST waveforms (STAN) and direction deviations, in the central hemodynamic 5 min after IRE, in hematological, serum biochemical, and in the ECG variables during the investigation period and in cardiac function after IRE therapy, while only one case of supraventricular extrasystole was encountered. However, the study concluded that the IRE can be used as feasible and safe technique to treat patients with kidney tumors[69].

In another study, unresectable soft tissue tumors in the liver and pancreas in a group of 150 patients were treated and analyzed with IRE over the period of 2 years. The study results showed that using IRE for larger lesions or lesions with more vascular involvement showed no significant increase in side effects or morbidity rate compared to less complex lesions. This proves that IRE is a safe alternative to conventional ablative methods for unresectable soft tissue tumors [70].

As for Renal Cell Carcinoma (RCC), a clinical trial conducted on six patients who were given IRE treatment immediately before the resection of the tumor. The study results showed no immediate side effects of IRE;

no change in the hemodynamic state during the study except for one case of supraventricular extrasystole. This study proved the effectiveness and safety of IRE over other ablative techniques [69]. In a phase-II clinical trial conducted [71], on twenty-nine patients with unresectable, centrally located colorectal liver metastases who were treated with IRE and followed up 12 months after IRE, a high variation of efficacy with a higher efficacy for tumors $\leq$ 3 cm was shown. The study also showed a local recurrence rate of 67-100%. These results were considered encouraging and showed an advantage over the only other option that these patients had which is palliative chemotherapy [71].

A clinical trial was conducted on 139 patients with locally advanced pancreatic cancer, divided into 2 groups; one group treated with IRE and standard therapy and the other group treated with standard therapy (chemotherapy and radiation) alone. The study results showed that patients who underwent IRE and standard therapy combined had a better local palliation, distant palliation and overall survival compared to those who underwent standard therapy alone. The study results showed a mortality rate of only 2% in the combined therapy [72].

A study on 28 patients with perivascular hepatic malignant tumor showed that IRE treated all tumors via both open and percutaneous approaches. Complications occurred in 2 patients and the overall morbidity was 3%. IRE had a combined local failure of only 7.5% [73]. Another study on patients with perivascular hepatic malignant tumors showed that 10 out of 14 treated patients (71%) were successfully treated with no reoccurrence seen during follow-up sessions. Complications were mainly hemorrhage and occurred in 4 out of 14 (29%) due to multiple needle insertions while the bile duct remained intact. This study proved that IRE is more effective than thermo-ablative techniques but still carries a similar risk of complications [56].

IRE was used to treat two patients with locally advanced pancreatic cancer and one with colorectal liver metastasis. The study results showed a successful IRE procedure of the whole tumor in all three patients and on the minimum 7-month follow-up there was a 100% local control without any progression. No complications were found to be directly connected to the procedure [74].

The first numerical study showed that it was possible to destroy cells by irreversible electroporation without inducing significant temperature increases. The feasibility of this treatment for different cancer types including breast cancer was investigated further by determining the threshold of the electric field required for irreversible electroporation. It was then found that a threshold of 1000V/cm was capable of achieving irreversible electroporation to cells in culture[46][75], [76]. Furthermore, a study on a 3D model consisting of cancer cells cultured in collagen 1 hydrogels treated by IRE and after that compared to that in an in vivo

system. The study results showed that both systems showed same characteristics of treating tumors. This study proved the effectiveness of using a 3D model to mimic in vivo model and therefore proved its clinical applicability and reliability [51].

1.3 Treatment planning for electroporation-based therapies

Treatment planning can be defined as the procedure in which the best conditions for treating a patient are defined. In electroporation-based therapies, treatment planning is the process in which it is planned, by means of computer systems, the electric field distribution to be induced in a patient.

Electroporation-based treatments aims to precisely cover the target volume with the required electric field distribution while minimizing the damage to the healthy surrounding tissue.

There are two main approaches for generating electroporation treatment plans: forward planning, and inverse planning. In forwarding planning, useres design the treatment plan, simulate it and observe the predicted result on a computer system.

The users can change the treatment plan parameters (i.e. electrode position, length, orientation and applied voltages) until an acceptable solution is achieved. In inverse planning, the electroporation treatment parameters are specified by the users and then the system automatically computes the best treatment parameters.

Similar to radiotherapy treatments, electroporation-based treatments are localized treatments in which the definition of a target volume is considered to be a prerequisite for an efficient 3D-treatment planning, depending on high-quality patient specific medical image (CT or MRI). Adopting the terminology from radiotherapy, three relevant volumes can be defined in electroporation treatment planning. The first is the localized and extent (the visible tumor) of the gross tumor (GTV). The second volume is the clinical target volume (CTV) which is the GTV plus a margin of tissue containing the GTV. The CTV volume should be adequately treated to achieve a cure. The third volume is the planning target volume (PTV) which manages the uncertainties in planning or treatment delivery[77].

Figure 1.4. shows a proposed radiotherapy treatment plan for liver tumor based on the International Commission on Radiation Units (ICRU) 62 recommendation[78]. The PTV, CTV and GTV volumes were identified.

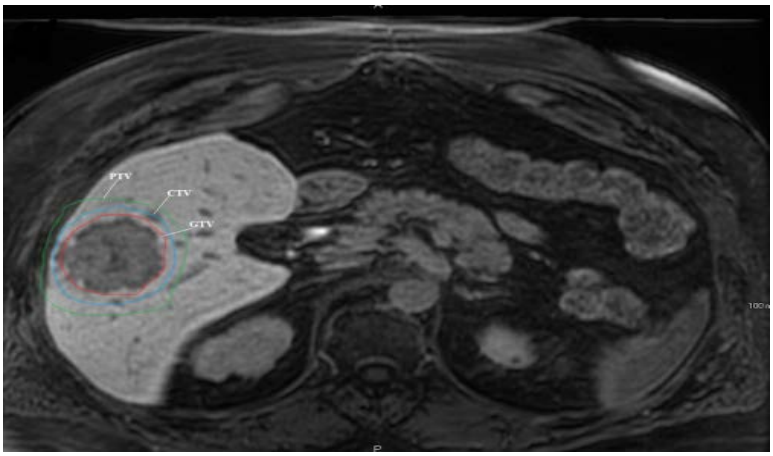

Figure 1.4. Image from a radiotherapy treatment planning procedure for a patient with a liver tumor. The gross tumor volume (GTV; red) is defined on the contrast-enhanced CT, the clinical target volume (CTV; blue) is a 2-mm expansion on the GTV, and the planning target volume (PTV; green) [79].

Furthermore, electroporation treatment planning should take into consideration the organs at risk (OR) by adding a safety margin around the PTV to ensure that the organ will not be exposed to unsafe electric field distribution.

Mathematical and numerical modeling have been used to successfully predict treatment outcomes in electroporation-based therapies in relatively simple and experimental scenarios. Several studies used the numerical modeling for calculating the in vivo electric field distribution[51], [75], [76], [80]–[83]. The finite element method and the 2D/3D models that represent the target tissue, and specified electric field threshold value for identifying the electroporated regions have been used in numerical modeling[83]–[85]. In these studies it has been validated the notion that the tissue exposed to electric field higher than the specified threshold can be considered as effectively treated by electroporation, while no electroporation occurs in the regions in which the electric field magnitude is below that threshold. In order to identify the covered volume of the electroporated region, the threshold value must be known in advance[5], [83], [86].

Although there are some examples of studies in which numerical methods have been used to optimize electrode setups for electroporation-based therapies, very few examples exist in which patient specific treatment planning has been attempted, either in animals or in humans. Two examples of electroporation treatment plan based on finite element method has been conducted for calculating the electric field distribution on mouse tumor and in muscle tissue models[87], [88]. Another study for

identifying the electroporation threshold values in liver tissue was conducted, in which the reversible and irreversible volumes at 360V/cm and 640V/cm were experimentally compared for static and sequential models [21], [89]. Furthermore, the impact of electric conductivity changes on electric field distribution during electroporation has been experimentally examined [90]–[93].

The impact of electrode configurations (insertion depth, interelectrode spacing, diameter, and contact surfaces) on electroporation treatment has been included in numerical modeling and investigated in several studies [10], [57], [89], [96], [94], [97]. Furthermore, the changes in tissues electric conductivity during electroporation were numerically and experimentally investigated [21],[97], [98].

In clinical setting, treatment planning has been used for electrochemotherapy by institutions in Europe for treating deep-seated tumors in various organs, such as liver, bone, brain, and soft-tissue[41] [99][96] [100]. Recently, IRE is being introduced to clinical trials for treating deep-seated tumors in liver, pancreas, prostate and renal tumors in many institutions in the USA and Europe[101].

Following the electroporation treatment procedures to ensure safety and efficacy treatment, a patient-specific treatment plan is required for both ECT and IRE[84], [96], [99], [102]. Specially for deep-seated tumors that are heterogeneous in shapes, size, and location in the body; therefore, obtaining total coverage on the target tissue with sufficient electric field distribution requires modeling of electric field distribution[103], [104]. To ensure an excellent treatment quality, it is important to have treatment planning tool that model the electric field distribution and able optimize the treatment.

Recently, the University of Ljubljana has developed the first treatment planning tool for electroporation therapies. It is a web-based tool for patient-specific planning in different tissues [99], [105]. The tool is composed of image processing algorithms for segmenting and reconstructing the 3D models and the numerical modeling for calculating the electric field distribution is performed by COMSOL Multiphysics (Comsol AB, Stockholm, Sweden).

1.4. Research Aims and Objectives:

The general aim of this thesis is to contribute to the development of treatment planning tools and methods for treatment modalities based on electroporation.

1.4.1 . Research objectives

The specific research objectives of the thesis are listed below, coarsely in the order they were pursued:

O1. To develop a prototype of a treatment planning platform for treatments based on electroporation which employ needle-shaped electrodes.

O2. To investigate the impact of blood vessels on IRE treatments in the liver by simulating a large set of clinically plausible treatments in an anatomically realistic model.

O3. To develop a method capable of rapidly computing the electric field distribution generated by needle-shaped electrodes in order to pre-visualize the expected treatment region before performing an accurate, but laborious and slow, computation based numerical methods.

1.5 Dissertation overview

Chapter 1 describes the electroporation phenomena and introduces the electroporation based therapies for cancer treatment. It contains short overview of pre-clinical and clinical studies that demonstrated IRE and ECT treatments in different locations such as the liver, the prostate, the pancreas, the kidneys and the skin. Diverse parameters that determine the treatment quality are indicated and are related to the need for patient-specific treatment planning prior the actual treatment is delivered. Basic concepts and terminology related to treatment planning are presented.

Chapter 2 describes the development and use of a treatment planning prototype for electroporation based therapies which employ needle-shaped electrodes. This platform is implemented on a 3D biomedical image computing open source framework, GIMIAS, and links to an external numerical solver, COMSOL Multiphysics, to compute the planned treatment volume according to the location of the electrodes specified by the user through an interactive graphical tool. The platform allows users to perform the complete treatment planning sequence in a single environment.

Chapter 3 describes a study in which it was quantitatively investigated the potential impact of liver blood vessels on tumor ablation by irreversible electroporation. A large set of clinically plausible treatments was simulated in an anatomically realistic model. From the results it is concluded that those vessels must not be neglected in treatment planning

and that undertreatment around those vessels may be occurring frequently in current irreversible electroporation treatments of liver tumors. In order to prevent this risk, it is proposed and analyzed a solution based on infusing isotonic low conductivity liquids into the liver vasculature

Chapter 4 describes the implementation and characterization of a fast semi-analytical algorithm for computing the electric field distribution generated by needle-shaped electrodes. The performance of the algorithm is compared against the performance of simulations based on the finite element method in terms of speed and accuracy. This algorithm is intended to rapidly pre-visualize the expected treatment region before proceeding with an accurate, but laborious and slow, computation based numerical methods.

CHAPTER 2

Treatment Planning Platform Prototype for Electroporation-Based Therapies

Abstract

Electroporation is the phenomenon in which the permeability of the cell membrane to ions and molecules is artificially increased by applying an electrical field that causes a formation of nano-scale defect in the cell membrane. With the recent advancement of technology, electroporation therapy (electrochemotherapy(ECT) or irreversible electroporation(IRE)) has become an increasingly attractive option for minimally invasive treatment of cancer tumors in clinical applications. To perform a successful ECT or IRE treatment, a patient specific treatment planning is required. In this study we have developed in a single and complete platform a patient- specific treatment-planning prototype based on patient medical image. The Graphical Interface for Medical Image Analysis and Simulation (GIMIAS) was integrated with the Comsol numerical simulation software. This prototype has several attributes namely: it includes algorithms for 3D model geometry reconstruction from patient medical image, allows physicians to insert and manipulate the electrodes, calculates the electric field distribution over the patient image, and helps physicians to better visualize patient's anatomic structures which allows them to easily find an adequate treatment.

2.1 Introduction

Electroporation therapy is becoming an increasingly attractive option for minimally invasive treatment of cancer diseases. During electroporation procedure, electric pulses are delivered into tumor volumes whereby the electric field distributed to the surrounding tissues which then causes cell electroporation. The success of electroporation treatment relies on three main criteria: maximum volume coverage with sufficient electric field distribution, a minimum damage of healthy tissues, and the choice of the optimal needle insertions. However, the planning of such treatment is still difficult in clinical application.

Recently published studies showed a direct relationship between electroporation parameters (i.e. electrodeposition, length, orientation, electric potential and the number of pulses) and lesion size and shape. All these parameters have to be taken into account for providing an efficient and accurate electroporation treatment[46], [47], [88], [106].

On computer simulation aspects, until now very few developments have been carried out in the field of electroporation simulation and treatment planning. Most of the published simulations were conducted on numerical modeling by means of finite element methods and do not seem to be simple to integrate the medical imaging for patient-specific treatment planning. However, it can accurately compute electric field distribution on modeled geometry[10], [84], [86], [107]–[110].

Recently, a research group in the University of Ljubljana leaded by Prof. Miklavcic has proposed the first patient-specific electrochemotherapy treatment planning software. The software makes use of patient-specific medical images to build the 3D volumes, needle insertion tool and the Comsol Matlab link for numerical simulation of the electric field distribution[110]. Later, the same group developed a web-based electroporation treatment planning software that includes a fully automatic liver segmentation algorithms, electrode insertion tool and the electric field distribution was computed by using the Matlab-Comsol finite element solver[99]. Nevertheless, the geometry identification and the computation of electric field distribution is a timely process and it seems to be limited to adequate liver electroporation treatment planning.

In this work, we propose a software prototype for electroporation treatment planning that incorporates image-processing software, the building of the 3D geometries from patient-specific medical images, electrodes insertion, and the calculation of electric field distribution in a desktop single platform. Here, we describe the implementation of the electroporation treatment planning platform including the software development environment, the building of the 3D geometries from patient-specific medical images, electrodes insertion, and the calculation of electric field distribution. The goal of our proposed software prototype

is to provide physicians with an easy and user-friendly platform for patient-specific electroporation treatment planning.

2.2 Software development environment

The electroporation treatment-planning prototype is a medical image-based and cross-platform operating system software developed in C++ programming language to calculate the electric field distribution. The prototype was developed based on *Graphical Interface for Medical Image Analysis and Simulation* (GIMIAS) open source package that has been initially developed by the Center for Computational Image and Simulation Technologies in Biomedicine (CISTIB) at the University of Sheffield (UK) and the Pompeu Fabra University (Spain) [93].

The development package (GIMIAS) is a framework that integrates different tools for medical imaging, computational modeling, computer graphics, and numerical modeling for building clinical applications. GIMIAS provides a graphical user interface with all main data input/output, rendering, data access, and advanced visualization of multi-modal imaging data. In addition, it is built over a widely used open source C++ libraries which are the Visualization Toolkit (**VTK**, supported by Kitware Inc.), the Insight Toolkit (**ITK**, also supported by Kitware Inc.), the DICOM Toolkit (**DCMTK**, supported by Offis in Germany), the Medical Imaging Interaction Toolkit (**MITK**, developed at Division of Medical Informatics, Deutsches Krebsforschungszentrum (DKFZ), Germany), and other commonly used C++ libraries (**Boost**, **wxWidgets**, CXXTest, among others)[111]–[113][114].

The software designed to be extended via the addition of plug-ins, which are software entities that can be created using the C++ language and integrated into GIMIAS general architecture.

The framework provides set of classes for creating new plug-in[114]:

- **DataEntity**: This class stores and encapsulates a single data object (e.g., medical image, transformation, surface mesh, model simulation result, etc.).
- **DataHolder**: This class allows objects to register as observers of data, for instance, to be notified when the data is changed.
- **WorkingData**: This class holds a reference to the DataHolders associated to the data required and is currently used by the plug-in (selected input, output, etc.).
- **DataEntityList**: This class contains a list populated with the data entities currently available for processing in the application. The input data that will be processed by the plug-in and also their outputs are stored in this list.

- **FrontEndPlugin**: This is the base class for all the plug-ins, every new plug-in must extend from this class. This base class provides access to the rendering classes but delegates the creation of the rendering scene to the extending class' implementation.
- **Processor**: This class executes one algorithm that produces one or more input data and generates one or more output data (usually coming from the DataEntityList).

Furthermore, the framework integrates the VTK, which provides basic services for scientific visualization, mesh processing data, post-processing and heterogeneous data management (images, poly data, surface geometries, volumetric meshes). In addition, it integrates the MITK, ITK, and DICOM Toolkits to provide multi-modal image processing (MRI, SPECT, MSCT, US, PET) in standard input /output format. The advantages of using these toolkits are the computational framework and the underlying designed algorithms which are implemented and optimized as platforms independent. In addition, the inclusion of data flow model in their computational framework has two subclasses; the volume subclass which is responsible for reading images in DICOM format (CT or MRI) and normal image data, and the mesh subclass which constructs 3D meshes from geometrical data structure [115].

Figure 2.1. Illustrates the flow diagram of treatment planning prototype. In the image processing stage, the tool contains sets of algorithms for Image loading and visualization, segmentation, and volume construction. The MITK rendering algorithms provide users with the ability of reading and displaying medical images in different formats (DICOM, Meta Image, and VTK images) with the possibility of image editing (cropping, orientation, and merging). Besides that, the noise in the acquired image data could be eliminated by denoising filters, such as Gaussian blur filter and Median Image Filter. Furthermore, different ITK segmentation algorithms are included such as region growing, threshold segmentation and Otsu segmentation, in addition to the interactive segmentation tool in which users can edit the segmented region of interest with mesh editor plugin (MrachingCubes and TetGen or Netgen)[116] that allows 3D surface and volume construction.

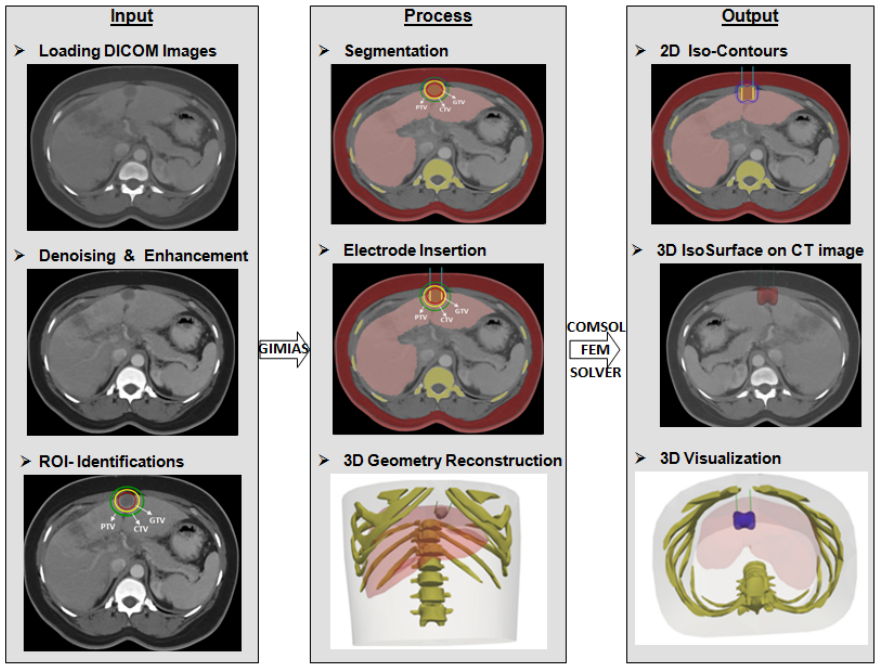

Figure 2.1. Process flow diagram illustrates the clinical workflow of electroporation treatment planning.

The treatment planning output is illustrated in Figure 2.1 which shows three types of electric field distribution visualization: The 2D iso-contours, The 3D iso-surface over the CT medical image, and the 3D Iso-surface within the 3D model.

2.3 Building model 3D geometry

2.3.1 Building the 3D volume from a medical image

The first essential step in modeling the electric field distribution is to define the 3D volumes (i.e. regions or domains) within the human body in which the electric field will be computed. Within the Region of Interest (ROI), volumes will be defined according to the tissue types which exhibit different electrical properties that impact the electric field distribution (e.g. electric conductivity, σ S/m).

To build 3D representative models for electroporation treatment planning, patient medical image (MRI or CT) is imported into software DICOM plug-in. The input data image is loaded into GIMIAS DICOM viewer. Then, the DICOM plug-in creates a volumetric image from the selected DICOM data. After that, the image is rendered and located in the

DataEntityList where it becomes accessible for the rest of plug-ins for further processing.

The 3D geometry is constructed from the patient image by segmentation of CT or MRI image data set. Therefore and similar to radiotherapy treatment planning, a set of volumes (GTV, CTV, and PTV) – which corresponds to different tissues – will be constructed in order to perform the computation of the electric field by treatment planning tool. Segmentation of the target tissues and the organs will be performed using different segmentation algorithms, such as threshold segmentation, binary segmentation, vtk Connected threshold, and region grow segmentation algorithms, in addition to the semi-automatic interactive segmentation tool that provides the user with image editing tools.

Figure 2.2. shows 3D geometry construction of the 2.8cm^3 liver tumor from a patient specific CT image[79]. The segmentation of the region of interest was conducted using region growing segmentation algorithm that depends on the intensity level, therefore, segments are defined as clusters of pixels with the same intensity levels. The region growing algorithm starts with a seeding point extracted by a mouse click on the target region of interest. The algorithm checks the eight neighboring pixels around the seeding point and selects all pixels with the same intensity level. Then, the algorithm continues checking the neighboring pixels and stops when there are no more neighbor pixels with the same intensity. Furthermore, the interactive segmentation tools allow the user to add, delete or modify the segmented cluster according to their need.

The process of converting the segmented volumes into a 3D geometry was carried out by VtkMarchingcubes algorithm and the surface editor plug-in. The algorithm constructs a 3D surface mesh from the segmented image data. The surface mesh is converted to the volumetric mesh using tetrahedral mesh plug-in. Therefore, the volumetric quality and regularly shaped elements are ensured by controlling the maximum distance between neighboring nodes and the radius to edge ratio.

For electroporation numerical simulation, it is necessary to simplify the volumetric mesh and to generate a proper solid model for finite element solver. The mesh was simplified using the vtkQuadraticdecimation algorithm. In order to protect the mesh boundaries during simplification, the process is controlled by the preserve mesh boundary and preserve topology parameters. In addition, the vertex classification characterizes the local geometry and topology according to their local neighborhoods, the decimation criterion that estimates the error of each vertex if removed, and the triangulation process that triangulates the whole polygon after removing vertices.

In our prototype, the Comsol Multiphysics software is used for numerical modeling of electroporation treatment planning. Unfortunately, Comsol is often unable to model the surface mesh which leads to difficulties in

calculating the electric field distribution. Since Comsol-FEM solver works more efficiently on solid volumes, we integrated the "Create Shape from Mesh" and Convert to Solid" algorithms from the FreeCAD library to convert the volumetric mesh into solid volumes.

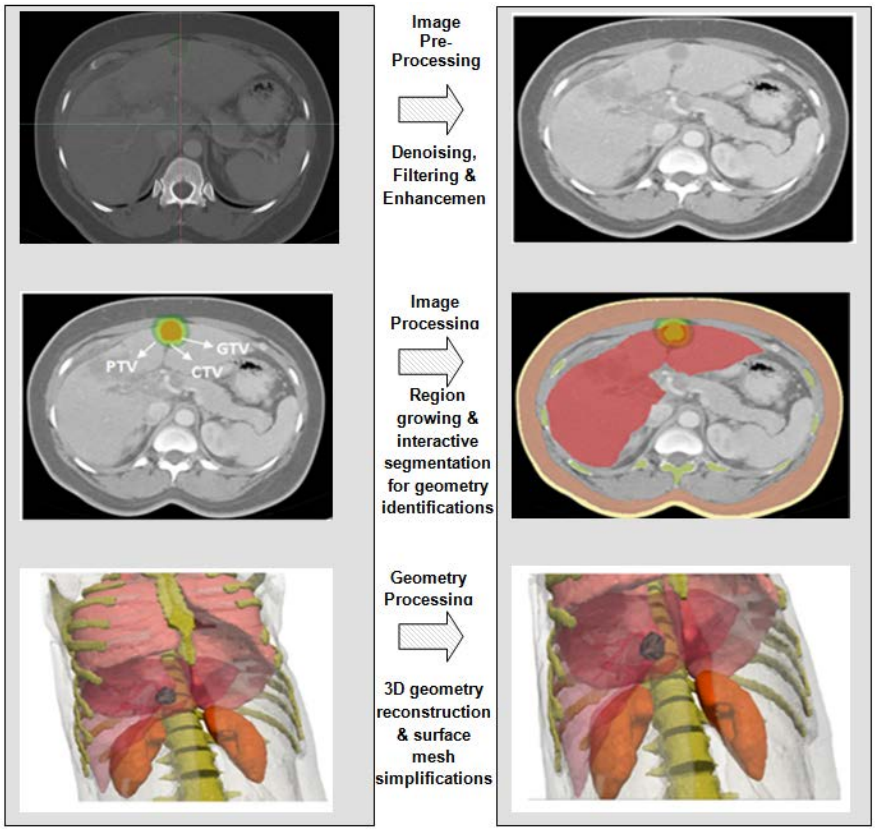

Figure 2.2. The 3D geometry construction process for electroporation treatment planning extracted from patient-specific computed tomography (CT) scan. The target treatment volumes(GTV, CTV, and PTV) were identified by the interactive segmentation tool, while the tissues were segmented by region growing algorithm. The 3D geometries were constructed by the surface editor-plug-in and marching cubes Algorithm[79]. *Note: The lung and kidney just for graphical illustration*

2.3.2 Electrode insertion and manipulation

In most cases, needle-shaped electrodes are employed in electroporation-based treatments for deep-seated tumors. In previous numerical studies, these electrodes are approximated by cylindrically shaped elements which are later modeled with simple polyhedrons [86].

We developed an electrode geometry plug-in that allows the user to build and modify needle electrode geometry through a mouse click on the position of insertion of the electrode tip. The plug-in allows the user to identify the electrode active length and diameter. Since the right electrode position and orientation has an important impact on the treatment efficacy, our tool employed a user-friendly electrode placement and manipulation plug-in, which allows the user to manipulate the electrode position and orientation. For this purpose, we included the VtkTransform filter and the vtkBoxwidgetTransform filter, by which user can translate the electrode position and change the electrode orientation.
The needle-shaped electrode is composed of two parts: an active conductive section and a passive insulating section. The insulating section (shaft) is not significantly relevant for the electric field computation. However, it is important to visualize it as the whole trajectory of needle-shaped electrodes is crucial in clinical scenarios. For instance, it is necessary to assess whether the electrode can be percutaneously introduced between two ribs.

2.4 Numerical Modeling of Electric Field Distribution

The electric field distribution can be calculated by the COMSOL Multiphysics finite element solver that is integrated into our treatment planning tool. COMSOL Multiphysics supports static, quasi-static, and fully dynamic analyses, and integrates equation systems and boundary conditions for a variety of physics. In addition, COMSOL includes the direct current (DC) conduction which is used for computing the electric field distribution and a Joule heating equation which is relevant for computing temperature increase which might cause thermal damage.
In electroporation treatment planning, the Laplace equation for electric potential is used for calculating the electric field in conductive media:

$$\nabla.(\sigma.\nabla\varphi) = 0 \qquad (1)$$

From which the electric field distribution can be determined by using the equation (2):

$$\mathrm{E} = -\ \nabla.\varphi\ . \qquad (2)$$

This equation has been numerically solved by the Comsol Multiphysics (Comsol, Stockholm, Sweden) finite element method solver.
In our prototype, we built an electroporation numerical modeling plug-in that act as Comsol model builder. Our plug-in allows the user to build the model geometry, to insert the electrodes, to set the material properties (Tissue conductivity), to set the potential between the electrodes array, to build the mesh, to run the finite element solver and finally to display the electric field distribution.

Furthermore, we incorporated the non-commercial meshing software package, Tetgen[117], to generate a volumetric mesh from an input surface mesh. This software was integrated with the simplifications and decimation algorithms for repairing the intersecting surface meshes that result, for instance, from the small edges, intersected elements, electrode penetrating other structures such as the outer boundaries of the domain. Typically, Comsol FEM solver provides more accurate results by discretizing the domain into the extremely fine mesh. After studying many possible refinements in the target domain, we found that extra fine mesh with minimum and maximum element size of $3e^{-4}$ and $7e^{-3}$mm, and maximum element growth rate of 1.35mm provides an accurate solution and with an acceptable use of computational resources.
It is worth mentioning that our plug-in runs the finite element solver in the backend without any user interaction with Comsol graphical user interface by integrating COMSOL model javascript generator. In addition, our plug-in is integrated within the 3D builder and the simplifications plug-ins to iteratively allow the user to simplify the 3D volume according to the FEM mesh needs. Moreover, the post-processing of the computed electric field is handled by vtk post-processing algorithms that are included in our software.

2.5 Results

In order to validate the performance of the platform prototype, a complete patient-specific treatment planning for an anatomically realistic study of human liver tumor was carried out. The study was performed on CT data set stored as DICOM images, 512 by 512 pixels with a 12-bit gray level resolution, 5mm interval and with 67 slides[118]. The computer used for runtime measures had Intel(R) Core(TM) i7-4770, 3.4GHz CPU, 8GB RAM and Windows 7 Professional operating system. The study performed in a typical clinical workflow as indicated in figure 2.1.
Figure 2.3. illustrates an example of a complete irreversible electroporation treatment planning processed by our prototype. The image pre-processing phase starts with CT DICOM image loading, enhancement and denoising without affecting image quality and edges. The performed pre-processing were processed independently which respectively corrected the non-uniform luminance noise, suppressed noise and enhanced contrast and brightness. The noise removal was performed by applying the ITK MedianImageFilter that is commonly used as a robust approach for noise reduction, mainly in the presence of gray-level outliers. Similar to radiotherapy procedure, segmentation of region of interest (ROI) could be achieved by use of: threshold segmentation, region growing and interactive segmentation tool. The three regions of interest (GTV, CTV and PTV) were segmented according to the treatment planning procedure. The GTV was contoured on the pre-processed CT

image. CTV was defined as the GTV+ 3mm margin, while the PTV was defined as GTV+5mm margin. The whole liver, bones and surrounding tissues (modeled as a combination of muscle, fat and body fluids) were also segmented. Moreover, the adjustment of the segmented regions and the removal of the unwanted leakage was carried by the manual segmentation tool.

The 3D geometry construction (see method section) from the 2D segmented regions was performed by Marching cube algorithm and surface mesh editor tool which is then simplified and decimated by using simplification algorithms and Tetgen volumetric mesh generator.

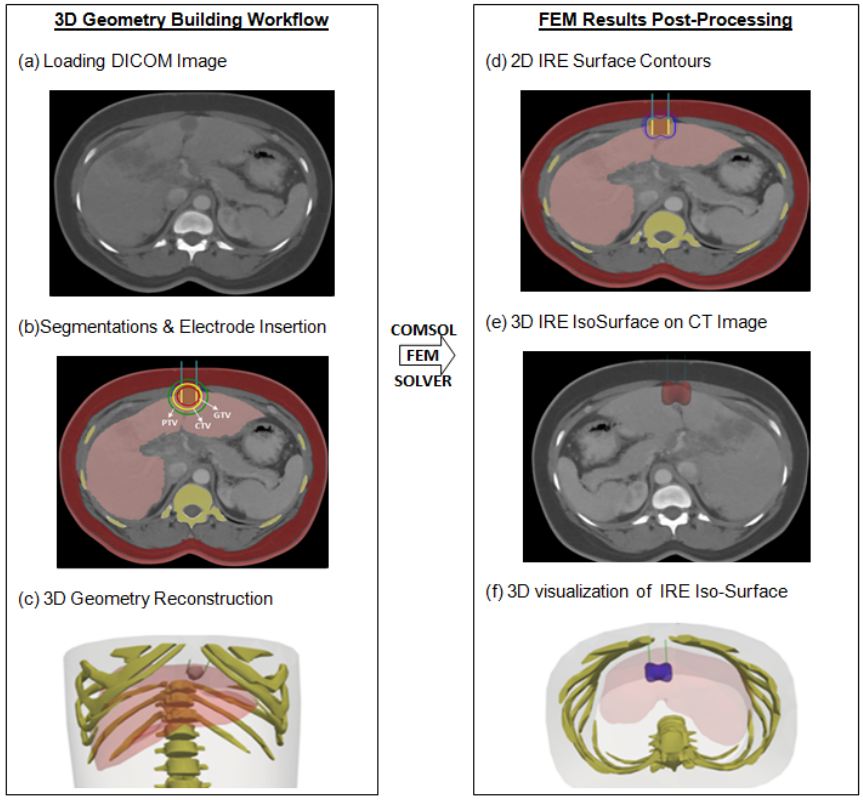

Figure 2.3. Simulation of human liver tumor case study by means of the treatment planning platform prototype.

The electrode insertions was carried by electrode insertion and manipulation plug-in. In this case study, two needle electrodes (1 mm diameter, 20mm active length, 20mm interelectrode and 3000 V applied potential) were inserted around the GTV as shown in figure 2.3. (c). The 3D geometries including the electrodes were added to the numerical modeling plug-in and combined as one unit geometry with different electrical properties. The tissues electric conductivity of bones,

surrounding tissues and liver were set to 0.02 S/m, and 0.2 S/m respectively; While these values were obtained from experimental data found in Gabriel et al.[97]. The GTV was given a liver tumor conductivity of 0.2S/m for the static model [119], while for the dynamic model was set as in [120] . The electric field distribution was calculated using the backend link with Comsol FEM solver.

Table 2.1. The estimated running time T (s) of a complete IRE treatment planning on a case study with liver tumor.

Treatment Planning Parameters	**Numerical Homogeneous -Static T (minutes)**	**Homogeneous - Dynamic T (minutes)**
Image-Preprocessing Time(s)	7	7
Segmentation of ROI (GTV,CTV and PTV)	43	43
3D Geometry construction	26	26
Geometry simplification	31	31
Building the numerical model	5	5
FEM solver estimated running time(s)	11	41
Overall estimated time (T)	**123**	**153**

The model simulation was performed twice in which homogeneous static conductivity model was used first , followed by the homogeneous dynamic conductivity model. In both runs, the estimated time for each step of the complete procedure was recorded and shown in Table 2.1. The complete treatment planning in both the homogeneous-static and homogeneous-dynamic models was performed in an average time of 123 and 153 minutes respectively. The increase in the running time of the dynamic model was mainly due to the non-linear change in conductivity during electroporation processes.

2.6 Discussion

We have presented an integrated software prototype to build a patient-specific electroporation treatment planning using the GIMIAS medical image analysis open source software and the Comsol finite element solver. Apart of the time consumed in the treatment planning process, our prototype produces an accurate calculation for electric field distribution in a single user friendly platform for clinical application.

The uses of GIMIAS open source clinical framework in the development of our prototype improved and facilitated the applications of the treatment planning procedure. We described the development environment with some detailed information that can help physician in understanding and using the prototype software in clinical applications.

The prototype treatment planning clinical workflow was implemented in similar procedures to radiotherapy and radiofrequency [77], [99], [110], [121], [122]. The patient-specific treatment planning procedure requires a medical image processing and analysis, 3D model construction, and numerical modeling for calculating the electric field distribution.

The prototype implementation on GIMIAS clinical framework provides physicians with a powerful medical image processing and analysis algorithms and tools. The image pre-processing was constructed in a sequential workflow steps where radiologist and physicians can get benefits from the set of predefined tools and algorithms for loading the DICOM images, reviewing, enhancing, filtering and denoising according to the image quality. The integration of DICOM plug-in simplified the pre-processing by automatically creating a volumetric image from the DICOM image and rendered it into the general scene view and it made it accessible by the implemented plug-ins.

In image processing, the implementation of ITK segmentation algorithms provides physicians with sets of automatic, semi-automatic and interactive algorithms that facilitate the identification and segmentation of ROI. Furthermore, the integration of measurement tool provides them with the ability to identify the distance margin between the GTV, CTV and PTV planning. The inclusion of ITK segmentation algorithms provides physicians with robust segmentation tool. However, incorporating fully automatic segmentation algorithms that can segment and interpolate through all image slices and reconstruct the 3D surface mesh improved the image processing and reduced the segmentation time.

The workflow of 3D model construction was developed in a systematic process in which physicians can reconstruct 3D mesh from the segmented ROI, edit the mesh, smoothing and optimizing the geometry curvature through the surface editor plug-in. The integrated tools for 3D mesh surface reconstruction and 3D volume constructions provide physicians with an efficient tool for building the FEM 3D model geometry.

The prototype allows physicians to compute the electric fields using the Comsol solver link without user interaction with Comsol graphical user interface, without the need to Matlab link, and demonstrates the results of electric field distribution over patient medical image on the prototype scene view. This helps physicians to optimize the treatment planning according to the treatment needs. It is worth noting here that once the model built and executed for the first time, physicians can optimize the treatment parameters and re-run them without need to rebuild the model. Thus, the process can be repeated according to the physicians need.
The use of medical image analysis and Numerical simulation of electric field distribution on a single platform helps physicians to build an efficient and accurate patient-specific treatment planning. Unfortunately, the current software prototype cannot perform real-time calculation of electric field distribution. The image analysis and the numerical modeling is a timely process and it may delay the treatment for hours or days in some cases. This motivates the idea of developing a fast treatment planning tool that can perform real time calculation for electric field distribution during clinical application. To this end, one of our future objectives is to develop a fast algorithm for calculating the electric field distribution in analytical approach rather than numerical approach, and with a simplified image processing and 3D model reconstruction procedures.

The presented prototype allows performing a complete treatment planning procedure in a single platform and on the same scene view, which is important for physicians in evaluating the treatment planning over the patient medical image prior the treatment. Furthermore, the prototype is able to perform post-processing of electric field distributions, where physicians can change the $E_{threshold}$ and visualize 2D and 3D plots over the medical image.

2.7 Conclusions

We introduced a software prototype of electroporation simulation and treatment planning tools which is a part of electroporation patient-specific therapy in clinical application. The prototype integrates the patient-specific treatment planning procedure in a clinical work flow structure in which 3D model reconstruction from patient medical image, electrode insertion and numerical calculation of electric field distribution are in a single platform.
The physicians can greatly benefits from the developed prototype by generating electroporation treatment planning on patient-image and evaluate and optimize the electric field distribution prior electroporation treatment. Moreover, it is possible to include the whole geometry in numerical simulation, which allows physicians to evaluate the electric field distribution in the healthy tissue and near the organs at risk.

Finally, the prototype was constructed in a clinical workflow according to electroporation treatment planning procedure, which is structured in a simple, understandable and user friendly form. The prototype provides physician with an efficient and accurate numerical calculation of electric field distribution based on patient medical image. Therefore, the developed prototype can contribute to improve and enhance the electroporation clinical applications. Despite of it is accuracy and efficiency; it is a timely procedure and does not support real-time electroporation treatment planning in clinical application.

CHAPTER 3

Impact of Liver Blood Vessels on Irreversible Electroporation Ablation

Abstract-

Irreversible electroporation is a novel tissue ablation technique which entails delivering intense electrical pulses to the target tissue, hence producing fatal defects in the cell membrane. The present study numerically analyzes the potential impact of liver blood vessels on ablation by irreversible electroporation because of their influence on the electric field distribution. An anatomically realistic computer model of the liver and its vasculature within an abdominal section was employed, and blood vessels down to 0.4 mm in diameter were considered. In this model, the electric field distribution was simulated in a large series of scenarios (n = 576) corresponding to plausible percutaneous irreversible electroporation treatments by needle electrode pairs. These modeled treatments were relatively superficial (maximum penetration depth of the electrode within the liver = 26 mm) and it was ensured that the electrodes did not penetrate the vessels nor were in contact with them. In terms of the total ablation volume, the maximum deviation caused by the presence of the vessels was 6%, which could be considered negligible compared to the impact by other sources of uncertainty. Sublethal field magnitudes were noticed around vessels covering volumes of up to 228 mm^3. If in the model the blood was substituted by a liquid with a low electrical conductivity (0.1 S/m) the maximum volume covered by sublethal field magnitudes was 3.7 mm^3 and almost no sublethal regions were observable. We conclude that undertreatment around blood vessels may occur in current liver ablation procedures by irreversible electroporation. Infusion of isotonic low conductivity liquids into the liver vasculature could prevent this risk.

The content of this chapter is adapted from the following published manuscripts

R. Qasrawi and A. Ivorra, "Impact of liver vasculature on electric field distribution during electroporation treatments : an anatomically realistic numerical study," in *6th European Conference of the International Federation for Medical and Biological Engineering*, 2014, pp. 573–576

L. Silve, R. Qasrawi, and A. Ivorra, "Incorporation of the Blood Vessel Wall into Electroporation Simulations," 1st World Congress on Electroporation and Pulsed Electric Fields in Biology, Medicine and Food & Environmental Technologies. Springer Singapore, 2016. pp. 1–4.

R. Qasrawi, L. Silve, and F. Burdı, "Anatomically Realistic Simulations of Liver Ablation by Irreversible Electroporation : Impact of Blood Vessels on Ablation Volumes and Undertreatment," Technology in cancer research & treatment (2017): 1533034616687477.

3.1 Introduction

Irreversible electroporation (IRE) is a relatively novel non-thermal ablation modality [10]. IRE is typically performed by inserting thin electrodes into the target tissue and delivering a number (8 to 100) of short (10 µs to 100 µs) high voltage pulses across the electrodes thereby producing field magnitudes in the tissue in an order of 1000 V/cm. These pulsed fields cause a large increase in cell membrane permeability to ions and macromolecules which fatally disrupts cell homeostasis [5].

Ablation of soft tumors by IRE has been demonstrated in a number of clinical studies[68],[70],[73][123], [124]. IRE ablation is not based on heating, which gives it two major advantages over other ablation modalities: 1) IRE does not destroy the extracellular matrix, and 2) IRE is insensitive to thermal sinks. These advantages imply that it is safe and physically possible to use IRE to treat tissues which are in close proximity to vital vessels or are in contact with them. The first advantage implies that it is safe to perform IRE ablation in the vicinity of vital vessels because the structural properties of those vessels are preserved [73], [125]. It is even possible to directly treat arteries without compromising their fluidic function[126]. The second advantage implies that it is physically possible to perform IRE ablation in the vicinity of large blood vessels[58][127]. In contrast to other ablation modalities based on heating or freezing, the thermal sink effect produced by large blood vessels does not hinder IRE ablation. From this last feature, it may be mistakenly concluded that the presence of blood vessels is irrelevant for IRE ablation. A subjacent objective of the present work was to illustrate that this is not the case.

IRE's effectiveness depends on the temporal features of the sequence of pulses, but for a given set of temporal features (number of pulses, pulse duration, and repetition frequency), it is accepted that local IRE effectiveness depends mainly on the local field magnitude; an electric field threshold for IRE is typically defined for each tissue type and pulse protocol[128]. Therefore, any factor that may have an impact on the electric field distribution may have an impact on the ablation. In the case of the liver – which tends to be considered as homogenous in electrical terms – one of those factors may be the contrast in electrical conductivity between the liver parenchyma and the interior of the blood vessels. Indeed, recent numerical studies[102],[129],[130] and *in vivo* studies [104] have revealed that this sort heterogeneity may have a significant impact on IRE ablation. However, to the best of our knowledge, its impact on liver ablation has been neither observed clinically nor assessed for clinical relevance through numerical studies.

The purpose of the study reported here is to numerically analyze and quantify the potential impact of liver blood vessels on ablation by

irreversible electroporation (IRE) due to their influence on the electric field distribution.

3.2. Materials and Methods

An anatomically realistic computer model of a male human liver, its blood vessels (down to 0.4 mm in diameter), bones and surrounding tissues was employed in this study. The 3D anatomical geometry was developed by the Korea Institute of Science and Technology Information[131]. The geometry was decimated and prepared for simulation using the Graphical Interface for Medical Image Analysis and Simulation (GIMIAS) software platform developed by the Center for Computational Imaging and Simulation Technology in Biomedicine (CISTIB) at the Universitat Pompeu Fabra [114]. The main geometrical features of the modeled liver and its vasculature are indicated in Table 3.1.

Table 3.1. Geometrical measurements of the liver and the vessels used in this study

Blood Vessels	**Diameter**		**Length**	**Volume**
	Min(mm)	**Max (mm)**	**(X,Y,Z)(mm)**	**(ml)**
Left vein	1.4	10.9	95.0, 79.6, 60.6	5.3
Left duct	0.4	4.4	122.3, 46.7, 39.6	0.6
Left artery	0.5	2.9	6.3, 30.8, 19.8	0.6
Middle vein	1.2	13.2	63.0, 80.7, 74.4	5.3
Right vein	0.8	14.2	93.3, 62.5, 121.2	7.3
Right duct	0.5	5.1	33.0, 69.3, 60.4	0.3
Right artery	0.4	3.0	50.3, 22.9, 36.7	0.3
Portal vein	1.2	18.3	130.4, 114.4, 88	9.6
Liver	-	-	**230.9, 170.5, 161.8**	**1514.3**

Electroporation across pairs of needle probes was simulated. The two probes of the pair were parallel and aligned so that they would form the opposite sides of an imaginary rectangle. Six arbitrarily chosen locations and four separations (10, 15, 20 and 25 mm) per location were assayed. These locations correspond to probe insertions through the anterior part of the abdomen. Figure 3.1. shows the anatomic model together with the assayed locations (separation = 25 mm). Each needle probe, with a diameter of 1 mm, consisted of a passive shaft (length = 40 mm) and an active part (i.e. the electrode) with a length of 10, 15, 20, or 25 mm. The penetration depth of the pair was adjusted to ensure a complete and superficial insertion of the active part into the liver with a maximum proximal distance of 1 mm from the surface of the liver. This resulted in a maximum penetration depth of 26 mm within the liver.

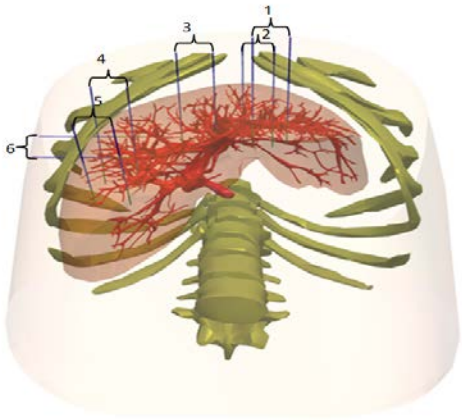

Figure 3.1. 3D geometrical representation of the 6 insertion locations assayed for the electrode pairs (in this case the interelectrode spacing is 25 mm and the electrode length is 25mm).

Electrode locations were carefully checked for ensuring that the electrodes neither penetrated the vessels nor were in contact with them. It was ensured that the minimum distance between the electrodes and any vessel was 0.2 mm. It was also ensured that the probes did not go through bone tissue. If these conditions were not met, the location of the probe pair was randomly modified a few millimeters (<5 mm) maintaining the above constraints regarding parallelism, separation and penetration depth.

For each model (homogeneous and non-homogeneous) three voltages across the two electrodes were assayed: 2000, 2500 and 3000 V. The total number of simulated cases for each model was 288 (6 locations × 4 separations × 4 electrode lengths × 3 voltage magnitudes). The electric field threshold for effectively irreversible electroporation was considered to be 700 V/cm (2, 15, and 20).

The 3D geometry was imported into COMSOL Multiphysics 4.3a (COMSOL AB, Stockholm, Sweden). The entire geometry was meshed using the COMSOL Multiphysics regular refinement method user controlled tetrahedral mesh with a minimum element size of 0.1 mm. The total number of elements was above 2,200,000.

The electric field distribution was computed using the 'Electric Currents (ec)' application mode of the AC/DC module of COMSOL. As in previous studies (15, 21-24), non-linear behavior was assumed for the hepatic tissue in order to model the increase in tissue electrical conductivity during pulse delivery due to electroporation. This behavior was modeled with the following sigmoid equation describing the dependence of tissue conductivity (δ) of electric field magnitude ($|\vec{E}|$):

$$\sigma = \sigma_0 + [(\sigma_f - \sigma_0)\frac{1}{1+e^{-\frac{|\vec{E}|-T}{W}}}] \quad (1)$$

Where $\sigma_0$is the conductivity of the tissue when no field is applied (i.e. initial conductivity), σ_f is the maximum conductivity the tissue can reach due to electroporation (i.e. final conductivity), and T and W are two parameters that describe the morphology of the sigmoid (coarsely, inflection magnitude and slope respectively). The set of values used for the hepatic tissue model was: σ_0 = 0.2 S/m, σ_f = 0.5 S/m, T = 950 V/cm and W = 200 V/cm. These values would correspond to hepatic tumors and have been inferred from experimental data in Prakash et al.[119]. The values for healthy (normal) liver tissue would be σ_0 = 0.05 S/m, σ_f = 0.3 S/m, T = 950 V/cm and W = 200 V/cm; also inferred from data in Prakash et al. [119]. This set of values was also assayed in this study and the results obtained are reported as supplementary material. We deemed it more realistic to model tumor properties rather than healthy liver properties because IRE treatments mostly occur on tumor tissues (i.e. the electrodes are inserted into the tumors).

The electrical conductivity of the other tissues was modeled as field independent. The conductivities of the vessels (modeled as blood containers), bones and soft tissues filling the anatomy (modeled as a combination of muscle, fat and body fluids) were 0.7 S/m, 0.02 S/m, and 0.2 S/m respectively; these values were obtained from experimental data found in Gabriel et al.[97] . Conductivity values of the electrodes and the passive shafts were set to 1×10^5 S/m and 1×10^{-5} S/m respectively.

For each case, a simulation was performed assuming the presence of the vasculature ($\sigma_{vessels}$ = 0.7 S/cm) and another one was performed under the assumption that the liver was homogenous ($\sigma_{vessels}$= σ_{liver}). Both solutions were then compared. First, the size of the ablation volumes was compared (regions in which $|\vec{E}|$ > 700 V/cm). It was then checked whether there were any regions in the ablation volume predicted with the homogeneous assumption ($\sigma_{vessels}$= σ_{liver}) that were not included in the ablation volume predicted with the heterogeneous assumption ($\sigma_{vessels}$ = 0.7 S/cm). That is, the solution of the homogeneous assumption was considered to be the target volume and it was checked whether the blood vessels caused undertreatment within that volume.

In addition to the above referred systematic study with 288 cases, for graphical illustration, two hypothetical treatment cases were simulated to emphasize the impact of undertreatment around vessels. First, case H1 was simulated in which the presence of a tumor ($20.7 \times 19 \times 10$ mm^3) was modeled at a distance of 0.3 mm away from the right hepatic vein (Figure 3.2.(a)). In this case, the distinctive conductive properties of the liver and of the tumor were modeled according to the tumor conductivity models and parameters described above. The second case (case H2), the impact of

blood vessels on the IRE treatment was assessed by inserting the pair electrodes (active part =25mm and passive shaft =50 mm) deep into the liver with a maximum penetration depth of 65mm. The electrodes were located 1 mm from the right hepatic vein and the portal vein which are 10.2 mm and 14.6 mm in diameter respectively, and 3 mm from the middle hepatic vein which is 8.1 mm in diameter.
Furthermore, as it is common to employ more than two electrodes in IRE treatments, additional simulations were performed using three-electrode and four-electrode arrays. For each array model (homogeneous and non-homogeneous) two active length used (20 and 25mm), two interelectrode spacing (20 and 25mm) and three voltages across the electrodes pairs (2000, 2500 and 3000V). The total number of simulated cases for each array model was 12 (2 separations × 2 electrode lengths × 3 voltage magnitudes).

3.3. Results

3.3.1 Simulations indicate that undertreatment may appear around vessels

Figure 3.2.(a) shows the geometry of the modeled hypothetical treatment of a tumor (case H1) and Figures 3.2.(b) and 3.2.(c) show a cross section of the corresponding simulated electric field magnitude assuming that the liver is homogeneous ($\sigma_{vessels} = \sigma_{liver} \neq \sigma_{tumor}$) and that it is heterogeneous ($\sigma_{vessels} = 0.7$ S/cm $\neq \sigma_{liver} \neq \sigma_{tumor}$) respectively. It can be observed that for the homogeneous case (Figure 3.2.b) the treatment volume (regions in which $|\vec{E}| > 700$ V/cm) well covers the tumor (voltage across electrodes = 2000 V). However, once the blood vessels are modeled (Figure 3.2. (c)), the electric field distribution is distorted around them. In particular, it could be noticed that there is a tumor region close to the right hepatic vein (lower vessel) in which the electric field is significantly below 700 V/cm.

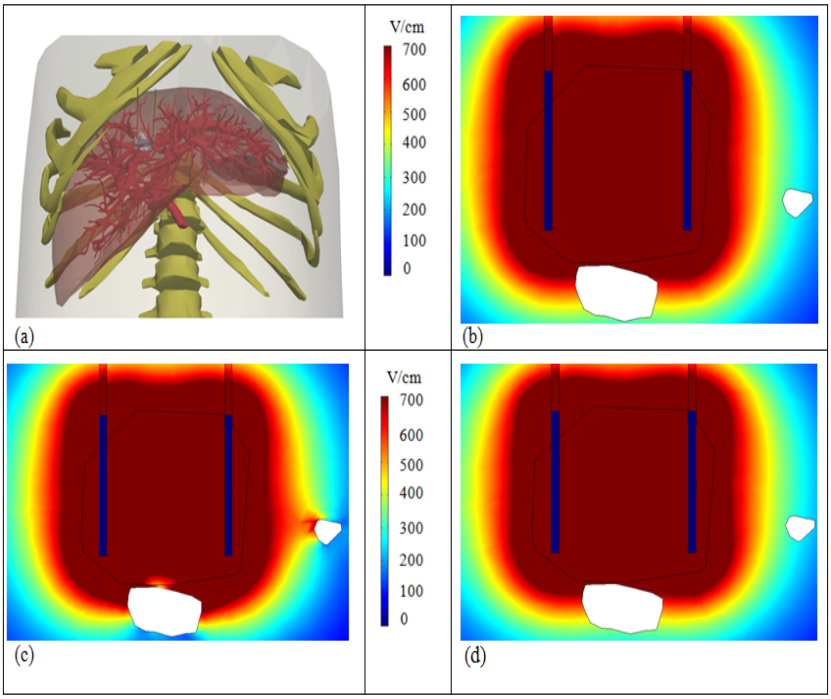

Figure 3.2. X-Y plane plot of electric field magnitude during hypothetical treatment of a tumor. (a) The 3D geometry model. (b) The homogeneous model ($\sigma_{vessels} = \sigma_{liver} \neq \sigma_{tumor}$) result. (c) The non-homogeneous model ($\sigma_{vessels} = 0.7$ S/m $\neq \sigma_{liver} \neq \sigma_{tumor}$) result. (d) Result when the vessel is filled with a low conductivity fluid ($\sigma_{vessels} = 0.1$ S/m $\neq \sigma_{liver} \neq \sigma_{tumor}$) .

3.3.2. Impact of vessels on the treated volume

Table 3.2. shows the result of volume analysis for the 576 simulations (288 homogeneous and 288 non-homogeneous). The average treated volume (regions in which $|\vec{E}| > 700$ V/cm) is indicated for the two conductivity models (homogenous and heterogeneous), the six assayed locations and for every combination of electrodes separation distances, active lengths and voltages. In addition, out of the six assayed locations, the maximum relative difference between the two conductivity models is indicated.

Table 3.2. Average of treatment volumes in mm^3 (for six locations) and the maximum percentage deviation between homogeneous and non-homogeneous models.

AL	Space	3000 V			2500 V			2000 V		
		NHT	HT	NHT (%D)	NHT	HT	NHT (%D)	NHT	HT	NHT (%D)
10	10	3.98	4.00	1.27	3.19	3.22	1.59	2.39	2.42	2.55
	15	4.76	4.83	3.43	3.86	3.91	2.81	2.56	2.59	2.39
	20	5.06	5.05	0.48	3.49	3.49	2.15	2.10	2.09	2.74
	25	4.35	4.33	2.70	3.00	2.96	2.75	2.06	2.01	4.37
15	10	5.43	5.46	1.22	4.34	4.38	2.29	3.28	3.32	1.83
	15	6.50	6.47	5.20	6.22	6.29	2.78	3.81	3.83	2.55
	20	7.67	7.70	1.72	5.23	5.22	1.19	3.01	3.02	1.47
	25	6.56	6.54	1.47	4.32	4.29	0.92	2.62	2.61	0.87
20	10	7.04	7.05	0.45	5.66	5.68	0.84	4.28	4.28	0.86
	15	8.68	8.73	0.93	6.80	6.80	0.87	4.82	4.82	0.58
	20	9.31	9.51	3.69	6.68	6.85	4.05	3.88	3.96	2.62
	25	8.83	8.94	4.24	5.50	5.57	4.02	3.25	3.25	2.10
25	10	8.57	8.63	2.19	6.91	6.95	1.86	5.26	5.28	1.26
	15	10.07	10.05	4.05	8.19	8.22	2.17	6.12	6.13	2.79
	20	11.26	11.54	5.14	8.28	8.49	5.41	5.06	5.18	3.21
	25	10.99	11.17	2.62	6.94	7.10	6.04	3.88	3.90	4.84

Note: AL: electrode active length; NHT: Non-Homogeneous Tumor tissue, HT: Homogeneous Tumor tissue, (%D): maximum percentage deviation between the homogeneous and the nonhomogeneous cases.

The simulation results indicate that there are differences between homogeneous and non-homogeneous cases regarding the treated volume. It can be observed that the average integrated volume in cm^3 increases as electrode depth, spacing, and applied potential increase. The maximum percentage deviation of the tumor models ranged from 0.5% up to 6%.

3.3.3. Undertreatment volume quantification

The volume of tissue subjected to undertreatment because of the presence of blood vessels (heterogeneous case) was quantified by estimating the integrated volume inside the target region (regions in which $|\vec{E}| > 700$ V/cm for the homogeneous case) which had an electric field magnitude below 700V/cm. Results in Table 3.3. show the minimum, maximum and average undertreatment volumes in mm^3 for the various electrode

configurations (15-25 mm depth, 10-25 mm spacing, and 3000-2000 V applied potential).

The results in Table 3.3 indicate that the minimum and maximum undertreatment volumes found for the 10, 15, 20 and 25 mm active lengths were (0- 68.7), (0-120.8), (0- 224.7) and (1.4- 227.7) mm^3 respectively. In some cases, in which the electrodes were inserted near very small vessels or > 10 mm away from vessels with diameters ranging from 2 to 8 mm, the undertreatment volume was close to 0 mm^3.

Table 3.3. Volumes of tissue subjected to undertreatment (cm^3) because of the presence of blood vessels

Active length	Space	3000 V			2500 V			2000 V		
		Min	**Max**	**Mean**	**Min**	**Max**	**Mean**	**Min**	**Max**	**Mean**
10	**10**	0.0	31.8	19.5	19.2	35.2	28.3	0.0	26.6	14.4
	15	0.0	68.7	30.7	0.0	62.8	27.7	0.0	33.0	13.3
	20	1.6	6.3	4.1	0.0	7.0	4.1	0.0	11.9	4.1
	25	0.0	7.0	3.7	0.0	4.8	2.4	0.0	5.0	2.4
15	**10**	0.0	15.4	7.4	0.0	11.2	5.3	0.0	5.8	2.6
	15	61.9	120.8	97.3	21.3	81.9	51.4	0.0	30.4	20.1
	20	9.3	27.1	19.6	0.0	30.6	15.1	0.0	25.0	11.8
	25	1.7	22.8	10.8	0.0	7.9	2.9	0.0	4.5	1.7
20	**10**	0.0	43.3	18.4	0.0	28.0	14.5	0.0	20.9	12.9
	15	0.0	44.2	26.4	0.0	40.3	17.2	0.0	25.2	12.2
	20	62.7	224.7	111.4	50.4	201.7	96.8	24.4	112.1	61.5
	25	1.2	159.4	82.9	0.0	109.6	50.0	0.0	63.2	28.6
25	**10**	11.3	36.4	21.0	5.4	40.8	21.4	5.5	33.8	18.6
	15	5.6	119.5	47.5	1.8	65.9	38.3	1.4	38.4	17.9
	20	84.2	227.7	139.9	72.9	210.6	128.2	36.2	134.0	74.8
	25	74.5	182.6	112.2	27.4	155.3	66.6	11.3	50.2	27.3

Note: Min: Minimum, Max: Maximum.

Figure 3.3. illustrates two cases of undertreatment around the vessels. The green regions represent the isosurfaces of treatment ($|\vec{E}|$ = 700 V/cm) for the homogeneous model. The undertreatment regions ($|\vec{E}|$ < 700 V/cm) for the heterogeneous models are depicted in blue.

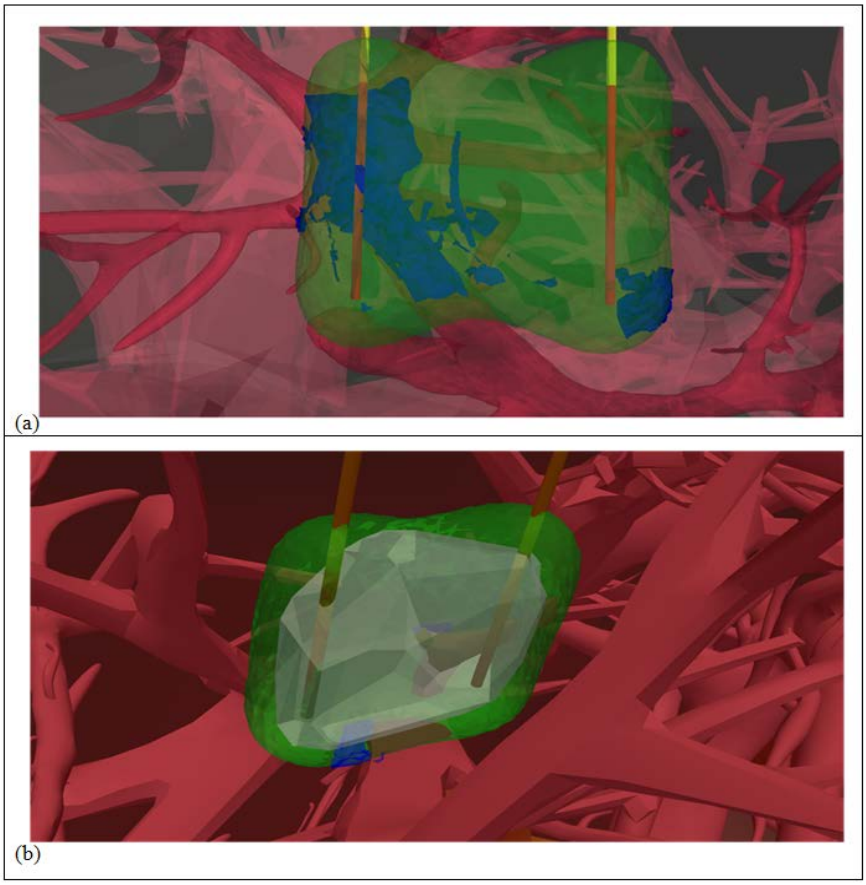

Figure 3.3. 3D volume plot of vessels (red), homogeneous treatment region (green), tumor region (gray, only in b) and untreated spots (blue). (a) Deep treatment of liver (no tumor) close to the right hepatic vein and the portal vein with 25mm electrode active length and spacing, and 3000V applied potential. (b) Tumor case study close to vessels with 15mm active length, 14mm spacing, and 2000V applied a potential (case 2D illustrated in figure 3.2.(c).

The result depicted in Figure 3.3. (a) (case H2) corresponds to the largest undertreatment volume found heuristically when very deep ablations were assayed. The numerical results corresponding to this case shown in figure 3.3. (a) indicate that the undertreatment volume was 1049, 731.6, and 313.2 mm^3 for the 3000, 2500, and 2000 V applied potentials respectively.

3.3.4. Simulated probability of undertreatment

The event rate of undertreatment was estimated from the 288 simulated cases, and it was considered to occur when there was at least an undertreated region ($|\vec{E}|$ < 700 V/cm) with a volume $\geq 1\ mm^3$ found

within the IRE treatment region ($|\vec{E}|$ > 700 V/cm for the homogeneous case).

Table 3.4. Number of cases of undertreatment (undertreated volume $\geq 1 mm^3$) out of the 6 assayed insertion locations

Electric Potential(V)	Active length (mm)	Space(mm)			
		10	**15**	**20**	**25**
2000	**10**	2/6	2/6	2/6	3/6
	15	2/6	2/6	3/6	3/6
	20	3/6	4/6	4/6	4/6
	25	3/6	4/6	4/6	5/6
2500	**10**	2/6	2/6	3/6	3/6
	15	2/6	3/6	3/6	4/6
	20	4/6	4/6	5/6	6/6
	25	5/6	5/6	6/6	6/6
3000	**10**	3/6	2/6	4/6	4/6
	15	3/6	4/6	5/6	6/6
	20	4/6	5/6	5/6	6/6
	25	5/6	5/6	6/6	6/6

The results in Table 3.4. indicate that the minimum and maximum probability of having undertreatment volume ($\geq 1\ mm^3$) found for the 10mm active length electrode was (2/6 - 4/6) and for the 15, 20 and 25 mm active lengths electrodes were (2/6 - 6/6).

Furthermore, it was found that the presence of vessels with a diameter ≥ 3mm within the target region always produced at least a region of undertreatment with a volume $\geq 1\ mm^3$.

3.3.5. Three and Four-Electrode Arrays

In order to be further relevant to clinical treatment, we simulated three-electrode and four-electrode arrays with the various electrode configurations (20-25 mm depth and 15-25 mm spacing). This was performed by applying 2000, 2500, and 3000V to the possible electrode sets and between the two diagonal pairs.

The result depicted in Figure 3.4. shows four possible treatment planning approaches for the targeted tumor in case H1 depicted in Figure 3.2. Figure 3.4.(a) shows the result of a 2-electrode model with 15mm active length. The distortion on the electric field distribution is clearly observed around the blood vessels. Figure 3.4.(b) shows the result of four-electrode array simulation with 15mm active length. It can be observed that the four-electrode array increased the treatment zone and reduced the undertreatment region, however, a small area of electric field distortion

was still noticed around the vessel. Figure 3.4.(c) shows the simulation result of three-electrode array simulation with 20mm active length. It can be observed that the increase of active length increased the treatment region; nonetheless, a small region of electric field distortion is also clearly noticed around the vessels. The result depicted in Figure 3.4.(d) shows the result of low conductivity liquid infusion (0.1S/m); see next section. A uniform electric field distribution was produced and it was noticed that the undertreatment region around the vessels was completely covered.

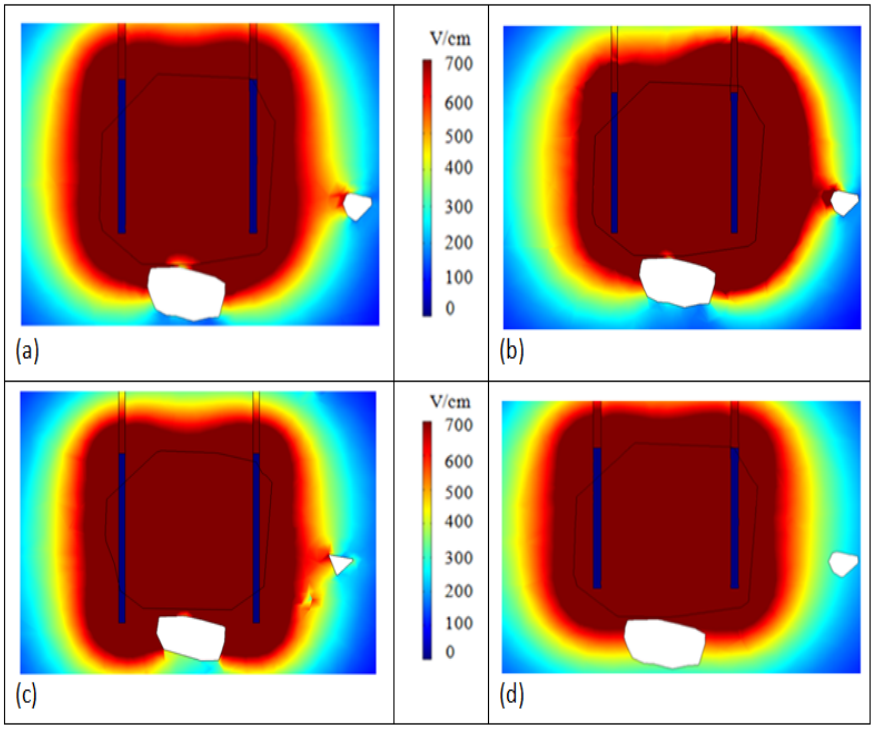

Figure 3.4. The X-Y plane plot of electric field magnitude during hypothetical treatment of a tumor. (a) The non-homogeneous model ($\sigma_{vessels}$ = 0.7 S/m ≠ σ_{liver} ≠ σ_{tumor}) two 15mm electrodes model result. (b) The non-homogeneous model ($\sigma_{vessels}$ = 0.7 S/m ≠ σ_{liver} ≠ σ_{tumor}) four 15mm electrodes model result. (c) The non-homogeneous model ($\sigma_{vessels}$ = 0.7 S/m ≠ σ_{liver} ≠ σ_{tumor}) three 20 mm electrodes model result. (d) The result of two 15 mm electrodes model when the vessel is filled with a low conductivity fluid ($\sigma_{vessels}$ = 0.1 S/m ≠ σ_{liver} ≠ σ_{tumor}).

Furthermore, we repeated the simulation of the maximum undertreatment volumes found in our study with three electrodes and four-electrode arrays in order to assess the impact of these approaches on the undertreatment volumes. The results depicted in Table 3.5. shows the maximum undertreatment volume found in the repeated simulations. The maximum

undertreatment volumes found for the 20 and 25 mm active lengths were (227.7), (291.9) and (215.7) mm^3 for 2, 3 and 4 electrode arrays respectively. In cases where the electrodes were inserted near a heavy set of vessels, a larger undertreatment volume was sometimes found.

Table 3.5. Volumes of tissue subjected to undertreatment because of the presence of blood vessels of different treatment approaches

Active length (mm)	Spacing (mm)	Potential (V)	1Probes Max (mm^3)	3Probes Max (mm^3)	2Probes Max (mm^3)	Saline Infusion (0.1S/m) Max (mm^3)
20	20	2000	112.1	108.1	43.9	0
		2500	201.7	160.4	87.5	0
		3000	224.7	254.3	160.3	2.1
	25	2000	63.2	54.2	15.1	0
		2500	109.6	87.8	32.2	0
		3000	159.4	142.6	66.7	0
25	20	2000	134.0	68.1	32.7	0
		2500	210.6	157.4	48.2	0
		3000	227.7	291.9	215.7	0
	25	2000	50.2	80.1	32	1.1
		2500	155.3	118.5	28.9	1.8
		3000	182.6	148.2	39.6	2.4

3.3.5. Simulated potential benefit of infusing low conductivity fluids into liver vasculature for preventing undertreatment

In order to prevent undertreatment due to the heterogeneity conductivity caused by the liver vessels, we propose to inject the blood vessels with a low conductivity liquid so that the tissues become more homogeneous in terms of conductivity. Figure 3.2. (d) illustrates that the electric field distribution obtained with a model in which the vessel has a conductivity of 0.1 S/m is almost indistinguishable when compared to that obtained with the homogenous model. More importantly, the region of tumor undertreatment observed in Figure 3.2. (c) disappears in Figure 3.2. (d).

The results in Table 3.6. indicate that by reducing the modeled conductivity of blood vessels, the size of the undertreated volumes is extremely reduced and in most cases, undertreatment is not noticeable at all. The event rate of undertreatment is reported in Table 3.7. when the conductivity of the vessels is set to 0.1 S/m rather than 0.7 S/m.

Table 3.6. Average undertreated volume (mm^3) for different electrical conductivities of the liver vessels

Active length (mm)	Space (mm)	3000V		2500V		2000V	
		0.7 (S/m)	0.1 (S/m)	0.7 (S/m)	0.1 (S/m)	0.7 (S/m)	0.1 (S/m)
10	10	31.8	0.0	35.2	0	26.6	0
	15	68.7	0	62.8	0	33.0	0
	20	6.3	0	7.0	0	11.9	0
	25	7.0	3.7	4.8	1.6	5.0	2.5
15	10	15.4	0	11.2	0	5.8	0
	15	120.8	0	81.9	0	30.4	0
	20	27.1	2.8	30.6	0	25.0	0
	25	22.8	0	7.9	0	4.5	0
20	10	43.3	0	28.0	0	20.9	0
	15	44.2	0	40.3	0	25.2	0
	20	224.7	2.1	201.7	0	112.1	0
	25	159.4	0	109.6	0	63.2	0
25	10	36.4	0	40.8	0	33.8	0
	15	119.5	0	65.9	0	38.2	0
	20	227.7	0	210.6	0	134.0	0
	25	182.6	2.4	155.3	1.8	50.2	1.1

Table 3.7. A number of cases of undertreatment (undertreated volume $\geq 1mm^3$) out of the 6 assayed insertion locations when the conductivity of the vessels is 0.1 S/m.

Electric Potential(V)	Active length (mm)	Space(mm)			
		10	**15**	**20**	**25**
2000	**10**	0/6	0/6	0/6	2/6
	15	0/6	0/6	0/6	0/6
	20	0/6	0/6	0/6	0/6
	25	0/6	0/6	0/6	1/6
2500	**10**	0/6	0/6	0/6	1/6
	15	0/6	0/6	0/6	0/6
	20	0/6	0/6	0/6	0/6
	25	0/6	0/6	0/6	0/6
3000	**10**	0/6	0/6	0/6	1/6
	15	0/6	0/6	2/6	0/6
	20	0/6	0/6	2/6	0/6
	25	0/6	2/6	2/6	2/6

3.4 Discussion

Complete ablation of viable tumor cells by achieving an adequate electric field distribution is the purpose of IRE treatment planning. Thus, understanding the impact of the treatment area characteristics, the electric conductivity heterogeneities in particular, on the electric field distribution is crucial to achieving optimal treatment. In this study, the impact of blood vessels in the treatment zone was examined in a realistic anatomical model consisting of liver, blood vessels, bones and surrounding tissues which were obtained from human male CT imaging. In earlier studies, it has been found that large blood vessels, because of their high conductivity, may interfere with electric field coverage of tumors in liver [102],[129],[130] described the impact of blood vessels on electric field distribution of IRE treatment. In which they experimentally demonstrated the need to increase the baseline field intensity around large vessels. Unsurprisingly, our study found that the distortion produced by the conductivity heterogeneity caused by the presence of a blood vessel was dependent on the vessel diameter and on the electrode's distance to the vessel. This is in agreement with other previous studies [130],[132],[122].
In the present study, we have modeled the blood vessels as simple containers of blood. That is, they were modeled as homogeneous regions of higher electrical conductivity than the liver parenchyma. Unfortunately, our data model didn't support the inclusion of vessels wall. Furthermore, the thickness of vessel walls varies enormously around arteries and veins let alone variability in the structure of veins and arteries. The lack of existing data about vessel walls as well as the non-uniform geometry

distribution of vessels limited the possibility of adding accurate vessel walls around our data model. However, to validate this simplification, an additional group of simulations was repeated with the inclusion of a 1 mm vessel wall around large hepatic veins and portal vein, as described in our previous study[133]. The results of these simulations are included in the supplementary materials (Figure 3.1. and Table 3.7.). The results show that the presence of the wall reduces the influence of blood on the electric field distribution and the undertreatment volumes. However, the relative difference in undertreatment volume compared to the results reported here does not exceed 21%.

In terms of treatment volume size (Table 3.2.), our results indicate that the impact of blood vessels will be mild for superficial liver IRE treatments. The maximum deviation in volume we observed was only 6%, which can be perceived as almost negligible if other confounding factors that influence the outcome of IRE are considered. For instance, tolerances when placing the electrodes are likely to cause a larger error in treatment planning. On the other hand, the observed regions of undertreatment around the blood vessels represent a potentially grave issue. We observed undertreatment in 65% of the analyzed cases (Table 3.4.). This high incidence rate would increase if deeper treatments – such as the ones represented in Figure 3.3. – were analyzed because the electrodes would be closer to even larger vessels. Therefore, we deem that undertreatment is likely to occur in current IRE liver treatments. It must be noted that IRE is particularly prescribed for ablations close to vessels because in those scenarios other ablative techniques based on temperature are not usable[134]. Whether undertreated regions of only 1 mm^3 represent a real clinical threat is still debatable, particularly because in our analysis undertreatment typically occurred at the periphery of the target volume and it must be presumed that in clinical IRE these locations would correspond to the safety margins considered during treatment planning. However, undertreatment certainly should be a matter of concern because any tumor cell left viable is a new potential tumor nodule. Furthermore, it must also be taken into account that we obtained much larger volumes of undertreatment, reaching up to 228 mm^3 (Table 3.3.). Therefore, although to the best of our knowledge no clinical cases of recurrence after hepatic IRE have been reported that were directly linked to undertreatment around vessels, we advise practitioners of liver IRE to carefully monitor any possible signs of recurrence around vessels during post-treatment follow-ups. Again it is convenient to note that undertreatment around vessels has been experimentally reported by Golberg et al. [130].

Different treatment planning approaches were included in our simulation in order to be more relevant to clinical applications. Three-electrode and four-electrode arrays were simulated. Our results show an increase in the treatment zones and a decrease in the size of undertreatment volumes

(Table 3.5.). The four-electrode array produced a larger treatment zone similar to the reported results in Applebaum et al. [58].
In order to prevent undertreatment due to the presence of vessels, we propose to replace blood in the liver vessels with an isotonic low conductivity liquid – such as a mixture of normal saline and dextrose 5% – so that the tissues are made more homogeneous in terms of conductivity. Our results indeed showed a huge improvement regarding cases of undertreatment (Table 3.7.) and regarding the size of the undertreated regions (Table 3.6.) when the conductivity of the vessels is set to 0.1 S/m. Similar results, not reported here, were obtained with higher (0.2 S/m) and lower (0.05 S/m) conductivities.

Delivery of low conductivity liquids into the liver vasculature could be performed either directly through percutaneous trans-hepatic portal catheterization (PTPC), which has been used for islet transplantation[135], or through hepatic vascular exclusion (HVE) maneuvers by deploying clamps through laparoscopy[135]. It is worth noting that total HVE (THVE) has been used for gene therapy[136] or to improve the pharmacokinetics of chemotherapeutic drugs [137]. Several low conductivity solutions could be employed with a reasonable margin of safety[138],[139],[140]. In particular, by diluting one part of normal saline (0.9% NaCl, $\sigma_{37^{o}C}$ = 1.5 S/m) in fourteen parts of dextrose 5% ($\sigma_{37^{o}C}$ < 0.01 S/m) an isotonic solution with a conductivity of about 0.1 S/m would be obtained. Note that, if the delivery technique does not substitute the blood but merely dilutes it, then the conductivity of the injected liquid would have to be adjusted to a lower value so that the resulting mixture had an adequate conductivity (0.1 S/m).

3.5 Conclusion

Due to their impact on electric field distribution, liver blood vessels may have an impact on IRE treatments in terms of treatment volume size and shape. This numerical study shows that the impact of blood vessels occurs around the medium size vessels and on the periphery of the treatment region, which may sufficiently distort the electric field distribution that resulted in undertreatment regions, with the potential effect on the quality of IRE cancer treatment. According to the reported results, the frequent random positions with different electrode settings indicated that the probability of undertreatment could occur frequently in hepatic IRE treatments. These undertreatment regions correspond to areas where the applied electric field is potentially sub-lethal. Therefore, caution is advised due to the possibility of these undertreated volumes to become new tumor nodules. This risk could be minimized by replacing blood in the liver vasculature, or by diluting it, with isotonic low conductivity liquids.

3.6 Supplementary Material

Table 3.8. Average of treatment volumes (cm^3) and the maximum percentage deviation between homogeneous and non-homogeneous models. Considering in the model the electrical conductivity of healthy (normal) liver.

AL	Space	3000 V			2500 V			2000 V		
		NH	HN	NH (%D)	NH	HN	NH %D	NH	HN	NH %D
10	10	4.7	4.8	2.3	3.7	3.8	3.0	2.8	2.9	3.3
	15	5.8	5.9	5.1	4.4	4.5	4.8	3.1	3.1	2.3
	20	6.5	6.5	1.0	4.8	4.8	0.8	2.9	2.9	1.1
	25	6.4	6.5	6.8	4.0	4.1	7.3	2.3	2.3	3.2
15	10	6.3	6.3	2.5	5.0	5.1	3.0	3.8	3.8	3.0
	15	14.2	14.4	2.4	9.6	9.7	2.9	4.5	4.4	3.9
	20	9.2	9.3	1.0	6.9	6.9	1.2	4.3	4.3	2.1
	25	9.0	9.1	0.8	6.0	5.9	1.3	3.2	3.1	3.6
20	10	8.0	8.0	0.9	6.4	6.4	0.7	4.9	4.9	1.4
	15	10.1	10.1	1.0	8.0	8.0	1.6	5.7	5.7	1.5
	20	11.1	11.4	5.6	8.2	8.5	4.7	5.1	5.2	5.6
	25	11.8	11.9	6.5	7.8	7.9	6.5	3.8	3.7	6.8
25	10	9.7	9.7	2.6	7.8	7.8	1.9	5.9	5.9	1.3
	15	12.0	12.0	1.8	9.5	9.5	1.6	6.8	6.8	0.9
	20	13.6	13.9	2.8	10.2	10.4	3.1	6.5	6.6	3.0
	25	14.3	14.5	2.1	9.6	9.7	2.6	4.5	4.4	3.3

Note: AL: Active Length, NH: Non-Homogeneous Normal tissue, HN: Homogeneous Normal tissue, (%D): maximum percentage deviation between the homogeneous and the non-homogeneous cases.

Table 3.9. Volumes (mm^3) of tissue subjected to undertreatment because of the presence of blood vessels. Considering in the model the electrical conductivity of healthy (normal) liver.

AL (mm)	Space (mm)	3000 V			2500 V			2000 V		
		Min	Max	Mean	Min	Max	Mean	Min	Max	Mean
10	10	0.0	53.3	34.5	0.0	55.1	35.1	0.0	48.7	30.1
	15	0.0	119.1	58.6	0.0	82.4	40.6	0.0	33.1	19.2
	20	4.4	10.1	7.9	1.6	5.9	4.4	0.0	4.9	3.2
	25	3.0	12.2	7.8	0.0	8.2	3.7	0.0	6.5	3.3
15	10	0.0	28.6	13.8	0.0	17.3	8.5	0.0	13.2	6.3
	15	114.6	160.6	145.2	93.8	109.1	103.2	14.6	41.8	30.4
	20	15.6	54.7	37.0	6.1	53.1	31.7	0.0	48.3	21.5
	25	4.2	45.4	20.4	2.0	24.8	10.8	0.0	8.2	3.1
20	10	2.0	76.2	32.7	1.3	52.9	27.0	0.0	37.5	20.4
	15	0.0	109.4	51.8	0.0	62.1	34.6	0.0	53.4	28.4
	20	120.1	443.7	216.7	90.2	370.0	171.8	41.2	193.2	113.4
	25	49.9	291.6	172.1	35.1	224.4	142.3	0.0	88.0	39.8
25	10	31.1	63.9	48.1	16.6	54.2	37.6	9.2	41.8	27.8
	15	9.5	121.5	55.4	4.1	76.5	34.7	1.5	41.7	18.1
	20	114.8	402.0	212.6	97.9	344.6	176.9	57.2	200.6	103.2
	25	74.5	197.9	143.6	60.8	161.9	99.9	19.5	52.0	32.4

Note: Min: Minimum, Max: Maximum.

Table 3.10. Volumes of tumor tissue subjected to undertreatment because of the presence of blood vessels of different IRE thresholds (V/cm).

Active length (mm)	Space (mm)	500 V/cm	600 V/cm	700 V/cm	800 V/cm	1000 V/cm
20	15	95.7	63.1	44.2	35.2	15.2
	20	319	272.3	224.8	180	49.2
	25	317.9	202.9	159.4	75.5	19.6
25	15	190.7	142.1	119.5	87.8	41.1
	20	273	271.2	227.7	206.3	98.4
	25	241.5	204.2	182.6	153.7	119.8

Note: 3000 V applied potential

Table 3.11. A number of cases of undertreatment (undertreated volume $\geq 1 mm^3$) out of the 6 assayed insertion locations. Considering in the model the electrical conductivity of healthy (normal) liver.

Electric Potential(V)	Active length (mm)	Space(mm)			
		10	**15**	**20**	**25**
2000	**10**	2/6	2/6	2/6	3/6
	15	2/6	2/6	3/6	3/6
	20	3/6	4/6	4/6	4/6
	25	3/6	4/6	4/6	5/6
2500	**10**	2/6	2/6	3/6	3/6
	15	2/6	3/6	4/6	4/6
	20	4/6	5/6	6/6	6/6
	25	5/6	5/6	6/6	6/6
3000	**10**	3/6	4/6	4/6	4/6
	15	3/6	4/6	5/6	6/6
	20	4/6	5/6	5/6	6/6
	25	5/6	5/6	6/6	6/6

Table 3.12. Average undertreated volume (mm^3) for different electrical conductivities of the liver vessels. Considering of healthy (normal) liver.

Active length (mm)	Space (mm)	3000V		2500V		2000V	
		0.7 (S/m)	**0.1 (S/m)**	**0.7 (S/m)**	**0.1 (S/m)**	**0.7 (S/m)**	**0.1 (S/m)**
10	**10**	34.5	0.0	35.1	0	30.1	0
	15	58.6	0	40.6	0	19.2	0
	20	7.9	0	4.4	0	3.2	0
	25	7.8	6.5	3.7	3.9	3.3	3.2
15	**10**	13.8	0	8.5	0	6.3	0
	15	145.2	1.1	103.2	1.4	30.4	1.2
	20	37.0	1.2	31.7	0	21.5	3.6
	25	20.4	2.7	10.8	0	3.1	0
20	**10**	32.7	0	27.0	0	20.4	0
	15	51.8	0	34.6	0	28.4	0
	20	216.7	3.3	171.8	1.5	113.4	1.2
	25	172.1	7.9	142.3	17.7	39.8	3.1
25	**10**	48.1	2	37.6	1	27.8	0.7
	15	55.4	7.3	34.7	4.9	18.1	1.4
	20	212.6	11	176.9	6	103.2	2
	25	143.6	3.2	99.9	2.8	32.4	1.5

Table 3.13. A number of cases of undertreated volume ≥1mm^3 out of the 6 assayed insertion locations When the conductivity of the vessels is 0.1 S/m. normal tissue.

Potential(V)	Active length(mm)	Space(mm)			
		10	**15**	**20**	**25**
2000	**10**	0/6	0/6	0/6	2/6
	15	0/6	1/6	2/6	0/6
	20	0/6	0/6	2/6	2/6
	25	1/6	2/6	2/6	2/6
2500	**10**	0/6	0/6	0/6	2/6
	15	0/6	2/6	0/6	0/6
	20	0/6	0/6	1/6	3/6
	25	1/6	3/6	3/6	1/6
3000	**10**	0/6	0/6	0/6	2/6
	15	0/6	2/6	2/6	3/6
	20	0/6	0/6	0/6	2/6
	25	0/6	1/6	2/6	0/6

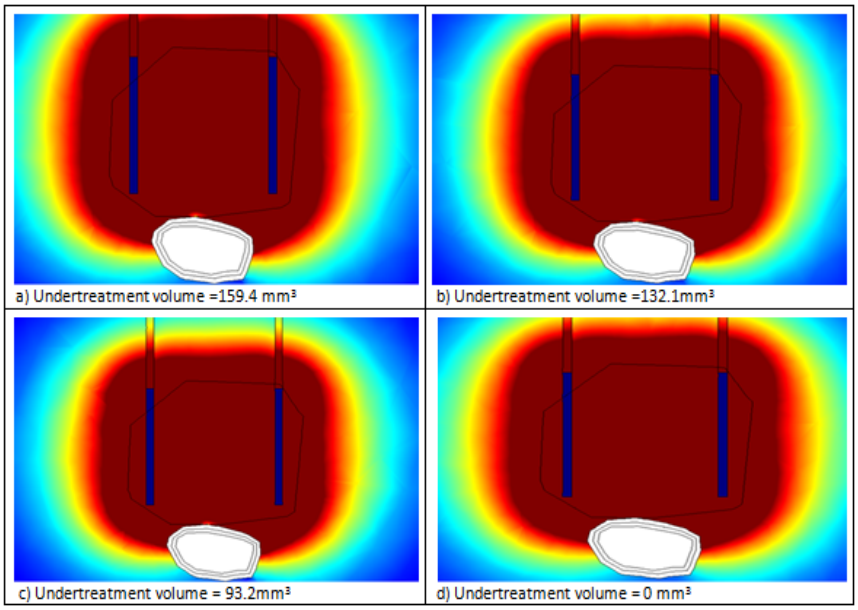

Figure 3.5. X-Y plane plot of electric field magnitude during hypothetical treatment of a tumor. (a) The non-homogeneous model ($\sigma_{vessels}$ = 0.7 S/m = $\sigma_{wall} \neq \sigma_{liver} \neq \sigma_{tumor}$) result. (d) The non-homogeneous model ($\sigma_{vessels}$ = 0.7 S/m $\neq \sigma_{wall} \neq \sigma_{liver} \neq \sigma_{tumor}$) result (c) The non-homogeneous model ($\sigma_{vessels}$ = 0.7 S/m $\neq \sigma_{wall} \neq \sigma_{liver} \neq \sigma_{tumor}$) result 3-electrode array (d) Result when the vessel is filled with a low conductivity fluid ($\sigma_{vessels}$ = 0.1 S/m $\neq \sigma_{liver} \neq \sigma_{tumor}$) .

CHAPTER 4

Fast Semi-Analytical Approach for Field Computation in Electroporation Treatment Planning

Abstract

Electroporation based therapies are becoming an increasingly attractive option for minimally invasive treatment of tumors. Electroporation treatment effectiveness mainly depends on electric field distribution. Typically numerical methods are used for modeling the electric field distribution, which is highly computational demanding and time-consuming. In this chapter it is presented a fast semi-analytical algorithm to calculate the electric field distribution when needle-shaped electrodes are employed for treatment delivery. The solution presented here makes the use of approximating needle electrodes needle electrodes as strings of charged spheres in a electrostatics problem. The algorithm calculates the position, number of spheres, electric potential and electric charges of the spheres, and then calculates the electric field at any point in the space by superposition. A systematic study of 20 cases with various possible configurations for pair of needles (Parallel, non-Parallel or asymmetric) was conducted for validation purpose. The semi-analytical algorithm results were compared with results from simulations computed with the finite element method (FEM). In particular the algorithm results were compared to simulations in which the medium conductivity was modeled as constant and to simulations in which it was modeled the dependence of tissue conductivity on the electric field due to the electroproation phenomenon (dynamic conductivity). The total current percentage deviation, the surface Euclidean distance and the maximum average distance of the ablation zone were estimated. The results showed a very good correlation between the algorithm and the FEM simulation under the assumption of constant conductivity. The comparison with homogenous-static and homogeneous -dynamic models indicated a maximum average distance of 5.6 and 9.8 mm respectively. However, the semi-analytical prototype was able to represent the solution with 1s, while the average estimated running time of numerical static and dynamic models were 42.8s and 243.1s respectively. Despite the limitations of the semi-analytical solution to the constant conductivity, it will be very useful in providing physicians with fast feedback on electric field distribution especially when they aim to optimize the treatment planning.

The content of this chapter is adapted from the following article (in preparation for publication):

R. Qasrawi, B. Mercadal , Q. Castellvi, Z. Abdeen, and A. Ivorra, " Fast Semi-Analytical Algorithm for Computing the Electric Field Distribution in Electroporation Treatment Planning. (In Preparation for Submission)

4.1 Introduction

Image-guided tumor ablation therapies using the electroporation technique have been developed as a minimally invasive treatment for cancer treatment due to its high effectiveness, minimal side effects and low cost[55], [141]–[144]. Electroporation treatment has become a widely used technique in the clinical routine for cutaneous, subcutaneous and recently for deep-seated tumors with response rates of approximately 70-100%[68], [142], [145], [146]. The treatment is entering routine clinical practice in the USA and many Europe countries. Currently, the technology is used for skin, liver, kidney, prostate, pancreatic, colorectal and renal tumors [101], [108], [147]–[149].

Treatment planning is used to determine treatment region size and shape. It involves managing and controlling the electroporation parameters, such as electrode geometry (active length, diameters, and orientations) as well as electrode placement for specifically applied potentials[94], [150]. There are two types of electroporation treatment, namely: electrochemotherapy that is used for allowing cytotoxic drugs to enter the cell[151][152]. And the non-thermal irreversible electroporation (N-IRE) that is used for ablating deep-seated tumors[5].

The success of electroporation therapy depends on the appropriate settings of treatment parameters and on the placement of electrodes into the target lesion to achieve complete tumor coverage with adequate electric field distribution[94]. In fact, Electroporation-based treatment has been identified and developed for many clinical applications, such as ECT and IRE. Despite standard operating procedures to ensure safe and successful treatment for the targeted tumors have been set[153][134], [21], nevertheless, patient-specific treatment planning is required prior deep-seated tumor treatment application [96], [99], [122].

Usually, deep-seated tumors have diverse shapes, size, and location. This entails exposing the target tissues with sufficient electric field that requires long needle electrodes and a proper electric field distribution. This can only be achieved by means of numerical or analytical modeling of electric field distribution based on real data from the patient medical image and proper electrode insertions.

Electroporation treatment planning tools have been used for this purpose [96], [99], [122] with inherent drawbacks. For example, numerical modeling has been used in many studies for different electroporation treatment purposes based on commercial packages developed for more general physics/electromagnetic simulations, such as COMSOL (www.comsol.com). Recently, Mehedi et al. introduced a simple analytical model for calculating electric fields in tissues based on the fractional-order model. The preliminary results of this study indicated that the calculated electric field distribution might help to find the optimal electrode configurations in electroporation treatment planning[155].

Furthermore, a web-based electroporation treatment planning software has been developed by the University of Ljubljana[99]. The software includes image processing algorithms for automatic tissue segmentations, surface reconstruction algorithms for generating the 3D model of the tissue, procedures for electrode insertions, while the electric field distribution is computed based on the Matlab–Comsol integration for numerical modeling. Unfortunately, the COMSOL numerical modeling requires a 3D simplified volume geometry, in order to save the computational time and resources. The software managed to minimize the process of 3D geometry reconstruction of the liver treatment plan by using the automatic segmentation algorithm for a liver from CT images. Also, it includes an efficient interactive tool for electrode insertion. However, the geometry simplification (meshing, cleaning, curvature, optimization, and decimation) still needed for numerical modeling. Furthermore, the post-processing of the computed electric fields and currents is handled by Matlab using built-in COMSOL functions.
In this study, we developed a fast semi-analytical algorithm for estimating the electric field distribution with accuracy that resembles numerical modeling. The algorithm designed to facilitate the real-time clinical application by providing physicians with very fast feedback on the electric field distribution when they are trying different electrode positions and orientations. Furthermore, it can provide a preliminary approximation for electric field distribution before performing the accurate simulation.

4.2 Methods

The fast semi-analytical algorithm has been developed as a voxel-based prototype software in C++ programming language and integrated to GIMIAS software package[114]. The key ideas of the algorithm were first conceived by Quim Castellví and Antoni Ivorra. Borja Mercadal devised the set of equations implemented in the algorithm and performed the first trials in Matlab. Radwan Qasrawi implemented prototype, the integration into GIMIAS and the validation presented here.The following sections describe the electrode geometry creations and the fast semi-analytical algorithm for electric field distribution calculation.

4.2.1 The semi-analytical algorithm

The semi-analytical algorithm applies the superposition principle in approximating the electrodes geometry from a set of conductive spheres and analytically calculates the electric field distribution generated from each sphere, while the overall electric field magnitude equals the sum of the spheres individual contributions.

In preliminary tests, it was found that the most accurate results were achieved upon assuming spheres separated by a distance equal to its radius as shown in the figure 4.1.:

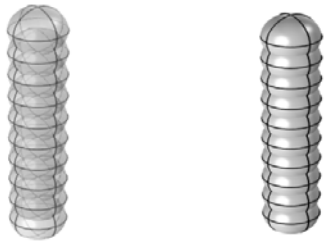

Figure 4.1. The approximated 3D electrodes geometry from a chain of conductive spheres.

The radius is calculated by imposing two conditions: that the contact surface of the medium is the same as the needles we are modeling, and the total length occupied by the spheres is the same as the needles. This means that to calculate the radius of our spheres, first we have to take into account that the sphere at the top, as well as the sphere at the bottom, has a higher contribution to the total surface than the other spheres. Then the surface would be:

$$S = 2 \times 3\pi R^2 + (n-2) \times 2\pi R^2 \quad (1)$$

R is the radius of the spheres and n the total number of spheres. The second condition leads to the following equation:

$$(n+1)R = h \quad (2)$$

h is the length of the needle. The system of equations 1 and 2 which is assumed to be equal to the surface of the needle (approximated as a cylinder), allows calculation of the sphere's radius as well as a number of spheres which in turn will lead to the calculation of the sphere centers.
After defining the spherical electrode geometry, the algorithm computes the electric field distribution assuming that the spheres act as point current sources. For obtaining the expressions that provide the electric field induced by these current sources, it was employed the duality between the current in volume conductors and the charge in electrostatics [156]. That is, it was solved an electrostatic problem equivalent to the current conduction problem.

The voltage difference between the two needles is U which means that we have a number of spheres n1 at a potential V=U/2 (first needle) and a number of spheres n2 at a potential V=-U/2 (second needle). This represents the system of conductors, which under electrostatic equilibrium the electric field inside them will be zero and its electric potential will be constant. The electric potential generated by a conducting sphere in the outer regions is assumed to be the same as that generated by a punctual charge:

$$V(r) = \frac{Q}{4\pi\varepsilon r} \tag{3}$$

Q is the charge of the sphere and r the distance from the point at which we are calculating the potential and the center of the sphere.
The potential of one sphere will be the sum of the potential generated by its own charge and the potentials generated by the rest of the charges in our geometry:

$$V_i = \frac{Q_i}{4\pi\varepsilon R_i} + \frac{Q_1}{4\pi\varepsilon d_{i,1}} + \frac{Q_2}{4\pi\varepsilon d_{i,2}} + \cdots + \frac{Q_N}{4\pi\varepsilon d_{i,N}} \tag{4}$$

Where $d_{i,j}$ is the distance between the surface of sphere i and the center of the sphere j and N is the total number of spheres (N=n1+n2). Equation 4 is the same as:

$$V_i = \sum_{j=1}^{j=N} b_{ij} Q_j \tag{5}$$

With b_{ij} defined as:

$$b_{ij=} \begin{cases} b_{ii} = \dfrac{1}{4\pi\varepsilon}\dfrac{1}{R_i} \\ b_{ij} = \dfrac{1}{4\pi\varepsilon}\dfrac{1}{d_{ij}} \end{cases} \tag{6}$$

If both needles have equal radii, b_{ij} will be a symmetric matrix. Since we know that the potential of the spheres has to be:

$$V_i = \begin{cases} +\dfrac{U}{2} & i = 1, \dots, n_1 \\ -\dfrac{U}{2} & i = n_1 + 1, \dots, n_1 \end{cases} \tag{7}$$

Then we calculate the charges by solving the linear system:

$$Q_i = a_{ij} V_j \tag{8}$$

Where a_{ij} is the inverse matrix of b_{ij}.

These charges can be associated to the current injected by each needle. This current will be proportional to the sum of the charges of the spheres:

$$I_{needle} = \frac{\sigma}{\varepsilon} \sum_{needle} Q_i \tag{9}$$

Where σ is the conductivity of the medium. This approximation does not take into account that the current on the two needles has to be the same but with opposite sign. To correct this, we add the condition that the sum of the two currents has to be lower than a certain value or tolerance. This leads to two additional equations to add to our linear system for the calculation of the charges:

$$\begin{cases} \frac{\sigma}{\varepsilon} \sum_{i=1}^{N} Q_i \leq \delta \\ \frac{\sigma}{\varepsilon} \sum_{i=1}^{N} Q_i \geq -\delta \end{cases} \tag{10}$$

Where δ is the tolerance. We have not studied the optimal value of the tolerance. We imposed a tolerance of 1 mA arbitrarily because we will work generally with currents in the order of amperes.
Finally, with this additional condition, to find the values of the charges we need to solve by the least squares method the linear system composed by equations 8 and 10:

$$\begin{cases} Q_i = a_{ij} V_j \\ \frac{\sigma}{\varepsilon} \sum_{i=1}^{N} Q_i \leq \delta \\ \frac{\sigma}{\varepsilon} \sum_{i=1}^{N} Q_i \geq -\delta \end{cases} \tag{11}$$

From the spheres positions and its charges, we can calculate the electric field at any point in the space by superposition. The electric field at an arbitrary point will be the sum of the field generated by each sphere:

$$\vec{E}_i(\vec{r}) = \frac{Q_i}{4\pi\varepsilon} \cdot \frac{(\vec{r} - \vec{r_i})}{|\vec{r} - \vec{r_i}|^3} \tag{12}$$

$$\left|\vec{E}\right| = \left| \sum_{i=1}^{N} \vec{E}_i \right| \tag{13}$$

Where r is the position at which we are calculating the field and r_i is the center of the sphere i.

In our model, we assumed the points in the space to represent the points of the target geometry that have been extracted from the patient medical image. The software reconstructs a voxel-based geometry with a scalar value equal to the electric field distribution at each point in the target region. Then the tool provides users with an isosurface reconstruction plug-in based on electric field threshold value by means of vtkMarchinCube and vtkContourFilter that is built in our planning tool.

4.2.2. Number of points optimization

The time elapsed by the algorithm depends on the geometry of the needles which is related to the number of spheres (the ratio length/radius of the needle conditions the number of spheres). However, on average, all the calculations before the computation of the electric field do not exceed 0.35 seconds and computing the electric field at a single point takes about 31μs. If we divide our simulation space with a grid of NxNxN points then the time cost is proportional to N^3. To obtain the results in less than 1 second the maximum N we can use is between 25 and 30. If our simulation space is large, this grid would lead to results that are not highly accurate. Therefore, we first need to reduce the space for electric field calculation by narrowing the region in which we expect a field higher than the iso-surface value.

To choose the minimum and maximum values of x, y, and z, we approximate the needles as a single charge (with a charge equal to the total charge of the needle) located in the middle of the needle. We then calculate the distance at which the electric field generated by these charges will be significantly lower than our iso-value. Using this distance, we set the limits of our region keeping in mind that the length of the grid has to be equal in all directions x, y, and z.

4.2.3. Algorithm validation

We have performed wide-ranging validation studies for testing the semi-analytical algorithm. The accuracy of our semi-analytical solution has been validated by comparing it with the numerical simulation results based on COMSOL. The implementation of electrodes has been validated by comparing the values of electric current generated by different electrode configurations, as well as by graphically comparing the Iso-Surfaces numerically obtained at IRE electric field threshold (E=800V/cm). Furthermore, we compared the distances between the numerically estimated Isosurfaces at E=800V/cm with the Isosurfaces estimated by the semi-analytical solution.

In order to graphically illustrate the correlation between the algorithm results and the numerical solution, we modeled IRE treatment in six models in various possible clinical applications. The 3D iso-surface and

the 2D plan plots were compared, in addition to the estimation of the Euclidian distance in the X, Y, and Z-Directions.
The accuracy of our semi-analytical algorithm results was compared with the results of numerical homogeneous static and homogeneous dynamic conductivity models in a series of 20 cases with different configurations. The numerical homogeneous static conductivity was set to the conductivity of the hepatic tumor tissue (0.5S/m) as described in Prakash et al.[119]. As for the homogeneous dynamic conductivity in the hepatic tumor tissue, it was modeled with the sigmoid function as described in[120]. In all cases, the total electric current, the maximum average distance and the estimated running time were reported and compared.
In order to illustrate the effectiveness of the fast algorithm in clinical application, a patient-specific treatment plan with a liver tumor of $2.8cm^3$ was conducted in an anatomically realistic case study[79]. We performed the simulation in three models (constant-analytical, homogenous-static and homogeneous-dynamic) in which the tumor, liver, bones and surrounding tissues were given initial conductivity values (0.2, 0.05, 0.02 and 0.2 S/m) respectively. The homogeneous dynamic conductivity changes were modeled with the sigmoid function described in [120]. The electrodes modeled in this case study were 2 needle electrodes with $1e^{-3}$ mm diameter; 20mm interelectrode space and 20mm electrode active length and 3000V applied potential. We performed our simulation on CT data sets stored as DICOM images, 512 by 512 pixels with a 12-bit gray level resolution, 5mm interval and with 67 slides. The computer used for runtime measures had Intel(R) Core(TM) i7-4770, 3.4GHz CPU, 8GB RAM and Windows 7 Professional operating system.
The study included the performance of a complete treatment planning procedure similar to radiotherapy treatment planning. In this case study, the difference in electric current, maximum average distance and the estimated running time were compared.

4.3 Results

Results from simulations performed using the fast analytical algorithm are compared here with results generated by the numerical simulation based on the commercial finite element package solver (Comsol Multiphysics, AS, Stockholm, Sweden). To evaluate our analytical module, we compared its behavior on a uniform 3D cuboid domain with two needles electrodes. Furthermore, we evaluated the model according to an anatomically realistic liver model reconstructed from human CT image.

4.3.1 Comparison of electric field distribution

Electrode configuration is one of the potential variables that affect the electric field distribution and the electroporation treatment effectiveness.

It has been shown that the electrode parameters (i.e. the length of exposure and interelectrode spacing) and the applied potential (i.e. voltage and current) have major effects on treatment outcomes [94], [150]. Therefore, in order to estimate the accuracy in our semi-analytical approximation method, we compared the semi-analytical results with the same models from the numerical simulation in various possible clinical situations as shown in Table 4.1. The six models were performed on a uniform cuboid domain under the assumption of constant tissue conductivity(1S/m). The configurations examined a set of variables including electric potential, the length of exposure, interelectrode spacing, electrode thickness, and electrode orientation (θ and φ). Each simulation examined one or more variables. The results were compared for IRE treatment zones where electric field threshold set as E_{th}=800V/cm.

Table 4.1. The electrode configurations used in the constant conductivity analytical and numerical simulations

Model number	Electrode one				Electrode Two					Spacing
	R1(m)	L 1(m)	θ_1	φ_1	R2(m)	L2 (m)	θ_2	φ_2	(KV)	(m)
1	2.5e-4	0.02	0	0	2.5e-4	0.02	0	0	7	0.02
2	2.5e-4	0.02	-30	-90	2.5e-4	0.02	-45	-90	8	0.02
3	2.5e-4	0.02	30	-90	2.5e-4	0.02	30	-90	10	0.02
4	2.5e-4	0.03	-60	-75	2.5e-4	0.05	45	-15	12	0.02
5	2.5e-4	0.02	35	-35	2.5e-4	0.02	-25	-75	8	0.02
6	2.5e-4	0.04	-60	-90	2.5e-4	0.01	-45	120	12	0.02

Note: R:electrode radius, L: electrode active length; V:electric potential; θ: polar angle (theta); φ: azimuthal angle (phi) in spherical coordinate.

In Figure 4.2. (a-f), 3D snapshots from the six cases illustrated in Table 4.1. are presented. For each case, a 3D Isosurface of IRE (E_{th}=800V/cm) plot was obtained from the semi-analytical and numerical models. The ellipsoidal ablation zones of the electric field distribution were compared for both simulations. The results of electric field distribution plots in Figure 4.2. indicated a uniform distribution and a very good agreement between the solution obtained from the semi-analytical algorithm and the numerical simulation. However, a small deviation was noticed at the periphery of the Isosurface of the electric field distribution.

The resulting ablation zones are compared using the Average Maximum Distance between the overall points. In our calculation, we considered only the points on the surface of the electric field distribution and deleted

the intersection points from our calculation since we assumed the distances to be zero.

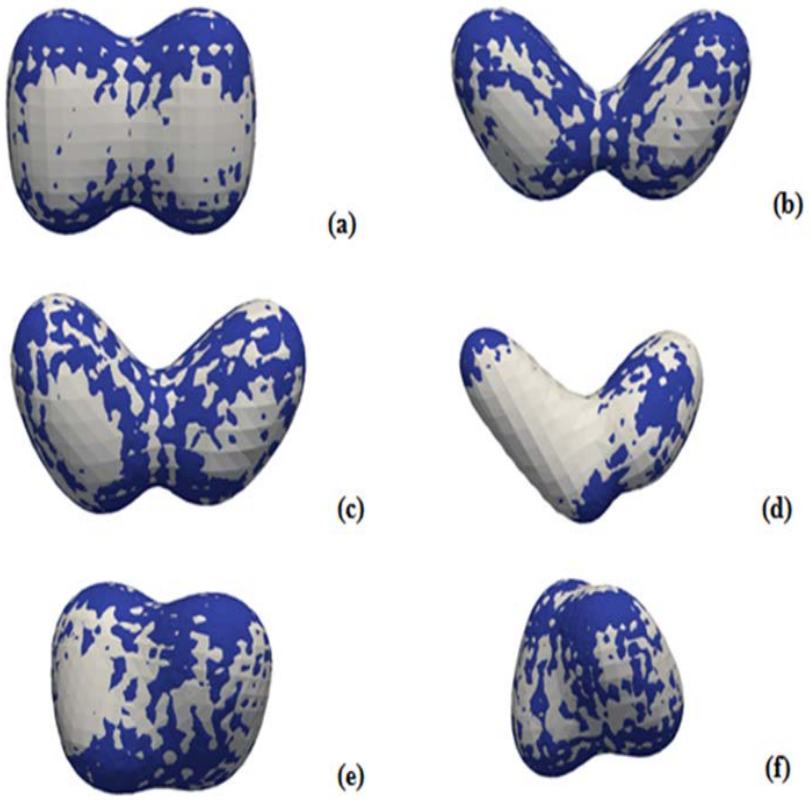

Figure 4.2. IRE 3D Iso-Surface plot (E_{th}=800V/cm) of the analytical (blue color) and numerical (gray color) simulations. Figures (a-f) represent the results of the constant conductivity models shown in Table 4.1. respectively.

Table 4.2. The average maximum distance between the semi-analytical and numerical simulations results.

Model	(X-AMD) (mm)	Max(Y-AMD) (mm)	Max(Z-AMD) (mm)	Max(AMD) (mm)
1	1.9	0.3	0.2	1.9
2	3.2	0.3	0.4	3.2
3	2.8	0.2	0.3	2.8
4	4.9	1.2	0.3	5.1
5	1.9	0.1	0.1	1.9
6	2.0	0.1	1.1	2.3

Note: AMD is the Average Maximum Difference; X, Y, Z is the XYZ directions

Table 4.2. shows the comparison of the average maximum distances between the semi-analytical and numerical simulated models. The results indicated that the maximum average distance found was 5.1mm in model 4. The results indicate a good correlation with numerical simulation considering the speed of geometry preparation and the electric field calculation time (especially in complex geometries).
Furthermore, the result depicted in Table 4.2. shows that the largest difference was introduced by incorporating various electrode lengths (model 4 and 6), where the largest maximum average distance found were 4.9, 1.2 and 1.1mm along the X, Y and Z-directions respectively.

4.3.1 Surface distance contours of electric field distribution

In order to quantify the accuracy of our analytical method, we compared it with the numerical method by estimating the Euclidean surface distances of the models described in Table 4.1. at different locations in the X-Y and Z-Y planes. For that, 2D cross-section plots and surface distance differences were illustrated in the following paragraphs:

Model 1. In Figure 4.3., the two methods were compared in the 2D X-Y and Z-Y plane plot. Figure 4.3.(a) shows the 2D X-Y plane plot at Z=-0.15, -0.14 and -0.13. The Z-direction surface distance at the 3 points is 0.2, 0.4 and 1.3 mm respectively. Figure 4.3.(b) shows the 2D Z-Y plane plot at X= 0.15, 0.145, and 0.14. The X- direction surface distance at the 3 points is 0.2, 0.1 and 1.1 mm respectively. The results indicated a very good correlation with the numerical model and a uniform ellipsoid electric field distribution is clearly evident.

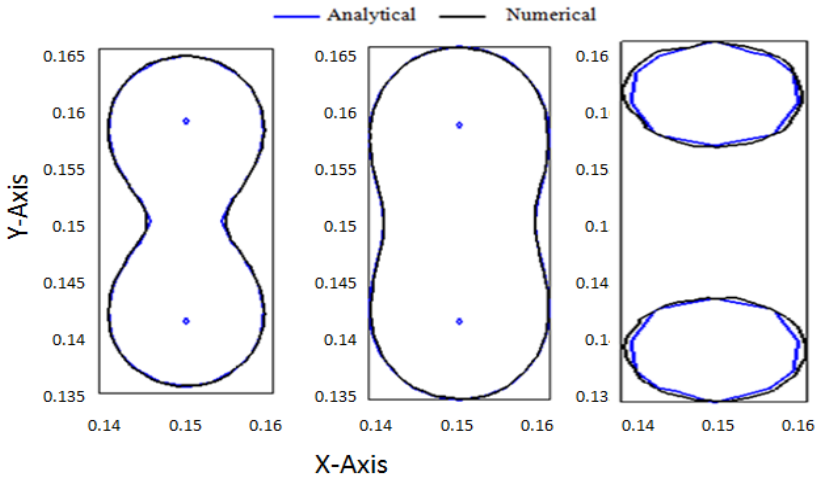

Figure 4.3. (a) The X-Y plane plot of electric field magnitude (E_{th}=800V/cm) for analytical and numerical solutions at Z= -0.15, -0.14 and -0.13 from left to right respectively.

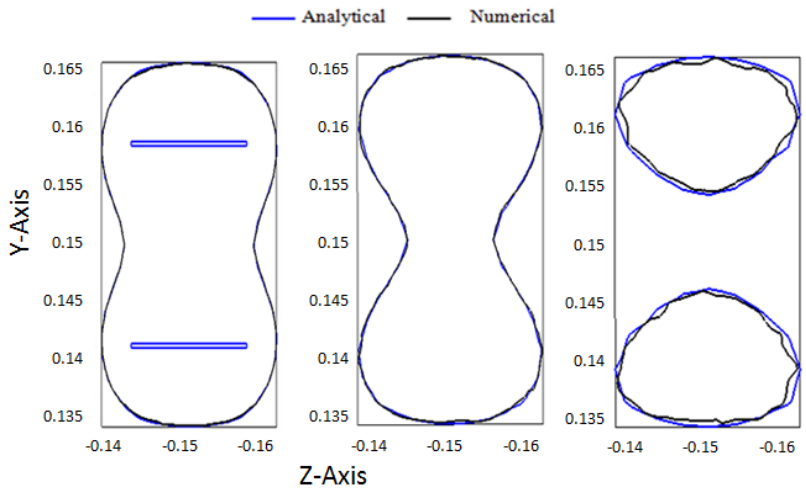

Figure 4.3. (b) The Z-Y plane plot of electric field magnitude (Eth=800V/cm) for analytical and numerical solutions at X=0.15, 0.145 and 0.14 from left to right respectively.

Model 2. In Figure 4.4., the two methods were compared in the 2D X-Y and Z-Y plane plot. Figure 4.4.(a) shows the 2D X-Y plane plot at Z= -0.155, -0.15 and -0.14. The Z-direction surface distance at the 3 points is 0.4, 0.6 and 0.8 mm respectively. Figure 4.4.(b) shows the 2D Z-Y plane plot at X=0.15, 0.155 and 0.157. The X-direction surface distance at the 3

points is 0.4, 0.5 and 0.7 mm respectively. The results indicated a very good correlation with the numerical model and a uniform ellipsoid electric field distribution is noticed.

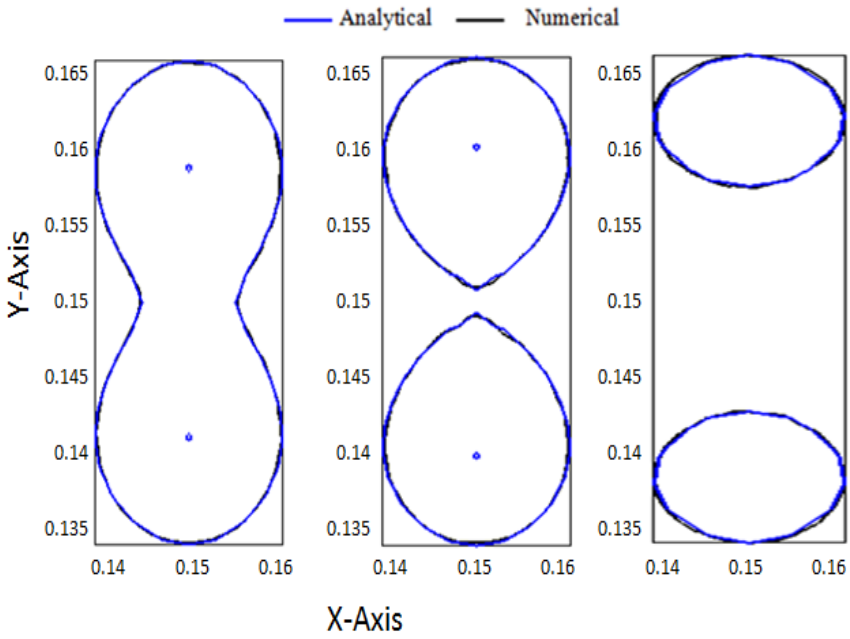

Figure 4.4. (a). The X-Y plane plot of electric field magnitude (E_{th}=800V/cm) for analytical and numerical solutions at Z= -0.155, -0.15 and -0.14 from left to right respectively.

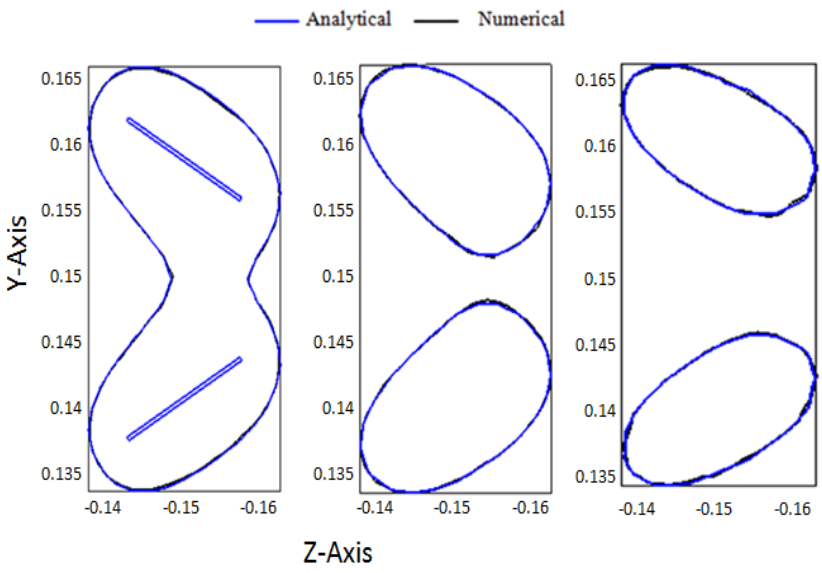

Figure 4.4. (b) Z-Y plane plot of electric field magnitude (Eth=800V/cm) for analytical and numerical solutions at X= 0.15, 0.155 and 0.157.

Model 3. In Figure 4.5., the two methods were compared in the 2D X-Y and Z-Y plane plot. Figure 4.5.(a) shows the 2D X-Y plane plot at Z=-0.16, -0.15 and -0.14. The Z-direction surface distance at the 3 points is 0.2, 0.3 and 0.3 mm respectively. Figure 4.5.(b) shows the 2D Z-Y plane plot at X=0.15, 0.155 and 0.16. The X-direction surface distance at the 3 points is 0.2, 0.3 and 0.6 mm respectively. The results indicated a very good correlation with the numerical model and a uniform ellipsoid electric field distribution is noticed.

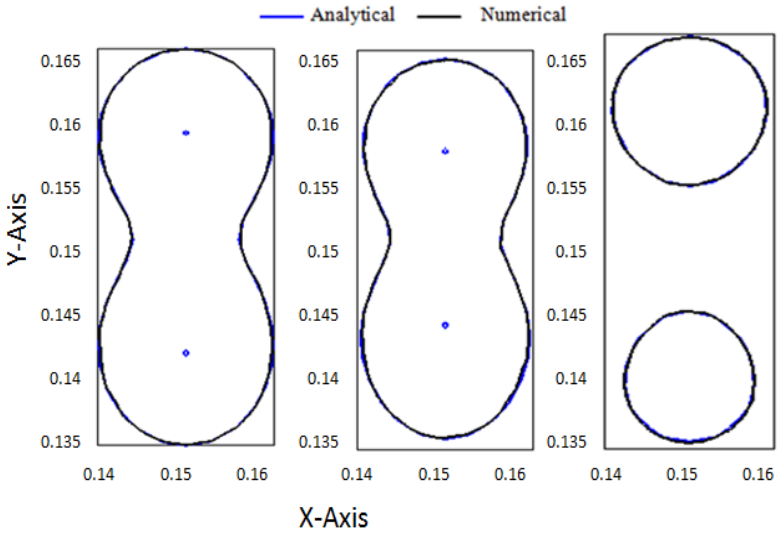

Figure 4.5.(a). The X-Y plane plot of electric field magnitude (E_{th}=800V/cm) for analytical and numerical solutions at Z= -0.16, -0.15 and -0.14 from left to right respectively.

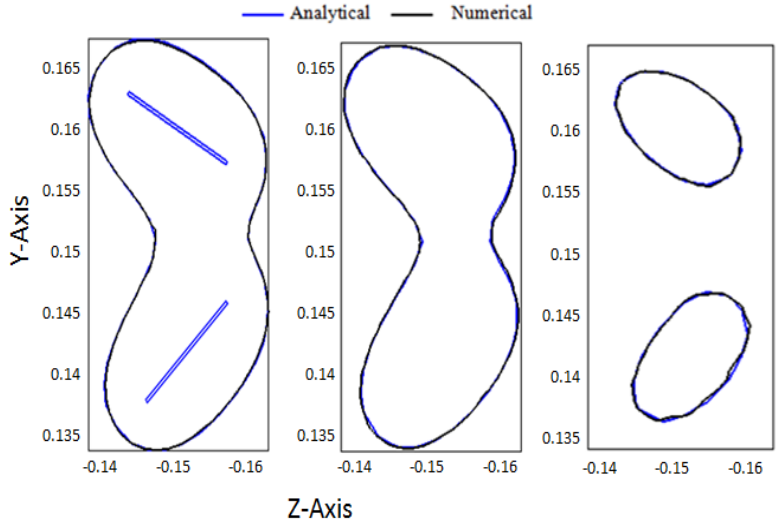

Figure 4.5. (b). Z-Y plane plot of electric field magnitude (E_{th}=800V/cm) for analytical and numerical solutions at X= 0.15, 0.155 and 0.16 from left to right respectively.

Model 4. In Figure 4.6., the two methods were compared in the 2D X-Y and Z-Y plane plot. Figure 4.6.(a) shows the 2D X-Y plane plot at Z=0.15, -0.16 and -0.14. The Z-direction surface distance at the 3 points is 0.9, 1.1 and 1 mm respectively. Figure 4.6.(b) shows the 2D Z-Y plane plot at X= 0.16, 0.15 and 0.14. The X-direction surface distance at the 3 points is 0.8, 1.3 and 1.1 mm respectively. The results indicated a very good correlation with the numerical model and a uniform ellipsoid electric field distribution is noticed.

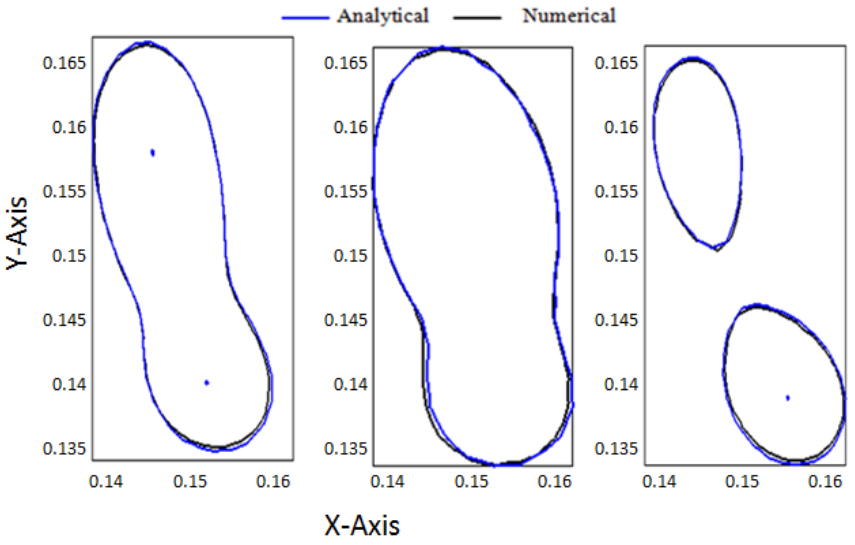

Figure 4.6.(a). The X-Y plane plot of electric field magnitude (E_{th}=800V/cm) for analytical and numerical solutions at Z= -0.15, -0.16 and -0.14 from left to right respectively.

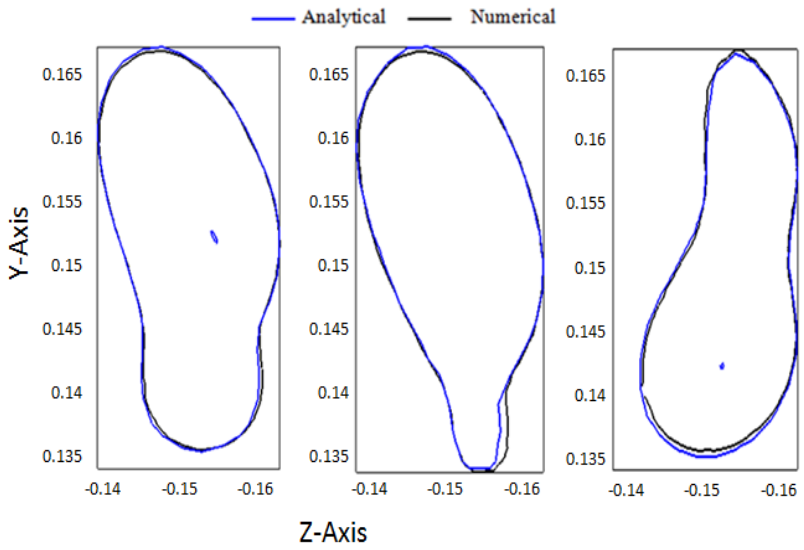

Figure 4.6. (b). Z-Y plane plot of electric field magnitude (E_{th}=800V/cm) for analytical and numerical solutions at X= 0.16, 0.15 and 0.14 from left to right respectively.

Model 5. In Figure 4.7., the two methods were compared in the 2D X-Y and Z-Y plane plot. Figure 4.7.(a) shows the 2D X-Y plane plot at Z= -0.15,-0.16 and -0.165. The Z-direction surface distance at the 3 points is 0.1, 0.3 and 0.5 mm respectively. Figure 4.7.(b) shows the 2D Z-Y plane plot at X= 0.15, 0.16 and 0.165. The X-direction surface distance at the 3 points is 0.1, 0.2 and 0.6 mm respectively. The results indicated a very good correlation with the numerical model and a uniform ellipsoid electric field distribution is noticed.

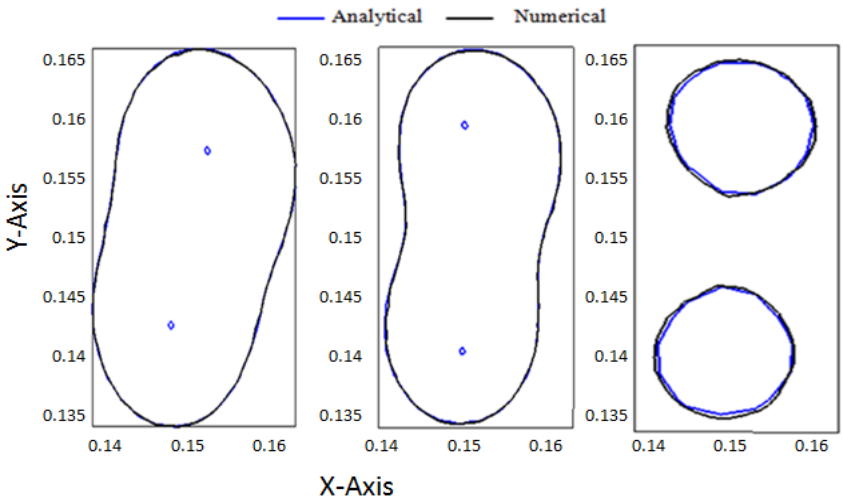

Figure 4.7. (a). The X-Y plane plot of electric field magnitude (E_{th}=800V/cm) for analytical and numerical solutions at Z= -0.15, -0.16 and -0.165 from left to right respectively.

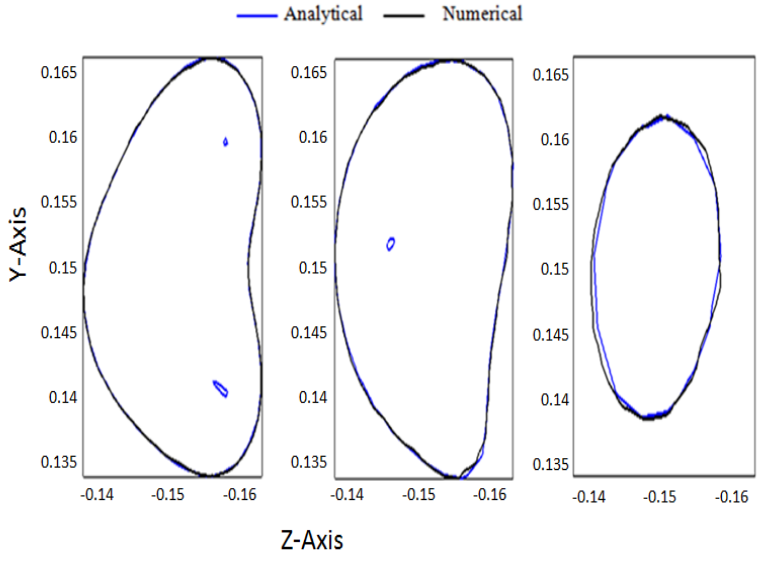

Figure 4.7. (b). The Z-Y plane plot of electric field magnitude (E_{th}=800V/cm) for analytical and numerical solutions at X= 0.15, 0.16 and 0.165 from left to right respectively.

Model 6. In Figure 4.8., the two methods were compared in the 2D X-Y and Z-Y plane plot. Figure 4.8.(a) shows the 2D X-Y plane plot at Z= -0.15, -0.145 and -0.14. The Z-direction surface distance at the 3 points is 3.6, 3.9 and 3.1 mm respectively. Figure 4.8.(b) shows the 2D Z-Y plane plot at X=0.145, 0.15 and 0.155. The X-direction surface distance at the 3 points is 2.4, 2.3 and 2.6 mm respectively. The results indicated a good correlation with the numerical model and a uniform ellipsoid electric field distribution is noticed.

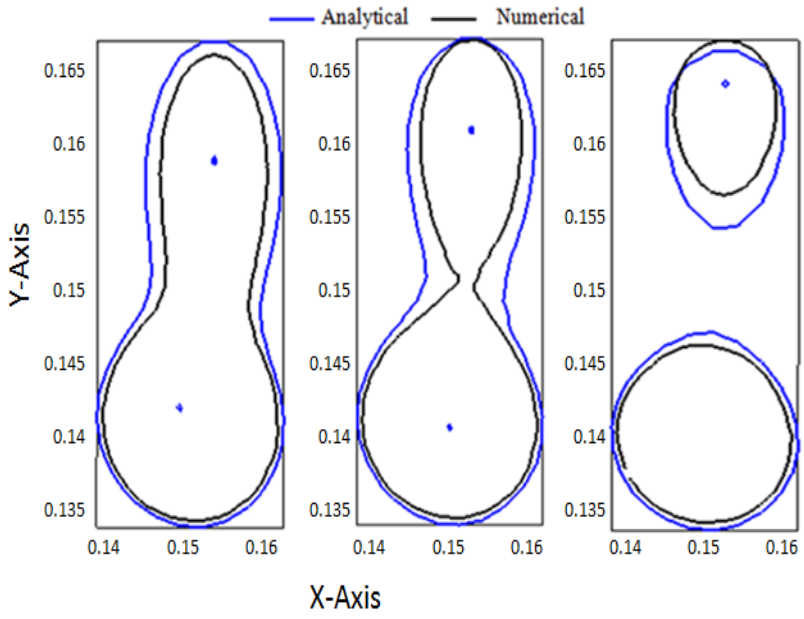

Figure 4.8. (a). The X-Y plane plot of electric field magnitude (E_{th}=800V/cm) for analytical and numerical solutions at Z= -0.15, -0.145 and - 0.14 from left to right respectively.

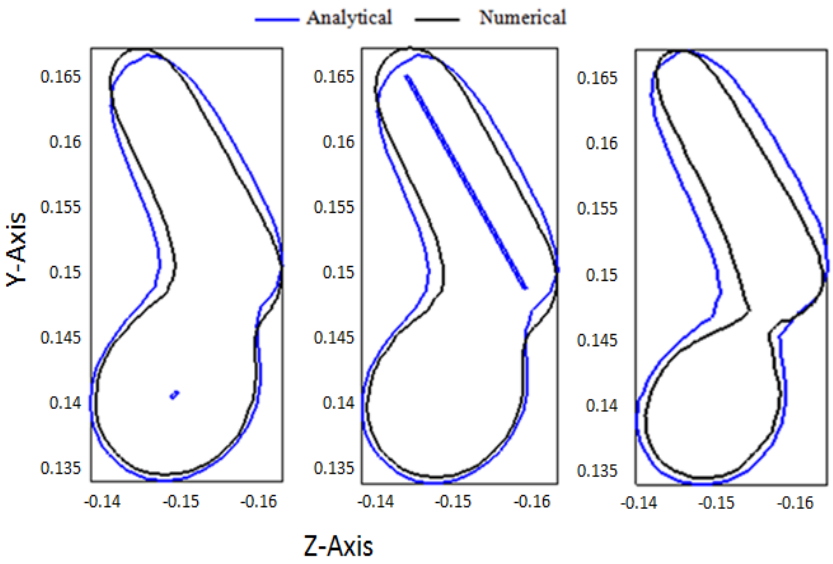

Figure 4.8. (b) The Z-Y plane plot of electric field magnitude (E_{th}=800V/cm) for analytical and numerical solutions at X= 0.145, 0.15 and 0.155 from left to right respectively.

4.3.2 Comparison with numerical (homogeneous-static and homogeneous-dynamic) simulation

In order to further validate the accuracy of our semi-analytical solution, a series of 20 models with different configurations were simulated and compared with similar numerical simulations. From the results obtained, a comparison was conducted between semi-analytical constant conductivity, numerical homogeneous static conductivity, and homogeneous dynamic conductivity models.

Table 4.3. The electrode configurations of the 20 models used in the comparison of the analytical and numerical simulations.

#	First Electrode				Second Electrode				Space
	R(m)	**L 1(m)**	**θ_1**	**φ_1**	**L2 (m)**	**θ_2**	**φ_2**	**KV**	**(m)**
1	$2.5e^{-04}$	0.02	0	0	0.02	0	0	10	0.02
2	$2.5e^{-04}$	0.02	-30	-90	0.02	-15	-90	9	0.02
3	$2.5e^{-04}$	0.02	-30	-90	0.02	30	-90	12	0.015
4	$2.5e^{-04}$	0.03	-20	-75	0.05	30	-15	12	0.02
5	$2.5e^{-04}$	0.02	-60	-35	0.02	-20	0	12	0.02
6	$2.5e^{-04}$	0.03	170	80	0.01	175	-75	13	0.02
7	$2.5e^{-04}$	0.01	0	0	0.01	0	0	7	0.01
8	$2.5e^{-04}$	0.02	10	-90	0.02	-25	90	7	0.015
9	$2.5e^{-04}$	0.015	30	-90	0.015	-30	-90	8	0.02
10	$2.5e^{-04}$	0.015	25	0	0.03	-45	0	10	0.02
11	$2.5e^{-04}$	0.02	0	-90	0.02	10	-90	14	0.025
12	$2.5e^{-04}$	0.025	0	0	0.025	0	0	12	0.025
13	$5e^{-04}$	0.015	0	0	0.015	0	0	3	0.01
14	$5e^{-04}$	0.0015	30	-90	0.015	-45	90	6	0.015
15	$5e^{-04}$	0.015	-55	-60	0.015	-35	-75	5	0.015
16	$5e^{-04}$	0.015	45	-90	0.025	-35	100	6	0.02
17	$5e^{-04}$	0.015	-50	-90	0.015	30	-90	6	0.01
18	$5e^{-04}$	0.02	40	-90	0.02	-30	90	6	0.02
19	$5e^{-04}$	0.02	-60	-90	0.04	0	-90	12	0.02
20	$5.e^{-04}$	0.025	-30	0	0.025	-45	60	5	0.01

Note: R: electrode radius, L: electrode active length; V:electric potential; φ: polar angle (theta); φ: azimuthal angle (phi) in spherical coordinate.

Table 4.3. illustrates the 20 models with the various configurations. To quantify the differences between the various electrode configurations and the three models (constant, static and dynamic), we examined the total electric current between the two electrodes, the maximum average distance and the estimated running time. Furthermore, we calculated the percentage deviation which represents the accuracy as a percent deviation between the analytical and numerical values:

$$\%\, deviation = \frac{(\text{Analytical} - \text{Nuemrical}) * 100}{\text{Numerical}} \qquad (14)$$

Results in Table 4.4. show the % deviation in the negative and positive total current passing through the electrodes of the 20 models described in Table 4.3.

Table 4.4.The total current measured in (A) for the semi-analytical, numerical homogeneous-static and numerical homogeneous-dynamic hepatic tumor conductivity.

Model	Semi-Analytical	H-Static	H - Dynamic	Ana-H-Static (%D)	Ana-H-Dynamic (%D)
1	88.9	90.1	84.3	-1.3	5.5
2	79.2	74.5	73.5	6.4	7.8
3	111.6	105.2	97.0	6.1	15.1
4	176.6	170.4	152.8	3.6	15.6
5	104.3	105.2	97.2	-0.9	7.4
6	101.5	94.6	87.7	7.4	15.7
7	38.8	40.2	38.3	-3.5	1.4
8	63.4	64.0	58.5	-0.9	8.4
9	60.6	64.3	61.9	-5.7	-2.0
10	58.8	56.5	51.4	4.2	14.5
11	91.3	88.6	81.2	3.0	12.4
12	29.8	30.9	27.4	-3.4	8.8
13	46.2	47.1	42.1	-1.9	9.7
14	65.5	65.0	57.1	0.8	14.7
15	54.2	54.5	47.8	-0.6	13.4
16	68.1	69.9	63.3	-2.5	7.6
17	166.6	159.9	143.8	4.2	15.9
18	68.2	68.0	58.6	0.3	16.4
19	125.4	127.6	118.9	-1.7	5.5
20	121	122.3	114.4	-1.1	5.8

Note H-Static: Homogeneous-Static in (A); H-Dynamic: Homogeneous-Dynamic in (A); %Div: the percentage deviation in the total current; Ana-H-Static: Analytical to the homogeneous static comparison; Ana-H-Dynamic: Analytical to the homogeneous static comparison.

The comparison between the constant analytical and homogenous-static models shows that the minimum and maximum deviations found were (0.3-7.4 mm). While the minimum and maximum deviation found between the constant analytical and homogeneous dynamic models were (2-16.4 mm). The maximum current difference was found in models 6 and 18. This difference in the electric current corresponds to the variation in electrode lengths and orientations, and thus the common electrode active length employed in electroporation treatment is of equal length. Varying the electrode orientation, length and size can also affect the total current values in the target ablation zone. Results in Table 4.4. show that changing the electrode active length increased the % deviation. The minimum value was achieved when the electrodes were inserted in

parallel and had the same length and size as indicated in models 1, 7, 11 and 12 (Table 4.3.). While with respect to the electric field distribution, a uniform distribution was noticed in all models as shown in Figure 4.2.

Furthermore, the comparisons between the three simulation models (constant, static and dynamic) indicated that the analytical to homogenous dynamic reported higher % deviation in total current than the analytical to the homogeneous static comparison. This difference was due to the increases in tissue electric conductivity during the electroporation process. Results in Table 4.5. illustrates the estimation of the maximum average distance between each two solutions (constant-analytic to homogeneous-static and constant-analytic to homogeneous-dynamic) and the maximum Euclidean distance along the X, Y, and Z-direction, indicated in Table 4.3. The comparison between the constant-analytical to numerical homogenous-static indicated a higher % difference compared with constant analytical to numerical homogeneous-dynamic. The minimum and maximum Euclidean surface distance for the comparison of analytical to numerical homogeneous static were (0.2-3.9 mm), (0.1-3.5 mm) and (0.4-3.5 mm) along the X, Y and Z-direction respectively, while the smallest and largest maximum average distance values found were (0.3-5.6 mm). Furthermore, the minimum and maximum Euclidean surface distance for the analytical to numerical homogeneous-dynamic comparison were (1.8-8.6 mm), (1.5 -7.5 mm) and (1.4-7.2 mm) along the X, Y, and Z-direction respectively, while the smallest and largest maximum average distance found was (1.4 -9.8 mm).

Table 4.5. The estimated maximum average distance (mm) between the constant to homogeneous-static and constant to homogeneous-dynamic simulations.

	Constant-Homogeneous-Static				Constant-Homogeneous-Dynamic			
Model	**Max-XD**	**Max-YD**	**Max-ZD**	**Max-AD**	**Max-XD**	**Max-YD**	**Max-ZD**	**Max-AD**
1	0.2	0.1	0.8	0.8	5.6	4.25	4.7	6.2
2	2.6	1.1	2.5	1.9	8.6	3.4	6.2	9.3
3	1.2	0.9	1.3	2.1	8.3	4.2	5.8	9.7
4	3.4	2.7	3.5	5.2	8.1	7.4	7.2	9.1
5	1.2	1.7	1.4	2.3	5.7	4	5.2	8.9
6	2.2	0.9	1.7	2.4	5.2	5.3	3.5	6.8
7	0.3	0.2	0.4	0.3	1.8	1.5	1.7	1.4
8	0.6	0.7	0.5	0.7	5.1	6.7	4.2	6.2
9	0.9	0.8	0.9	1.1	2.8	3.2	2.9	5.4
10	1.3	0.9	1.4	1.6	4.8	3.3	5.3	5.9
11	1	0.9	1.1	1.4	6.8	8.9	5.8	8.3
12	1.2	2.7	1	2.3	5.1	4.7	4.1	5.6
13	0.4	0.2	0.5	0.6	1.8	2.1	1.4	2.3
14	0.9	0.7	0.6	0.9	7.7	2.5	6.9	8.9
15	0.4	0.2	0.5	0.9	2.5	2.8	2.9	3.2
16	1.2	1.8	0.9	2.5	5.6	6.1	6.4	7.5
17	0.8	0.6	1.4	1.6	4.6	5.6	3.6	7.4
18	0.9	1.1	1.2	2.2	4	6.3	2.6	5.7
19	3.9	3.5	3.2	5.6	8.1	4.6	4.8	9.8
20	0.5	1.3	0.9	1.9	4.5	7.5	4.7	8.5

Note Max-XD: maximum distance along X-direction; Max-YD: maximum distance along Y- direction; Max-ZD: maximum distance along Z-direction; Max-AD: maximum average distance.

Table 4.6. shows the reported running time for the 20 cases described in Table 4.3. The results in Table 4.6. indicate that the fast semi-analytical algorithm reported a minimum and maximum estimated running time of (0.6-1s), while the minimum and maximum estimated running time for numerical homogeneous-static and numerical homogeneous- dynamic were (32-60s) and (131-349s) respectively.

Table 4.6. The estimated running time of constant analytical, homogeneous-static and homogeneous dynamic models.

Model	Analytical-Run-Time(s)	Homogeneous-Static Run-Time(s)	Homogeneous-Dynamic Run-Time(s)
1	1	32	185
2	0.9	52	204
3	1	57	245
4	1	60	477
5	0.9	45	140
6	0.8	51	357
7	0.9	33	131
8	0.9	44	178
9	1	48	139
10	1	43	292
11	0.8	34	159
12	0.8	36	194
13	0.9	32	176
14	1	35	318
15	1	42	346
16	0.9	38	292
17	0.9	48	166
18	1	42	294
19	1	37	219
20	1	47	349

The results depicted in Table 4.6. indicated that the fast analytical solution performed the simulation within an average time of 1s, while the numerical models were within 43s and 243s respectively.

4.3.3 Comparison with numerical simulation of anatomically realistic model

The patient specific CT image was imported and processed by our treatment planning prototype. A set of treatment planning parameters were reported for measuring the accuracy and the effectiveness of the fast analytical algorithm compared with the numerical solutions.

Table 4.7. The estimated time T (s) for processing the major treatment planning parameters.

Treatment Planning Steps	Fast-Analytical T(s)	Numerical-Static T(s)	Numerical Dynamic T(s)
Image-Preprocessing Time(s)	408	408	408
Segmentation of ROI (GTV,CTV and PTV)	764	2585	2585
3D Geometry construction	336	1563	1563
Geometry simplification	-	1874	1874
Building the numerical model	-	286	298
Estimated running time(s)	1	636	2457

The results in Table 4.7. show the estimated time in seconds for the main parameters of patient-specific electroporation treatment planning. The results indicated that the estimated time for image post-processing (loading, enhancement, and denoising) was 408s and it was the same for all models as it is an essential step in treatment planning. The threshold segmentation algorithm in high gray level tissues performed the segmentation of the target region. The segmentation of the target region was performed by the threshold segmentation algorithm in high gray level tissues, the region growing algorithm and the interactive segmentation tool for segmenting the region of interest (ROI). The segmentation estimated time (T) was 764s for the semi-analytical model and 2585s for the numerical model. The 3D geometry construction was performed by the vtkmarchingcubes algorithm and the surface editor tool. The estimated time for 3D geometry construction including surface construction, smoothing and volumetric mesh creation was 336s for semi-analytical and 1563s for numerical. The geometry simplification was performed by the simplification algorithms including decimation and solid volume creation in an estimated time (T) of 1874s. Building the numerical simulation model was performed in 286s for homogenous-static and 298s for homogeneous dynamic. The estimated running time of the numerical models was 636s for the homogeneous-static model and 2457s for the

homogeneous-dynamic model, while the fast analytical solution performed the simulation in 1s.

Figure 4.9. graphically illustrates the electric field distribution of IRE treatment planning of liver tumor. Figure 4.9.(a,b and f) shows the IRE contour lines and the 3D iso-surface plots of IRE treatment planning at $E_{thershold}$=800V/cm. Figure 4.9.(c,d, and e) shows magnified plots of Figure 4.9. results for better illustration.

Furthermore, the estimated maximum average distance found was 14.3 mm for the comparison of analytical to numerical homogeneous-static and 10.1for analytical and numerical homogeneous-dynamic simulation. The maximum Euclidian distances between constant semi-analytical and homogeneous-static were 14.7, 12.1 and 9.7 mm in X, Y; Z directions respectively, and between semi-analytical and homogeneous-dynamic were 11.7, 10.8 and 6.6mm in X, Y, Z directions respectively. Furthermore, the %deviations in total current were 5.9% in comparison with homogeneous-static and 8.1% compared with homogeneous-dynamic model.

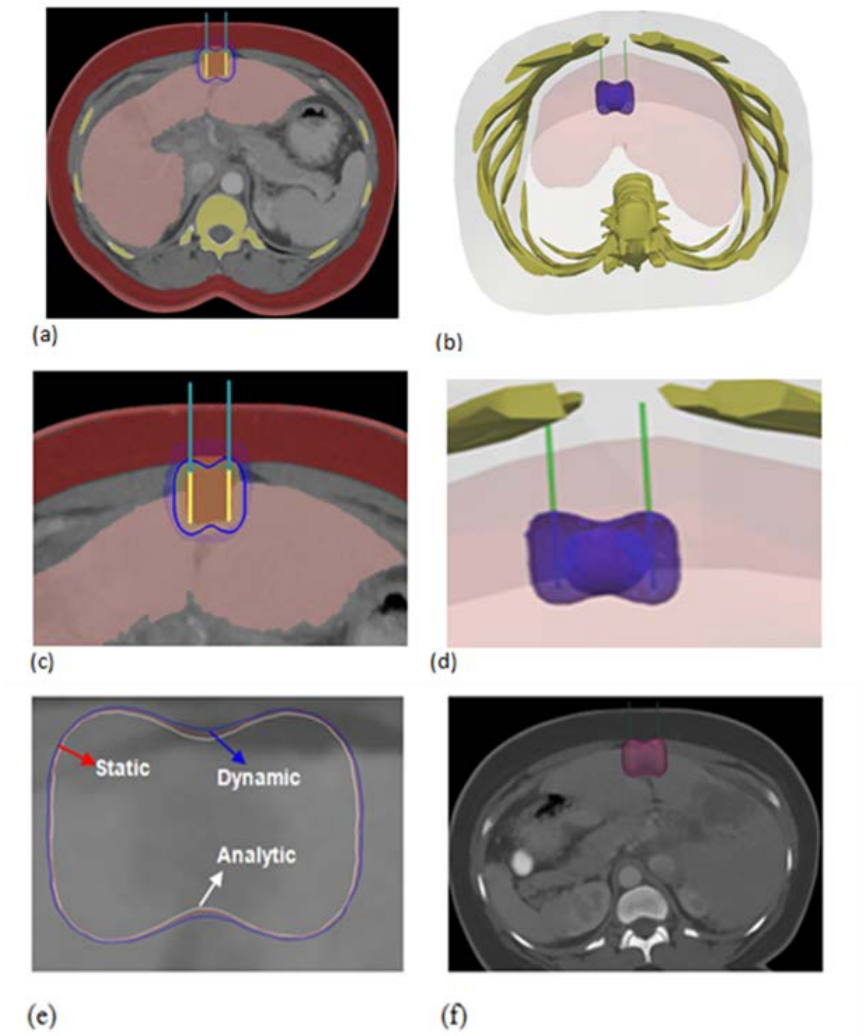

Figure 4.9. Electric field distribution calculation by the semi-analytical algorithm. (a) 2D plot of IRE contour lines at E_{th}=800V/cm; (b) the 3D iso-surface of IRE treatment plan. (c,d,f) the magnified images of (a), (b) and (f).

4.4 Discussion

Currently, electroporation-based treatment (electrochemotherapy or irreversible electroporation) have been used in clinical applications for cancer treatment[10], [70], [134], [143], [154]. Improving the electroporation treatment efficiency and safety requires controlling the electroporation parameters and reducing the damage to the healthy tissues, this increased the need for a patient-specific treatment planning prior clinical application.

In this work, a fast semi-analytical algorithm software prototype for estimating the electric field distribution was described, which can be used for electroporation (reversible and irreversible) treatment planning in clinical application. The geometry of the target region can be defined from the patient specific medical image (CT or MRI) by the use of the interactive image processing and surface reconstruction tool. The software also provides users with a simple and interactive needle electrode insertion tool, in which users can change and manipulate the electrode parameters with the additional advantage of calculating the electric field distribution in less than one second.

In similarity to the radiotherapy treatment planning procedures, the fast semi-analytical electroporation treatment planning prototype has the required protocols and algorithms for an efficient treatment plan. Covering target tissue with sufficient electric field distribution is very important in order to achieve efficient electroporation treatment. Because the electric field distribution is calculated based on analytical approximation, which is new in electroporation treatment planning, comprehensive treatment models were introduced and compared with the numerical treatment planning method. We found one attempt by Mehedi et al.[155] that indicate the possibility of using the semi-analytical solution for calculating electric field distribution in electroporation treatment.

The main purpose of the semi-analytical tool is to provide a real-time and accurate estimation of electric field distribution in the target region of interest. Currently, several image processing tools have been developed for this purpose [103], [114], [122], [157]. Unfortunately, identifying and preparing the geometry for numerical calculations of electric field distribution is a timely operation. Our tool was designed to minimize efforts and time consumed in image processing and in electric field calculation.

In the present accuracy validation study, a set of different models with various electroporation parameters has been simulated as described in Table 4.1. The comparison results between the constant conductivity semi-analytical with numerical models are in very good agreement. The accuracy of the semi-analytical model was compared by estimating the

maximum average distance between the points of the simulated results, which was used in the radiofrequency treatment planning validation [121], [158], [159]. Furthermore, we showed that a uniform electric field distribution and similar ablation zone can be calculated, even in various treatment situations and electrode configurations. The average maximum distance and the surface distance between contours showed a very good correlation between the two methods. Surprisingly, we believe that this is probably the first semi-analytical solution for electroporation treatment planning.

Results in Figure 4.2.(a) indicate a uniform ellipsoid electric field distribution around the electrodes, which produced a volume coverage similar to the numerical. This vividly supports the possibility of using the semi-analytical algorithm for providing physicians with a fast feedback on electric field distribution in clinical applications. Changing the electrode configurations for optimizing the electroporation treatment plan is intensively used in clinical applications [58], [83], [94], [150], [160]. Figures 4.3.-4.8. showed that the semi-analytical solution is able to estimate an accurate electric field distribution with respect to the changes in electrode configurations. The analysis of Euclidean surface distance showed a small difference between the two models, which is considered negligible compared to other sources of error in electroporation treatment.

For further investigating the accuracy of our semi-analytical algorithm, we compared the algorithm results with numerical homogeneous-static and homogeneous-dynamic conductivity results presented in Table 4.3. The total electric current, the maximum average distance and the estimated running time were reported and compared. The results of the %deviation in electric current indicated a notable difference between the three models (constant, static and dynamic). The maximum difference was found when the electrodes' active lengths and orientations do not match. This difference limits the semi-analytical solution to constant conductivity simulations.

Furthermore, the comparison of the maximum average distance showed a difference between the three models. The comparison between constant-semi-analytical and homogeneous-dynamic reported less difference compared to the homogeneous-static models. This was due to the non-linear changes in conductivity during electroporation, which increased the electric field distribution in the target region and produced a larger electroporated region[6],[105].

In looking at the comparison of the estimated running time between the three models. The fast semi-analytical solution can provide physicians with a fast feedback on electric field distribution within one second, while the numerical simulation is time-consuming. The numerical simulations also require hours of work from radiologists and physicians for preparing a complete electroporation treatment planning. It is worth noting that the

semi-analytical solution reduced the time consumed in the preparation of 3D models for treatment planning, as well as the time consumed in estimating the electric field distribution.

Finally, the validation results of the semi-analytical solution in an anatomically realistic liver model showed that it is a very effective solution in clinical application. It provides very fast feedback on electric field distribution compared to numerical solution, especially, when physicians change the parameters in real-time to optimize the treatment.
In summary, our goal in this study was to develop an accurate semi-analytical solution to calculate the electric field distribution for electroporation treatment planning in clinical applications. By comparing the results of semi-analytical with numerical solutions and from the results of the accuracy analysis, we managed to accomplish the study goal, and the proposed solution can be used in electroporation treatment planning for real-time clinical applications.

4.5 Conclusion

A fast and accurate semi-analytical solution for electroporation treatment planning has been developed, which can be very useful in many electroporation therapy applications. The simplicity and functionality in the identification of target region of interest, electrode insertion and electric field calculations allow the presented solution to be used in real-time treatment planning for clinical application. According to the simulation results, the semi-analytical solution matches very well with the constant conductivity numerical solution and could be used in electroporation treatment planning. Finally, the clinical workflow structure of our treatment planning prototype facilitates the clinical applications and allows physicians to easily manipulate the electroporation parameters and to perform patient-specific treatment plan.
For future work, we plan to conduct experimental and clinical studies to evaluate the clinical value of our fast semi-analytical solution. despite other electroporation treatment optimization constraints, our tool facilitates the clinical applications by fast estimation of tumor coverage with sufficient electric field distribution.

CHAPTER 5

Conclusions

5.1. General conclusions

In this thesis, treatment planning methods for electroporation-based treatments were developed and analyzed. In particular, three main objectives were achieved: it was developed a patient-specific treatment planning platform prototype based on the integration of the COMSOL solver into the GIMIAS framework, it was investigated the impact of blood vessels on IRE liver treatment and it was developed and characterized a fast semi-analytical algorithm for computing the electric field distribution generated by needle-shaped electrodes

The conclusions from this thesis can be grouped according to the three research objectives indicated above:

1. The implemented treatment planning platform prototype allows users to identify and delineate the treatment planning volumes (GTV, VTV, and PTV) on the patient medical images. The integrated algorithms for segmentation, 3D surface construction, meshing, simplifications, building the volumetric mesh and model builder plug-in successfully linked to the COMSOL FEM solver, in a transparent mode to the user, and displayed the electric field distribution. During development it was found that it was very practical to integrate the electrode insertion and Tetgen volumetric mesh generator plug-in into our prototype, as this resulted in reducing mesh problems and the computation time. Despite a high degree of automatization, during trials it was made obvious that accurate treatment planning for electroporation based therapies is a laborious process as the different tissues have to be identified, segmented and assigned properties.
2. It was determined that liver blood vessels may have a significant impact on IRE treatment in terms of volume and shape. This implies that those vessels must not be neglected in treatment planning. More importantly, the results showed that medium size vessels are likely to produce undertreatment around them, particularly in the periphery of the treatment region. These undertreatment regions correspond to volumes where the applied electric field is potentially sub-lethal. Therefore, caution is advised due to the possibility of these undertreated volumes to become new tumor nodules. It was determined that by replacing blood in the liver vasculature, or by diluting it, with isotonic low conductivity liquids this risk could be minimized.
3. The results from the developed semi-analytical algorithm for computing the electric field distribution were highly correlated with the results from a constant conductivity model solved by FEM. The semi-analytical algorithm was able to estimate and render the electric field distribution generated by needle-shaped

electrodes in less than one second. This indicates that the algorithm may be used to rapidly pre-visualize the expected treatment volume before proceeding with an accurate, but laborious and slow, computation based numerical methods.

5.2 Future perspectives and directions

In this thesis, the development of a patient-specific treatment planning methods in clinical applications was reported. The proposed numerical modeling prototype in this thesis can be improved in several ways. First, the integration of fully automatic segmentation algorithms could improve the medical image analysis, and reduce the time consumed in building the 3D geometry model. Second, building tissue-specific material properties within the proposed prototype would make the model builder more efficient.

The second part of this thesis was to assess the impact of liver blood vessels on IRE treatment efficacy. The proposed solution for recovering the impact of blood vessels on electroporation treatment by injecting the liver with isotonic low conductivity liquids could be experimentally tested and validated in animal models.

The proposed fast analytical solution for estimating the electric field distribution could be also experimentally tested and validated. Furthermore, our proposed analytical methods do not include the dynamic change in conductivity during electroporation, which could be considered in near future work. In addition, a single integrated software that includes the numerical modeling platform prototype and the fast analytical algorithm prototype could be released for clinical application in the near future.

References

[1] E. Neumann, M. Schaefer-Ridder, Y. Wang, and P. H. Hofschneider, “Gene transfer into mouse lyoma cells by electroporation in high electric fields.,” *EMBO J.*, vol. 1, no. 7, p. 841, 1982.

[2] A. V Titomirov, S. Sukharev, and E. Kistanova, “In vivo electroporation and stable transformation of skin cells of newborn mice by plasmid DNA,” *Biochim. Biophys. Acta (BBA)-Gene Struct. Expr.*, vol. 1088, no. 1, pp. 131–134, 1991.

[3] L. M. Mir, S. Orlowski, J. Belehradek, and C. Paoletti, “Electrochemotherapy potentiation of antitumour effect of bleomycin by local electric pulses,” *Eur. J. Cancer Clin. Oncol.*, vol. 27, no. 1, pp. 68–72, 1991.

[4] R. V Davalos, L. M. Mir, and B. Rubinsky, “Tissue ablation with irreversible electroporation,” *Ann. Biomed. Eng.*, vol. 33, no. 2, pp. 223–231, 2005.

[5] R. V. Davalos, L. M. Mir, and B. Rubinsky, “Tissue ablation with irreversible electroporation,” *Ann. Biomed. Eng.*, vol. 33, no. 2, pp. 223–231, 2005.

[6] A. Ivorra, B. Al-Sakere, B. Rubinsky, and L. M. Mir, “In vivo electrical conductivity measurements during and after tumor electroporation: conductivity changes reflect the treatment outcome.,” *Phys. Med. Biol.*, vol. 54, no. 19, pp. 5949–5963, 2009.

[7] D. S. Dimitrov, “Electroporation and Electrofusion of Membranes,” vol. 1, pp. 851–900, 1995.

[8] A. Ivorra, “Tissue Electroporation as a Bioelectric Phenomenon: Basic Concepts,” in *Irreversible Electroporation*, B. Rubinsky, Ed. Springer Berlin Heidelberg, 2010, pp. 23–61.

[9] M. Marty, G. Sersa, J. R. Garbay, J. Gehl, C. G. Collins, M. Snoj, V. Billard, P. F. Geertsen, J. O. Larkin, D. Miklavcic, I. Pavlovic, S. M. Paulin-Kosir, M. Cemazar, N. Morsli, D. M. Soden, Z. Rudolf, C. Robert, G. C. O’Sullivan, and L. M. Mir, “Electrochemotherapy - An easy, highly effective and safe treatment of cutaneous and subcutaneous metastases: Results of ESOPE (European Standard Operating Procedures of Electrochemotherapy) study,” *Eur. J. Cancer, Suppl.*, vol. 4, no. 11, pp. 3–13, 2006.

[10] B. Rubinsky, G. Onik, and P. Mikus, “Irreversible electroporation: a new ablation modality--clinical implications.,” *Technol. Cancer Res. Treat.*, vol. 6, no. 1, pp. 37–48, 2007.

[11] A. Ivorra and B. Rubinsky, “Historical review of irreversible electroporation in medicine,” in *Irreversible Electroporation*, Springer, 2010, pp. 1–21.

[12] U. Zimmermann, G. Pilwat, F. Beckers, and F. Riemann, “Effects of external electrical fields on cell membranes,” *Bioelectrochemistry Bioenerg.*, vol. 3, no. 1, pp. 58–83, 1976.

[13] A. J. H. Sale and W. A. Hamilton, “Effects of high electric fields on microorganisms: I. Killing of bacteria and yeasts,” *Biochim. Biophys. Acta (BBA)-General Subj.*, vol. 148, no. 3, pp. 781–788, 1967.

[14] J. Teissie and M.-P. Rols, “An experimental evaluation of the critical potential difference inducing cell membrane electropermeabilization,” *Biophys. J.*, vol. 65, no. 1, pp. 409–413, 1993.

[15] K. C. Melikov, V. A. Frolov, A. Shcherbakov, A. V Samsonov, Y. A. Chizmadzhev, and L. V Chernomordik, “Voltage-induced nonconductive pre-pores and metastable single pores in unmodified planar lipid bilayer,” *Biophys. J.*, vol. 80, no. 4, pp. 1829–1836, 2001.

[16] K. Kinosita, I. Ashikawa, N. Saita, H. Yoshimura, H. Itoh, K. Nagayama, and A. Ikegami, “Electroporation of cell membrane visualized under a pulsed-laser fluorescence microscope,” *Biophys. J.*, vol. 53, no. 6, pp. 1015–1019, 1988.

[17] U. Zimmermann, G. Pilwat, and F. Riemann, “Dielectric breakdown of cell membranes,” *Biophys. J.*, vol. 14, no. 11, pp. 881–899, 1974.

[18] B. Mercadal, P. T. Vernier, and A. Ivorra, “Dependence of Electroporation Detection Threshold on Cell Radius: An Explanation to Observations Non Compatible with Schwan???s Equation Model,” *J. Membr. Biol.*, vol. 249, no. 5, pp. 663–676, 2016.

[19] S. A. Miller and R. R. Martin, “No Title,” *Annu. Rev. Phytopathol.*, vol. 26, p. 409, 1988.

[20] A. Ivorra, B. Al-sakere, and B. Rubinsky, “Use of conductive gels for electric field homogenization increases the antitumor efficacy of electroporation therapies,” vol. 53, pp. 6605–6618, 2008.

[21] D. Cukjati, D. Batiuskaite, and D. Sel, “Sequential Finite Element Model of Tissue Electropermeabilization,” vol. 52, no. 5, pp. 816–827, 2005.

[22] W. G. M. Jr, B. A. Boone, J. D. Burgos, S. I. Gografe, M. K. Baldwin, M. L. Danielson, and M. J. Larson, “Electroporation-mediated delivery of a naked DNA plasmid expressing VEGF to the porcine heart enhances protein expression,” *Gene Ther.*, vol. 17, no. 3, pp. 419–423, 2009.

[23] J. Gehl, A. Gothelf, L. M. Mir, and J. Gehl, “Electrochemotherapy : Results of cancer treatment using enhanced delivery of bleomycin by electroporation

Electrochemotherapy : results of cancer treatment using enhanced delivery of bleomycin by electroporation," no. January, 2015.

[24] R. Heller, M. Jaroszeski, J. Leo-Messina, R. Perrot, N. Van Voorhis, D. Reintgen, and R. Gilbert, "Treatment of B16 mouse melanoma with the combination of electropermeabilization and chemotherapy," *Bioelectrochemistry Bioenerg.*, vol. 36, no. 1, pp. 83–87, 1995.

[25] G. Sersˇa, D. Miklavcˇicˇ, M. Cˇemazˇar, J. Belehradek, T. Jarm, and L. M. Mir, "Electrochemotherapy with CDDP on LPB sarcoma: comparison of the anti-tumor effectiveness in immunocompotent and immunodeficient mice," *Bioelectrochemistry Bioenerg.*, vol. 43, no. 2, pp. 279–283, 1997.

[26] L. M. Mir, P. Devauchelle, F. Quintin-Colonna, F. Delisle, S. Doliger, D. Fradelizi, J. Belehradek Jr, and S. Orlowski, "First clinical trial of cat soft-tissue sarcomas treatment by electrochemotherapy.," *Br. J. Cancer*, vol. 76, no. 12, p. 1617, 1997.

[27] Y. Tamzali, J. Teissie, and M. P. Rols, "Cutaneous tumor treatment by electrochemotherapy : preliminary clinical results in horse sarcoids," 2001.

[28] N. Tozon, V. Kodre, G. Sersa, and M. Cemazar, "Effective Treatment of Perianal Tumors in Dogs with Electrochemotherapy," vol. 846, pp. 839–845, 2005.

[29] G. Sersa, D. Miklavcic, M. Cemazar, Z. Rudolf, G. Pucihar, and M. Snoj, "Electrochemotherapy in treatment of tumours," vol. 34, pp. 232–240, 2008.

[30] S. Orlowski, J. Belehradek, C. Paoletti, and L. M. Mir, "Transient electropermeabilization of cells in culture: increase of the cytotoxicity of anticancer drugs," *Biochem. Pharmacol.*, vol. 37, no. 24, pp. 4727–4733, 1988.

[31] L. M. Mir, J. Gehl, G. Sersa, C. G. Collins, J.-R. Garbay, V. Billard, P. F. Geertsen, Z. Rudolf, G. C. O'Sullivan, and M. Marty, "Standard operating procedures of the electrochemotherapy: instructions for the use of bleomycin or cisplatin administered either systemically or locally and electric pulses delivered by the Cliniporator TM by means of invasive or non-invasive electrodes," *Eur. J. Cancer Suppl.*, vol. 4, no. 11, pp. 14–25, 2006.

[32] G. Sersa, T. Jarm, T. Kotnik, A. Coer, M. Podkrajsek, M. Sentjurc, D. Miklavcic, M. Kadivec, and S. Kranjc, "Vascular disrupting action of electroporation and electrochemotherapy with bleomycin in murine sarcoma," pp. 388–398, 2008.

[33] M. R. Ipbs, "Electrochemotherapy of horses . A preliminary clinical report," vol. 5394, no. February, 2002.

[34] V. Kodre, M. Cemazar, J. Pecar, G. Sersa, A. Cor, and N. Tozon,

"Electrochemotherapy compared to surgery for treatment of canine mast cell tumours.," *In Vivo*, vol. 23, no. 1, pp. 55–62, 2009.

[35] L. G. Salford, B. R. R. Persson, A. Brun, C. P. Ceberg, P. C. Kongstad, and L. M. Mir, "A new brain tumor therapy combining bleomycin with in vivo electropermeabilization," *Biochem. Biophys. Res. Commun.*, vol. 194, no. 2, pp. 938–943, 1993.

[36] T. Reinert, C. Serodio, F. Arthur, P. Nunes, A. Alves, and D. S. Scheliga, "Bleomycin-Induced Lung Injury," vol. 2013, 2013.

[37] M. Belehradek, C. Domenge, B. Luboinski, S. Orlowski, J. Belehradek, and L. M. Mir, "Electrochemotherapy, a new antitumor treatment. First clinical phase I trial," *Cancer*, vol. 72, no. 12, pp. 3694–3700, 1993.

[38] L. G. Campana, A. J. P. Clover, S. Valpione, P. Quaglino, J. Gehl, C. Kunte, M. Snoj, M. Cemazar, C. R. Rossi, D. Miklavcic, and G. Sersa, "Recommendations for improving the quality of reporting clinical electrochemotherapy studies based on qualitative systematic review," *Radiol. Oncol.*, vol. 50, no. 1, pp. 1–13, 2016.

[39] L. G. Campana, S. Mocellin, M. Basso, O. Puccetti, G. L. De Salvo, V. Chiarion-Sileni, A. Vecchiato, L. Corti, C. R. Rossi, and D. Nitti, "Bleomycin-based electrochemotherapy: clinical outcome from a single institution's experience with 52 patients.," *Ann. Surg. Oncol.*, vol. 16, no. November 2008, pp. 191–199, 2009.

[40] A. Gothelf, L. M. Mir, and J. Gehl, "Electrochemotherapy: Results of cancer treatment using enhanced delivery of bleomycin by electroporation," *Cancer Treat. Rev.*, vol. 29, no. 5, pp. 371–387, 2003.

[41] I. Edhemovic, E. M. Gadzijev, E. Brecelj, D. Miklavcic, B. Kos, a Zupanic, B. Mali, T. Jarm, D. Pavliha, M. Marcan, G. Gasljevic, V. Gorjup, M. Music, T. P. Vavpotic, M. Cemazar, M. Snoj, and G. Sersa, "Electrochemotherapy: a new technological approach in treatment of metastases in the liver.," *Technol. Cancer Res. Treat.*, vol. 10, no. 5, pp. 475–485, 2011.

[42] I. Skarlatos, G. Kyrgias, E. Mosa, X. Provatopoulou, M. Spyrou, and K. Theodorou, "Bd6475Ca51Eea37288E618Fa9493354F42853F1," vol. 274, pp. 265–274, 2011.

[43] V. Granata, R. Fusco, M. Piccirillo, R. Palaia, A. Petrillo, S. Lastoria, and F. Izzo, "Electrochemotherapy in locally advanced pancreatic cancer: Preliminary results," *Int. J. Surg.*, vol. 18, pp. 230–236, 2015.

[44] C. Collins, M. Tangney, and G. O. Sullivan, "Electrochemotherapy : Aspects of preclinical development and early clinical experience," no. May 2017, 2007.

[45] J. F. Edd, L. Horowitz, R. V. Davalos, L. M. Mir, and B.

Rubinsky, “In vivo results of a new focal tissue ablation technique: Irreversible electroporation,” *IEEE Trans. Biomed. Eng.*, vol. 53, no. 7, pp. 1409–1415, 2006.

[46] R. E. Neal and R. V. Davalos, “The feasibility of irreversible electroporation for the treatment of breast cancer and other heterogeneous systems,” *Ann. Biomed. Eng.*, vol. 37, no. 12, pp. 2615–2625, 2009.

[47] J. Rubinsky, G. Onik, P. Mikus, and B. Rubinsky, “Optimal parameters for the destruction of prostate cancer using irreversible electroporation,” *J. Urol.*, vol. 180, no. 6, pp. 2668–2674, 2008.

[48] N. Bao, T. T. Le, J.-X. Cheng, and C. Lu, “Microfluidic electroporation of tumor and blood cells: observation of nucleus expansion and implications on selective analysis and purging of circulating tumor cells,” *Integr. Biol.*, vol. 2, no. 2–3, p. 113, 2010.

[49] R. E. Neal and R. V. Davalos, “The feasibility of irreversible electroporation for the treatment of breast cancer and other heterogeneous systems,” *Ann. Biomed. Eng.*, vol. 37, no. 12, pp. 2615–2625, 2009.

[50] M. B. Sano, C. B. Arena, M. R. DeWitt, D. Saur, and R. V. Davalos, “In-vitro bipolar nano- and microsecond electro-pulse bursts for irreversible electroporation therapies,” *Bioelectrochemistry*, vol. 100, pp. 69–79, 2014.

[51] C. B. Arena, C. S. Szot, P. A. Garcia, M. N. Rylander, and R. V. Davalos, “A three-dimensional in vitro tumor platform for modeling therapeutic irreversible electroporation,” *Biophys. J.*, vol. 103, no. 9, pp. 2033–2042, 2012.

[52] G. C. Troiano, L. Tung, V. Sharma, and K. J. Stebe, “The reduction in electroporation voltages by the addition of a surfactant to planar lipid bilayers.,” *Biophys. J.*, vol. 75, no. 2, pp. 880–8, 1998.

[53] P. Kramar, D. Miklavcic, and A. M. Lebar, “A system for the determination of planar lipid bilayer breakdown voltage and its applications,” *IEEE Trans. Nanobioscience*, vol. 8, no. 2, pp. 132–138, 2009.

[54] Q. Castellví, A. Villanueva, M. Iglesias, R. Quesada, and C. Pañella, “Long-term effectiveness of irreversible electroporation in a murine model of colorectal liver metastasis,” *Nat. Publ. Gr.*, no. November 2016, pp. 1–8, 2017.

[55] R. Cannon, S. Ellis, D. Hayes, G. Narayanan, and R. C. G. Martin, “Safety and early efficacy of irreversible electroporation for hepatic tumors in proximity to vital structures,” *J. Surg. Oncol.*, vol. 107, no. 5, pp. 544–549, 2013.

[56] A. Eller, A. Schmid, J. Schmidt, M. May, M. Brand, M. Saake, M. Uder, and M. Lell, “Local Control of Perivascular Malignant Liver

Lesions Using Percutaneous Irreversible Electroporation: Initial Experiences," *Cardiovasc. Intervent. Radiol.*, 2014.

[57] Y. Guo, Y. Zhang, R. Klein, G. M. Nijm, A. V. Sahakian, R. a. Omary, G. Y. Yang, and A. C. Larson, "Irreversible electroporation therapy in the liver: Longitudinal efficacy studies in a rat model of hepatocellular carcinoma," *Cancer Res.*, vol. 70, no. 4, pp. 1555–1563, 2010.

[58] L. Appelbaum, E. Ben-David, M. Faroja, Y. Nissenbaum, J. Sosna, S. N. Goldberg, and F. Arrays, "Irreversible electroporation ablation: creation of large-volume ablation zones in in vivo porcine liver with four-electrode arrays.," *Radiology*, vol. 270, no. 2, pp. 416–24, 2014.

[59] P. Sánchez-Velázquez, Q. Castellví, A. Villanueva, R. Quesada, C. Pañella, M. Cáceres, D. Dorcaratto, A. Andaluz, X. Moll, M. Trujillo, J. M. Burdío, E. Berjano, L. Grande, A. Ivorra, and F. Burdío, "Irreversible electroporation of the liver: is there a safe limit to the ablation volume?," *Sci. Rep.*, vol. 6, no. April, p. 23781, 2016.

[60] E. Ben-David, M. Ahmed, M. Faroja, M. Moussa, A. Wandel, J. Sosna, L. Appelbaum, I. Nissenbaum, and S. N. Goldberg, "Irreversible Electroporation : Treatment Effect Is Susceptible," *Radiology*, vol. 269, no. 3, 2013.

[61] J. F. Edd, L. Horowitz, R. V Davalos, L. M. Mir, and B. Rubinsky, "In vivo results of a new focal tissue ablation technique: irreversible electroporation," *IEEE Trans. Biomed. Eng.*, vol. 53, no. 7, pp. 1409–1415, 2006.

[62] P. A. Garcia, J. H. Rossmeisl, R. E. Neal, T. L. Ellis, J. D. Olson, N. Henao-Guerrero, J. Robertson, and R. V Davalos, "Intracranial nonthermal irreversible electroporation: in vivo analysis," *J. Membr. Biol.*, vol. 236, no. 1, pp. 127–136, 2010.

[63] A. Ivorra and B. Rubinsky, "In vivo electrical impedance measurements during and after electroporation of rat liver," *Bioelectrochemistry*, vol. 70, no. 2, pp. 287–295, 2007.

[64] D. Miklavčič, D. Šemrov, H. Mekid, and L. M. Mir, "A validated model of in vivo electric field distribution in tissues for electrochemotherapy and for DNA electrotransfer for gene therapy," *Biochim. Biophys. Acta (BBA)-General Subj.*, vol. 1523, no. 1, pp. 73–83, 2000.

[65] P. A. Garcia, J. H. Rossmeisl, R. E. Neal, T. L. Ellis, and R. V Davalos, "A parametric study delineating irreversible electroporation from thermal damage based on a minimally invasive intracranial procedure," *Biomed. Eng. Online*, vol. 10, no. 1, p. 34, 2011.

[66] A. Deodhar, T. Dickfeld, G. W. Single, W. C. Hamilton Jr, R. H.

Thornton, C. T. Sofocleous, M. Maybody, M. Gónen, B. Rubinsky, and S. B. Solomon, “Irreversible electroporation near the heart: ventricular arrhythmias can be prevented with ECG synchronization,” *Am. J. Roentgenol.*, vol. 196, no. 3, pp. W330–W335, 2011.

[67] J. J. Wendler, M. Pech, S. Blaschke, M. Porsch, A. Janitzky, M. Ulrich, O. Dudeck, J. Ricke, and U.-B. Liehr, “Angiography in the isolated perfused kidney: radiological evaluation of vascular protection in tissue ablation by nonthermal irreversible electroporation,” *Cardiovasc. Intervent. Radiol.*, vol. 35, no. 2, pp. 383–390, 2012.

[68] K. R. Thomson, W. Cheung, S. J. Ellis, D. Federman, H. Kavnoudias, D. Loader-Oliver, S. Roberts, P. Evans, C. Ball, and A. Haydon, “Investigation of the Safety of Irreversible Electroporation in Humans,” *J. Vasc. Interv. Radiol.*, vol. 22, no. 5, pp. 611–621, May 2011.

[69] M. Pech, A. Janitzky, J. Wendler, C. Strang, S. Blaschke, O. Dudeck, J. Ricke, and U.-B. Liehr, “Irreversible Electroporation of Renal Cell Carcinoma: A First-in-Man Phase I Clinical Study,” *Cardiovasc. Intervent. Radiol.*, vol. 34, no. 1, pp. 132–138, 2011.

[70] P. Philips, D. Hays, and R. C. G. Martin, “Irreversible electroporation ablation (IRE) of unresectable soft tissue tumors: Learning curve evaluation in the first 150 patients treated,” *PLoS One*, vol. 8, no. 11, pp. 1–9, 2013.

[71] H. J. Scheffer, L. G. P. H. Vroomen, K. Nielsen, A. A. J. M. van Tilborg, E. F. I. Comans, C. van Kuijk, B. B. van der Meijs, J. van den Bergh, P. M. P. van den Tol, and M. R. Meijerink, “Colorectal liver metastatic disease: efficacy of irreversible electroporation-a single-arm phase II clinical trial (COLDFIRE-2 trial).,” *BMC Cancer*, vol. 15, p. 772, 2015.

[72] R. C. G. Martin, K. McFarland, S. Ellis, and V. Velanovich, “Irreversible Electroporation in Locally Advanced Pancreatic Cancer: Potential Improved Overall Survival.,” *Ann. Surg. Oncol.*, no. November 2012, pp. 443–449, 2012.

[73] T. P. Kingham, A. M. Karkar, M. I. D’Angelica, P. J. Allen, R. P. Dematteo, G. I. Getrajdman, C. T. Sofocleous, S. B. Solomon, W. R. Jarnagin, and Y. Fong, “Ablation of perivascular hepatic malignant tumors with irreversible electroporation,” *J. Am. Coll. Surg.*, vol. 215, no. 3, pp. 379–387, 2012.

[74] M. Wichtowski, P. Nowaczyk, J. Kocur, and D. Murawa, “Irreversible electroporation in the treatment of locally advanced pancreas and liver metastases of colorectal carcinoma.,” *Contemp. Oncol. (Poznań, Poland)*, vol. 20, no. 1, pp. 39–44, 2016.

[75] R. E. Neal, P. a. Garcia, J. L. Robertson, and R. V. Davalos,

"Experimental characterization and numerical modeling of tissue electrical conductivity during pulsed electric fields for irreversible electroporation treatment planning," *IEEE Trans. Biomed. Eng.*, vol. 59, no. 4, pp. 1076–1085, 2012.

[76] R. E. Neal, P. a. Garcia, H. Kavnoudias, F. Rosenfeldt, C. a. Mclean, V. Earl, J. Bergman, R. V. Davalos, and K. R. Thomson, "<italic>In Vivo</italic> Irreversible Electroporation Kidney Ablation: Experimentally Correlated Numerical Models," *IEEE Trans. Biomed. Eng.*, vol. 62, no. 2, pp. 561–569, 2015.

[77] H. Ren, E. Campos-Nanez, Z. Yaniv, F. Banovac, H. Abeledo, N. Hata, and K. Cleary, "Treatment planning and image guidance for radiofrequency ablation of large tumors," *IEEE J. Biomed. Heal. Informatics*, vol. 18, no. 3, pp. 920–928, 2014.

[78] H. G. Menzel, "The international commission on radiation units and measurements," *J. ICRU*, vol. 10, no. 2, pp. 1–35, 2010.

[79] K. Cleary, "Original Datasets," 2007.

[80] J. T. Mortimep and C. Western, "a Numerical Analysis of the Electric Field," vol. 13, no. 2, pp. 912–913, 1991.

[81] S. Čorović, L. M. Mir, and D. Miklavčič, "In vivo muscle electroporation threshold determination: Realistic numerical models and in vivo experiments," *J. Membr. Biol.*, vol. 245, pp. 509–520, 2012.

[82] K. N. Kiousis, A. X. Moronis, and A. S. Aegaleo, "Modeling and Analysis of the Electric Field and Potential Distribution in a Wire-Cylinder Air Gap 2 Numerical Modeling," no. 4, pp. 35–40.

[83] K. Kurata, S. Nomura, and H. Takamatsu, "Three-dimensional analysis of irreversible electroporation: Estimation of thermal and non-thermal damage," *Int. J. Heat Mass Transf.*, vol. 72, pp. 66–74, 2014.

[84] S. Corovic, I. Lackovic, P. Sustaric, T. Sustar, T. Rodic, and D. Miklavcic, "Modeling of electric field distribution in tissues during electroporation.," *Biomed. Eng. Online*, vol. 12, no. 1, p. 16, 2013.

[85] A. Guimera, A. Ivorra, G. Gabriel, and R. Villa, "Non-invasive assessment of corneal endothelial permeability by means of electrical impedance measurements," *Med. Eng. Phys.*, vol. 32, pp. 1107–1115, 2010.

[86] D. Miklavcic, M. Snoj, A. Zupanic, B. Kos, M. Cemazar, M. Kropivnik, M. Bracko, T. Pecnik, E. Gadzijev, and G. Sersa, "Towards treatment planning and treatment of deep-seated solid tumors by electrochemotherapy.," *Biomed. Eng. Online*, vol. 9, p. 10, 2010.

[87] C. Maja, "The Importance of Electric Field Distribution for Effective in Vivo Electroporation of Tissues," vol. 74, no. May, pp. 2152–2158, 1998.

[88] D. Šemrov and D. Miklavčič, "Calculation of the electrical parameters in electrochemotherapy of solid tumours in mice," *Comput. Biol. Med.*, vol. 28, no. 4, pp. 439–448, 1998.

[89] D. Miklavcic, D. Sel, D. Cukjati, D. Batiuskaite, T. Slivnik, and L. Mir, "Sequential finite element model of tissue electropermeabilisation.," *Conf. Proc. IEEE Eng. Med. Biol. Soc.*, vol. 5, no. 5, pp. 3551–3554, 2004.

[90] A. Ivorra, J. Villemejane, and L. M. Mir, "Electrical modeling of the influence of medium conductivity on electroporation," *Phys. Chem. Chem. Phys.*, vol. 12, no. 34, pp. 10055–10064, 2010.

[91] A. Golberg, B. G. Bruinsma, B. E. Uygun, and M. L. Yarmush, "Tissue heterogeneity in structure and conductivity contribute to cell survival during irreversible electroporation ablation by 'electric field sinks,'" *Sci. Rep.*, vol. 5, p. 8485, 2015.

[92] D. Haemmerich, D. J. Schutt, a. S. Wright, J. G. Webster, and D. M. Mahvi, "Electrical conductivity measurement of excised human metastatic liver tumours before and after thermal ablation," *Physiol. Meas.*, vol. 30, no. 5, p. 459, 2009.

[93] P. a. Garcia, J. H. Rossmeisl, and R. V. Davalos, "Electrical conductivity changes during irreversible electroporation treatment of brain cancer," *Proc. Annu. Int. Conf. IEEE Eng. Med. Biol. Soc. EMBS*, pp. 739–742, 2011.

[94] O. O. Adeyanju, H. M. Al-Angari, and A. V. Sahakian, *The optimization of needle electrode number and placement for irreversible electroporation of hepatocellular carcinoma*, vol. 46, no. 2. 2012.

[95] K. R. Thomson, H. Kavnoudias, and R. E. N. Ii, "Introduction to Irreversible Electroporation — Principles and Techniques," *Tech. Vasc. Interv. Radiol.*, vol. 18, no. 3, pp. 128–134, 2015.

[96] D. Pavliha, B. Kos, M. Mar, G. Ser, and D. Miklav, "Bioelectrochemistry Patient-speci fi c treatment planning of electrochemotherapy : Procedure design and possible pitfalls," vol. 87, pp. 265–273, 2012.

[97] S. Gabriel, R. W. Lau, and C. Gabriel, "The dielectric properties of biological tissues: II. Measurements in the frequency range 10 Hz to 20 GHz.," *Phys. Med. Biol.*, vol. 41, no. 11, pp. 2251–2269, 1996.

[98] C. Gabriel, a Peyman, and E. H. Grant, "Electrical conductivity of tissue at frequencies below 1 MHz.," *Phys. Med. Biol.*, vol. 54, no. 16, pp. 4863–4878, 2009.

[99] D. Pavliha, B. Kos, M. Marc, G. Sers, and D. Miklavc, "Planning of Electroporation-Based Treatments Using Web-Based Treatment-Planning Software," pp. 833–842, 2013.

[100] G. Bertino, G. Sersa, F. De Terlizzi, A. Occhini, C. C. Plaschke, A.

Groselj, C. Langdon, J. J. Grau, J. A. McCaul, D. Heuveling, M. Cemazar, P. Strojan, R. De Bree, C. R. Leemans, I. Wessel, J. Gehl, and M. Benazzo, "European Research on Electrochemotherapy in Head and Neck Cancer (EURECA) project: Results of the treatment of skin cancer," *Eur. J. Cancer*, vol. 63, pp. 41–52, 2016.

[101] C. Jiang, R. V Davalos, and J. C. Bischof, "A Review of Basic to Clinical Studies of Irreversible Electroporation Therapy," vol. 62, no. 1, pp. 4–20, 2015.

[102] M. Marčan, B. Kos, and D. Miklavčič, "Effect of Blood Vessel Segmentation on the Outcome of Electroporation-Based Treatments of Liver Tumors," *PLoS One*, vol. 10, no. 5, p. e0125591, 2015.

[103] D. Šel, S. Mazeres, J. Teissie, and D. Miklavčič, "Finite-Element Modeling of Needle Electrodes in Tissue From the Perspective of Frequent Model Computation," *IEEE Trans. Biomed. Eng.*, vol. 50, no. 11, pp. 1221–1232, 2003.

[104] E. Ben-David, L. Appelbaum, J. Sosna, I. Nissenbaum, and S. N. Goldberg, "Characterization of irreversible electroporation ablation in in vivo,porcine liver," *Am. J. Roentgenol.*, vol. 198, no. 1, 2012.

[105] T. Kotnik, W. Frey, M. Sack, S. Haberl Meglič, M. Peterka, and D. Miklavčič, "Electroporation-based applications in biotechnology," *Trends Biotechnol.*, vol. 33, no. 8, pp. 1–9, 2015.

[106] M. Hjouj, J. Lavee, D. Last, D. Guez, D. Daniels, S. Sharabi, B. Rubinsky, and Y. Mardor, "The effect of blood flow on magnetic resonance imaging of non thermal irreversible electroporation.," *Sci. Rep.*, vol. 3, p. 3088, 2013.

[107] J. F. Edd and R. V Davalos, "Mathematical modeling of irreversible electroporation for treatment planning.," *Technol. Cancer Res. Treat.*, vol. 6, no. 4, pp. 275–86, 2007.

[108] B. Kos, P. Voigt, D. Miklavcic, and M. Moche, "Careful treatment planning enables safe ablation of liver tumors adjacent to major blood vessels by percutaneous irreversible electroporation (IRE)," 2015.

[109] D. Dissertation, "Treatment planning in biomedical applications of electroporation," 2010.

[110] D. Pavliha, B. Kos, A. Županič, M. Marčan, G. Serša, and D. Miklavčič, "Patient-specific treatment planning of electrochemotherapy: Procedure design and possible pitfalls," *Bioelectrochemistry*, vol. 87, pp. 265–273, 2012.

[111] I. Wolf, M. Vetter, I. Wegner, M. Nolden, T. Böttger, M. Hastenteufel, M. Schöbinger, T. Kunert, H.-P. Meinzer, and D. Krebsforschungszentrum, "The Medical Imaging Interaction Toolkit (MITK)–a toolkit facilitating the creation of interactive

software by extending VTK and ITK," in *Proc. of SPIE Vol*, 2004, vol. 5367, p. 17.

[112] W. J. Schroeder, K. Martin, L. Avila, and C. Law, "The Visualization Toolkit User's Guide. Kitware," *Inc., Clift. Park. New York, 380pp*, 2001.

[113] L. Ibanez, W. Schroeder, L. Ng, and J. Cates, "The ITK Software Guide. Insight Software Consortium; 2003." .

[114] I. Larrabide, P. Omedas, Y. Martelli, X. Planes, M. Nieber, J. a. Moya, C. Butakoff, R. Sebastián, O. Camara, M. De Craene, B. H. Bijnens, and A. F. Frangi, "GIMIAS: An open source framework for efficient development of research tools and clinical prototypes," *Lect. Notes Comput. Sci. (including Subser. Lect. Notes Artif. Intell. Lect. Notes Bioinformatics)*, vol. 5528, pp. 417–426, 2009.

[115] J. Tian, J. Xue, Y. Dai, J. Chen, and J. Zheng, "A novel software platform for medical image processing and analyzing," *IEEE Trans. Inf. Technol. Biomed.*, vol. 12, no. 6, pp. 800–812, 2008.

[116] J. Schöberl, "NETGEN-4.3," *Ref. Manual, January*, 2004.

[117] H. Si and K. Gärtner, "Meshing piecewise linear complexes by constrained Delaunay tetrahedralizations," in *Proceedings of the 14th international meshing roundtable*, 2005, pp. 147–163.

[118] A. Manuscript and T. Planning, "NIH Public Access," vol. 18, no. 3, pp. 920–928, 2014.

[119] S. Prakash, M. P. Karnes, E. K. Sequin, J. D. West, C. L. Hitchcock, S. D. Nichols, M. Bloomston, S. R. Abdel-Misih, C. R. Schmidt, E. W. Martin, S. P. Povoski, and V. V Subramaniam, "Ex vivo electrical impedance measurements on excised hepatic tissue from human patients with metastatic colorectal cancer," *Physiol. Meas.*, vol. 36, no. 2, pp. 315–328, 2015.

[120] R. Qasrawi, L. Silve, and F. Burdı, "Anatomically Realistic Simulations of Liver Ablation by Irreversible Electroporation : Impact of Blood Vessels on Ablation Volumes and Undertreatment," 2017.

[121] C. Rieder, T. Kr??ger, C. Schumann, and H. K. Hahn, "GPu-based real-time approximation of the ablation zone for radiofrequency ablation," *IEEE Trans. Vis. Comput. Graph.*, vol. 17, no. 12, pp. 1812–1821, 2011.

[122] M. Marcan, D. Pavliha, M. M. Music, I. Fuckan, R. Magjarevic, and D. Miklavcic, "Segmentation of Hepatic Vessels from Mri Images for Planning of Electroporation-Based Treatments in the Liver," *Radiol. Oncol.*, pp. 1–15, 2014.

[123] M. Pech, A. Janitzky, J. J. Wendler, C. Strang, S. Blaschke, O. Dudeck, J. Ricke, and U. B. Liehr, "Irreversible electroporation of renal cell carcinoma: A first-in-man phase i clinical study,"

Cardiovasc. Intervent. Radiol., vol. 34, no. 1, pp. 132–138, 2011.
[124] G. Narayanan, T. Froud, R. Suthar, and K. Barbery, "Irreversible electroporation of hepatic malignancy," *Semin. Intervent. Radiol.*, vol. 30, no. 1, pp. 67–73, 2013.
[125] Y. J. Lee, D. S. K. Lu, F. Osuagwu, and C. Lassman, "Irreversible Electroporation in Porcine Liver: Short- and Long-Term Effect on the Hepatic Veins and Adjacent Tissue by CT With Pathological Correlation," *Invest. Radiol.*, vol. 47, no. 11, 2012.
[126] E. Maor, A. Ivorra, J. Leor, and B. Rubinsky, "The Effect of Irreversible Electroporation on Blood Vessels," *Technol. Cancer Res. Treat.*, vol. 6, no. 4, pp. 307–312, 2007.
[127] E. W. Lee, C. Chen, V. E. Prieto, S. M. Dry, C. T. Loh, and S. T. Kee, "Advanced hepatic ablation technique for creating complete cell death: irreversible electroporation 1," *Radiology*, vol. 255, no. 2, pp. 426–433, 2010.
[128] G. Narayanan, *Irreversible Electroporation*, vol. 32, no. 4. 2015.
[129] R. Qasrawi and A. Ivorra, "Impact of liver vasculature on electric field distribution during electroporation treatments : an anatomically realistic numerical study," in *6th European Conference of the International Federation for Medical and Biological Engineering*, 2014, pp. 573–576.
[130] A. Golberg, B. G. Bruinsma, B. E. Uygun, and M. L. Yarmush, "Tissue heterogeneity in structure and conductivity contribute to cell survival during irreversible electroporation ablation by 'electric field sinks,'" *Sci. Rep.*, vol. 5, p. 8485, 2015.
[131] D. S. Shin, M. S. Chung, J. W. Lee, J. S. Park, J. Chung, S. B. Lee, and S. H. Lee, "Advanced surface reconstruction technique to build detailed surface models of the liver and neighboring structures from the Visible Korean Human," *J. Korean Med. Sci.*, vol. 24, no. 3, pp. 375–383, 2009.
[132] K. P. Charpentier, F. Wolf, L. Noble, B. Winn, M. Resnick, and D. E. Dupuy, "Irreversible electroporation of the liver and liver hilum in swine," *Hpb*, vol. 13, no. 3, pp. 168–173, 2011.
[133] L. Silve, R. Qasrawi, and A. Ivorra, "Incorporation of the Blood Vessel Wall into Electroporation Simulations," pp. 1–4.
[134] H. J. Scheffer, K. Nielsen, M. C. de Jong, A. A. J. M. van Tilborg, J. M. Vieveen, A. R. A. Bouwman, S. Meijer, C. van Kuijk, P. M. P. van den Tol, and M. R. Meijerink, "Irreversible electroporation for nonthermal tumor ablation in the clinical setting: a systematic review of safety and efficacy," *J. Vasc. Interv. Radiol.*, vol. 25, no. 7, pp. 997–1011, 2014.
[135] W.-Y. Lau, E. C. Lai, and S. H. Lau, "Methods of vascular control technique during liver resection: a comprehensive review," *Hepatobiliary Pancreat Dis Int*, vol. 9, no. 5, pp. 473–481, 2010.

[136] A. Alves, R. Adam, P. Majno, V. Delvart, D. Azoulay, D. Castaing, and H. Bismuth, “Hepatic resection for metastatic renal tumors: is it worthwhile?,” *Ann. Surg. Oncol.*, vol. 10, no. 6, pp. 705–710, 2003.

[137] A. M. Averbach, O. A. Stuart, T. A. Sugarbaker, A. D. Stephens, V. Fernandez-Trigo, F. Shamsa, and P. H. Sugarbaker, “Pharmacokinetic studies of intraaortic stop-flow infusion with 14 C-labeled mitomycin C,” *J. Surg. Res.*, vol. 59, no. 3, pp. 415–419, 1995.

[138] A. V Wolf and A. V Wolf, *Aqueous solutions and body fluids : their concentrative properties and conversion tables*. New York; London: Hoeber Medical Division Harper & Row Publ, 1966.

[139] S. Gananadha and D. L. Morris, “Saline infusion markedly reduces impedance and improves efficacy of pulmonary radiofrequency ablation,” *Cardiovasc. Intervent. Radiol.*, vol. 27, no. 4, pp. 361–365, 2004.

[140] A. R. Gillams and W. R. Lees, “CT mapping of the distribution of saline during radiofrequency ablation with perfusion electrodes,” *Cardiovasc. Intervent. Radiol.*, vol. 28, no. 4, pp. 476–480, 2005.

[141] F. M. André, J. Gehl, G. Sersa, V. Préat, P. Hojman, J. Eriksen, M. Golzio, M. Cemazar, N. Pavselj, M.-P. Rols, D. Miklavcic, E. Neumann, J. Teissié, and L. M. Mir, “Efficiency of high- and low-voltage pulse combinations for gene electrotransfer in muscle, liver, tumor, and skin.,” *Hum. Gene Ther.*, vol. 19, no. 11, pp. 1261–1271, 2008.

[142] R. C. G. Martin, K. McFarland, S. Ellis, and V. Velanovich, “Irreversible Electroporation in Locally Advanced Pancreatic Cancer: Potential Improved Overall Survival.,” *Ann. Surg. Oncol.*, no. August, pp. 443–449, 2012.

[143] B. Rubinsky, D. Ph, G. Onik, P. Mikus, and B. Sc, “Irreversible Electroporation : A New Ablation Modality – Clinical Implications,” vol. 6, no. 1, 2015.

[144] J. Zeng, G. Liu, Z. Li, Y. Yang, G. Fang, and R. Li, “The Safety and Efficacy of Irreversible Electroporation for Large Hepatocellular Carcinoma,” vol. 16, no. 1, pp. 120–124, 2017.

[145] M. Valerio, L. Dickinson, A. Ali, N. Ramachadran, I. Donaldson, N. Mccartan, A. Freeman, H. U. Ahmed, and M. Emberton, “Nanoknife Electroporation Ablation Trial : A Prospective Development Study Investigating Focal Irreversible Electroporation for Localized Prostate Cancer,” *J. Urol.*, vol. 197, no. 3, pp. 647–654, 2017.

[146] J. Tasu, G. Vesselle, G. Herpe, J. Richer, S. Boucecbi, S. Vélasco, M. Carretier, B. Debeane, and D. Tougeron, “Irreversible electroporation for locally advanced pancreatic cancer,” *Diagn.*

Interv. Imaging, vol. 97, no. 12, pp. 1297–1304, 2016.
[147] R. Lencioni, L. Crocetti, and G. Narayanan, "Irreversible Electroporation in the Treatment of Hepatocellular Carcinoma," *Tech. Vasc. Interv. Radiol.*, vol. 18, no. 3, pp. 135–139, 2015.
[148] L. G. Campana, S. Galuppo, and S. Valpione, "Treatment of cutaneous metastases of breast cancer with electrochemotherapy : what is the magnitude of clinical benefit ?," *Breast Cancer Res. Treat.*, vol. 24, pp. 3–5, 2017.
[149] M. Figini, X. Wang, T. Lyu, Z. Su, D. Procissi, V. Yaghmai, and C. Andrew, "Preclinical and clinical evaluation of the liver tumor irreversible electroporation by magnetic resonance imaging," vol. 9, no. 2, pp. 580–590, 2017.
[150] L. Appelbaum, E. Ben-David, M. Faroja, Y. Nissenbaum, J. Sosna, and S. Goldberg, "Irreversible electroporation ablation : Creation of large-volume ablation zones in in vivo porcine liver with four-electrode arrays," *Radiology*, vol. 270, no. 2, pp. 416–424, 2014.
[151] T. Kotnik, P. Kramar, G. Pucihar, D. Miklavcic, and M. Tarek, "Cell membrane electroporation-Part 1: The phenomenon," *IEEE Electr. Insul. Mag.*, vol. 28, no. 5, pp. 14–23, 2012.
[152] G. Sersa, T. Cufer, S. Marija, M. Cemazar, and M. Snoj, "Electrochemotherapy of chest wall breast cancer recurrence," *Cancer Treat. Rev.*, vol. 38, no. 5, pp. 379–386, 2012.
[153] G. Di Monta, C. Caracò, E. Simeone, A. M. Grimaldi, U. Marone, M. Di Marzo, V. Vanella, L. Festino, M. Palla, S. Mori, N. Mozzillo, and P. A. Ascierto, "Electrochemotherapy efficacy evaluation for treatment of locally advanced stage III cutaneous squamous cell carcinoma : a 22 - cases retrospective analysis," *J. Transl. Med.*, pp. 1–8, 2017.
[154] G. Schmidt, I. Juhasz-Böss, E.-F. Solomayer, and D. Herr, "Electrochemotherapy in Breast Cancer: A Review of References," *Geburtshilfe Frauenheilkd.*, vol. 74, no. 6, pp. 557–562, Jun. 2014.
[155] M. M. Hasan and C. Drapaca, "A Fractional Order Model for Local Electric Fields in Tissues," in *Mechanics of Biological Systems and Materials, Volume 7*, Springer, 2015, pp. 75–79.
[156] J. Malmivuo and R. Plonsey, *Bioelectromagnetism: principles and applications of bioelectric and biomagnetic fields*. Oxford University Press, USA, 1995.
[157] T. Wimmer, G. Srimathveeravalli, N. Gutta, P. C. Ezell, S. Monette, T. P. Kingham, M. Maybody, J. C. Durack, Y. Fong, and S. B. Solomon, "Comparison of Simulation-based Treatment Planning with Imaging and Pathology Outcomes for Percutaneous CT-guided Irreversible Electroporation of the Porcine Pancreas : A Pilot Study," *J. Vasc. Interv. Radiol.*, vol. 24, no. 11, pp. 1709–1718, 2013.

[158] R. Romero-méndez and E. Berjano, “An Analytical Solution for Radiofrequency Ablation with a Cooled Cylindrical Electrode,” vol. 2017, 2017.
[159] G. Zorbas and T. Samaras, “Simulation of radiofrequency ablation in real human anatomy,” vol. 6736, no. 8, pp. 570–578, 2014.
[160] W. van den Bos, D. M. de Bruin, R. R. Jurhill, C. D. Savci-Heijink, B. G. Muller, I. M. Varkarakis, A. Skolarikos, P. J. Zondervan, M. P. Laguna-Pes, H. Wijkstra, T. M. de Reijke, and J. J. M. C. H. de la Rosette, “The correlation between the electrode configuration and histopathology of irreversible electroporation ablations in prostate cancer patients,” *World J. Urol.*, vol. 34, no. 5, pp. 657–664, 2016.

List of Publications

1. R. Qasrawi and A. Ivorra, “Impact of liver vasculature on electric field distribution during electroporation treatments : an anatomically realistic numerical study,” in *6th European Conference of the International Federation for Medical and Biological Engineering*, 2014, pp. 573–576

2. L. Silve, R. Qasrawi, and A. Ivorra, “Incorporation of the Blood Vessel Wall into Electroporation Simulations,” 1st World Congress on Electroporation and Pulsed Electric Fields in Biology, Medicine and Food & Environmental Technologies. Springer Singapore, 2016. pp. 1–4.

3. R. Qasrawi, L. Silve, and F. Burdı, “Anatomically Realistic Simulations of Liver Ablation by Irreversible Electroporation : Impact of Blood Vessels on Ablation Volumes and Undertreatment,” Technology in cancer research & treatment (2017): 1533034616687477.

4. R. Qasrawi, B. Mercadal , Q. Castellvi, Z. Abdeen, and A. Ivorra, " Fast Semi-Analytical Approach for Computing 3D Electric Field Distribution in Electroporation Treatment Planning. (In Preparation for Submission)

Acknowledgments

It is my pleasure to thank those who helped and supported me in this thesis. First and foremost, I would like to thank my kind, great and supportive advisor, Prof. Antoni Ivorra, whose support, advice, valuable suggestions and guidance enabled me to develop this thesis until the finish.

I want to express my gratitude and special thanks to Prof.Ziad Abdeen for his guidance and support. I want to express my special thanks to Biomedical Electronics Research Group (BERG) team, specially, to Quim Castellví and Borja Mercadal for their valuable input in the development of our semi-analytical method for calculating the electric field distribution. I would like to thank the Department of Information and Communication Technologies staff, with special thanks to members of the secretariat for their help and support.

No words can capture all wonderful time and unforgettable memories that I have spent with my friends, those stands with me and gave me with the laugh and support that I need during these years.

Last but not least, I will like to express my deepest regards and appreciation goes to my family who defines every aspect in my life. I would like to thank my family and parents for their unending love and support.

Biography

Radwan Qasrawi was born in Jenin, Palestine, in August 1975. He studied electronic engineering at Al-Quds University and graduated in 1998. From 2003-2005, he studied Computer Science at Al-Quds University. Between 1999-2009, Radwan worked as a researcher and senior software developer at the Al-Quds Health and Nutrition Research Institute and conducted much biomedical technology and health research projects. Between 2009-2011, Radwan moved as researcher and lecturer at the department of computer science and information technology at Al-Quds University. In 2012, he joined the Biomedical Electronics Research Group at Universitat Pompeu Fabra as a Ph.D. student. Recently, Radwan got a grant of 700K€ for deploying electroporation treatments in Palestine. His project aims to establish electroporation treatment units in two hospitals and an electroporation research lab at Al-Quds University.